A wavelet based approach to the transient control of rotor/active magnetic bearing systems

Cade, Iain Stuart

Award date:
2006

Awarding institution:
University of Bath

A WAVELET BASED APPROACH TO THE TRANSIENT CONTROL OF ROTOR/ACTIVE MAGNETIC BEARING SYSTEMS

Submitted by Iain Stuart Cade
for the degree of
Doctor of Philosophy
of the University of Bath
2006

ProQuest LLC
789 East Eisenhower Parkway
P.O. Box 1346
Ann Arbor, MI 48106-1346

Abstract

Magnetic bearings exist in a wide variety of industrial applications of rotating machines. They offer advantages over normal passive bearings with their ability to vary force applied to the rotor and are commonly used with a control strategy to attenuate vibrations levels during operation.

This thesis is focused on the use of wavelet analysis in detecting and controlling the response due to disturbances in flexible rotor/magnetic bearing systems. A method for detecting sudden changes in synchronous forcing and rotor/auxiliary bearing contact is presented using wavelet coefficients. Artifacts associated with mass-loss and rotor/auxiliary bearing contact are identified in simulation and through experiment and shown to be distinguishable.

The discrete time transfer function of a rotor dynamic system is transformed to consider the behaviour of signal wavelet coefficients. This provides the basis for system analysis and controller design in the wavelet domain. A method of steady state identification is demonstrated using wavelet analysis to determine the long term behaviour of individual wavelet coefficient levels. Experimental validation is shown to identify the steady state vibration with a reduced transient response. Controller stability and performance are demonstrated using steady state prediction to moderate control signals.

A novel method for transient rotor/active magnetic bearing control using sampled wavelet coefficients is proposed. The wavelet based controller is designed from target transient responses due to step changes in wavelet coefficients of applied forces. Transient system dynamics are embedded in the controller and evaluated from online system identification. Simulated and actual mass-loss tests were performed at critical speeds corresponding to near sudden changes in unbalance that are capable of exciting rotor dynamic modes in a transient manner. The controller is shown to suppress the transient responses within a finite settling time.

Acknowledgements

I would like to thank my supervisors, Dr. Patrick Keogh and Dr. Necip Sahinkaya, for their direction and guidance during my studies. In particular, Dr. Patrick Keogh's support, willingness to teach and patience have been invaluable.

Thanks must also go to my family and friends. The faith and support from my parents and from Sarah Hiscock has been constant throughout.

Finally, I gratefully acknowledge the funding support of the Engineering and Physical Sciences Research Council grant GR/R45277/01.

Contents

Notation

Standard Variables

$\mathbf{A}, \mathbf{B}, \mathbf{C}, \mathbf{D}$	State space matrices
$\mathbf{A}^{(m)}_{p,q,p,q}$	Transient system gain matrices
A	Finite element nodal surface area
a	Wavelet dilation
$\mathbf{B}_{f,u}$	Force distribution matrices
$\mathbf{B}^{(m)}$	Matrix used to identify measured states
$\mathbf{B}^{(m)}_{p,q,p,q}$	Transient system inverse gain matrices
$B_{1,2}$	Magnetic flux density
b	Wavelet dilation
$c(a,b)$	Wavelet coefficient
c_g	Zero displacement rotor/auxilary bearing separation
E	Young's modulus
e	Mass eccentricity
$\mathbf{F}_{a,b}(z)$	Wavelet coefficient force in the Z-transform domain
$\mathbf{F}(t)$	System forcing term

$\bar{\mathbf{f}}(s)$	Laplace transform of disturbance vector
F	Electromagnetic coil force
$\mathbf{G}$	Gyroscopic damping matrix
$\mathbf{G}^0_{p,q}(z)$	Time period average wavelet coefficient transfer function
$\mathbf{G}_{p,q,p,q}(z)$	Wavelet coefficient transfer function
$g_{0,1}$	Wavelet reconstruction filter
$\mathbf{H}_{a,b}(z)$	Error dynamic transfer function
$H(t)$	Heaviside step function
$h_{0,1}$	Wavelet decomposition filter
$I_{d,p}$	Finite element diametral/polar inertia
$I_{1,2,s,b}$	Constant electric currents
$i_{1,2}(t)$	Time variant electric control currents
i	Imaginary number
i	Controller delay
J	Number of octaves
j	Octave index number
$\mathbf{K}_a$	Rotor element axial stiffness matrix
$\mathbf{K}_b$	Rotor element stiffness matrix
$\mathbf{K}_c$	Coupled stress-strain stiffness matrix
K_z	Negative stiffness
K_i	Current gain
k	Discrete time index
$\mathbf{L}_{p,q}(z)$	Transient wavelet coefficient controller
L	Coil inductance
l_g	Rotor displacement

l	Finite element length
$\mathbf{M}_{t,r}$	Translational and rotational finite element mass matrices
m_e	Finite element mass
m	Dummy variable time period index
m	Mass unbalance
$\mathbf{N}_{t,r}$	Translational and rotational finite element shape matrices
N	Number of coil windings
N	Number of eigenvalues
n	Discrete time index
n	Mother wavelet order
p	Wavelet translation
$\mathbf{Q}_{p,q}(z)$	Displacement wavelet coefficient in the Z-domain
$\mathbf{Q}_{p,q}^{(m)}(z)$	Measured displacement wavelet coefficient in the Z-domain
$\mathbf{q}(t)$	State vector
$\overline{\mathbf{q}}(s)$	Laplace transform of state vector
q	Wavelet translation
R	Coil resistance
$\mathbf{r}(t)$	Rotating frame coordinate
s	Laplace variable
$\mathbf{S}_{p,q}(z)$	Steady state wavelet identifier
$\mathbf{T}(t)$	Rotating frame coordinate transform matrix
T	Coil time constant
T	Time period
$\mathbf{U}_{p,q}(z)$	Wavelet coefficient control signal
$\mathbf{u}(t)$	Control force vector

$\mathbf{V}$	System eigenvectors
$\mathbf{V}(l)$	l^{th} system eigenvector
$v_{1,2}(t)$	Coil voltage
$v_{p,q}(z)$	Prescribed transient response characteristic
$\mathbf{W}_{p,q}^{(m)}$	Desired steady state wavelet coefficient response
$w_{p,q}(z)$	Prescribed transient response characteristic
$\mathbf{X}_n^0$	Average rotor displacement over n^{th} period
$\mathbf{x}(t)$	Rotor displacements at finite element node
$x[n]$	Discrete time signal
$\mathbf{y}(t)$	Base displacement vector
$\mathbf{y}(t)$	State space system output
$\mathbf{y}_k$	PID controlled state space system input vector (rotor displacement)
z	Discrete time variable

Greek Variables

$\alpha_{p,q}(z)$	Prescribed transient response
$\Delta\omega$	Wavelet bandwidth
Δt	Wavelet time dispersion
$\delta(t)$	Dirac delta function
Λ	System eigenvalues
λ_l	l^{th} system eigenvalue
μ_0	Permeability of free space
$\psi(t)$	Mother wavelet
Ω	Angular frequency
ω	Angular frequency
ω	Coil cut-off frequency

Transforms

$FT[.]$	Fourier transform
$FT^{-1}[.]$	Inverse Fourier transform
$\mathcal{L}[.]$	Laplace transform
$\mathcal{L}^{-1}[.]$	Inverse Laplace transform

Superscript Variables

$(.)^*$	Denotes pseudo inverse
(i)	Denotes wavelet coefficient level
(m)	Denotes measured variable

Subscript Variables

a	Wavelet dilation index
b	Wavelet translation index
m	Filter coefficient
n	Filter coefficient
p	Wavelet dilation index
q	Wavelet translation index

Terminology

ADC	Analogue to digital converter
AMB	Active magnetic bearing
Coif$n$	n^{th} order Coifman mother wavelet
CWT	Continuous wavelet transform
DAC	Digital to analogue converter
Daub$n$	n^{th} order Daubechies mother wavelet
DWT	Discrete wavelet transform
LHS	Left hand side
MB	Megabyte
PID	Proportional-integral-differential
PC	Personal computer
RHS	Right hand side
SDRAM	Synchronous dynamic read only memory

Chapter 1

INTRODUCTION

1.1 Control Issues In Rotor/Magnetic Bearing Systems

The industrial applications of active magnetic bearings can be separated into four different domains; aerospace applications, machine tool applications, light industrial and heavy industrial applications [1]. Within the aerospace domain there are two main uses for active magnetic bearings. The first is for use with momentum/energy storage flywheels such as those on satellites. The second is for use in turbopumps in jet and rocket engines. Machine tool applications are limited to electro-spindles used in milling and grinding, however, these are commonplace within industry. Light industrial applications include machines with a rotor of less than 50kg supported by active magnetic bearings, [1]. They cover a wide range of applications such as in X-ray tubes, liquid helium pumps, and most commonly, turbomolecular pumps. Heavy industrial applications are mostly limited to compressors, turbo expanders and generators. Furthermore, rotor magnetic bearing systems can be classified in terms of how they operate, whether the system is fully levitated or requires additional support and whether the rotor operates above its first critical bending speed, i.e. rigid or flexible. Although the range of application varies considerably the reasons for their use remain common. Since the rotor is supported by an electromagnetic field the system operation is contact free, and therefore frictionless. During operation the absence of rotor bearing contact means that the bearing requires no lubrication allowing it operate in a vacuum or in sensitive and/or aggressive environments. Operation at high speed and at temperature extremes is also achievable. In the case of active magnetic bearings, in contrast to passive magnetic bearings, it is possible to apply control forces to the rotor in order to attenuate rotor vibration.

An active radial magnetic bearing is essentially a collection of electromagnetic actuators arranged to apply lateral forces to a rotor. Although axial magnetic bearings also exist the focus of this thesis is on the radial type. The forces acting on the rotor are governed by electromagnetic principles and can be varied in conjunction

with a controller in order to ensure specified system dynamics. As a requirement of the control, but useful on its own, the rotor can also be monitored, allowing for safety and preventative maintenance. There are several main control problems associated with rotor/active magnetic bearing systems. The rotor needs to be accelerated and retarded during run-up and run-down procedures, respectively. During operation the system can undergo direct and indirect forcing. Examples of direct rotor forcing include rotor contact, rotor unbalance, which causes a synchronous forcing component, and aerodynamic excitation caused by sudden pressure changes. Indirect forces are often associated with external seismic activity during which the rotor housing moves relative to the rotor. This can be considered as an indirect force acting on the rotor in a stationary housing. Indirect forcing is a common issue among land, sea and air transport applications.

Many of the rotors used in magnetic bearing systems can be considered rigid. However, in applications such as compressors the first bending critical speed can be exceeded during normal operation. This can lead to problems when designing a control strategy. During rigid body vibrations the position of the rotor can be measured in two planes along the shaft. The position of any other point along the shaft can be evaluated by interpolating or extrapolating the displacement of the rotor at the measured planes to that point. This is not the case when the rotor is considered flexible where vibration nodes may occur close to sensor planes at particular frequencies.

Many different control strategies have been devised to control rotor/magnetic bearing during both steady state and transient forcing conditions. Rotor/magnetic bearing stability is easily achievable with local proportional-integral-derivative (PID) control, [2]. The closed loop characteristics of the system can be influenced by changing the PID gains. These include bearing stiffness, transmission forces and modal damping.

A common problem associated with rotating machinery is that of rotor unbalance resulting in steady state rotor vibration. Since the frequency of vibration is equal to the rotational speed of the rotor this is often referred to as the synchronous control problem. Burrows and Sahinkaya [3, 4] used an open-loop technique to eliminate synchronous vibration. Knospe *et al.* [5–7] present adaptive open-loop control methods updating control currents on a cyclic basis in order to remove synchronous vibration components. An adaptive open-loop controller is presented by Sahfai *et al.* [8], though in simulation only, in order to solve the problem of sudden variation in rotor unbalance. These techniques can be extended to consider multiple frequency components in order to provide more general rotor control. Cole *et al.* [9] identify a multi-level approach considering multiple frequencies. This has been further extended to consider transient control by Keogh *et al.* [10] using sampled harmonics.

There are many different robust control methods applicable to linear systems, and it is well understood that both H_∞ and μ-synthesis offer robust control strategies. An

H_∞ based controller was developed by Fujita *et al.* [11] to control an experimental model of a flexible rotor suspended with an active magnetic bearing. It was shown that the controller was robustly stable against various plant perturbations and provided good control of the rotor to input disturbance. Herzog and Bleuler [12, 13] present an H_∞ formulation for wideband disturbance attenuation. They provide a framework in which the disturbance attenuation and other performance criteria can be achieved. Rotor unbalance control has been formulated using H_∞ techniques (Mu *et al.* [14]) in order to provide optimal control. More recently, Keogh *et al.* [15] presented an H_∞ control method for transient vibration attenuation. Optimization of the H_∞ norm was used to minimize the system response to direct forcing, modelling error and measurement error. Cole *et al.* [16] present an H_∞ control algorithm to control base motion due to an impact and direct rotor forcing applied simultaneously. To ensure robustness using H_∞ controller design it is required that the errors between the system model and the system are understood. This can often result in an overly conservative controller. Nonami and Ito [17] use μ-synthesis to formulate a more accurate representation of plant perturbations and error analysis in order to achieve improved controller performance. However, optimally designed controllers are limited in their performance due to the compromise between high system order and computational efficiency in real-time implementation.

Rotor gyroscopic effects are dependent on the running speed, and so therefore are the system dynamics. The operational speed range of the system is therefore an important consideration when designing a controller. Optimally designed controllers operating outside their prescribed running speeds may become ineffective or unstable. Knospe *et al.* [5] and Sivrioglu and Nonami [18] use gain scheduling to overcome this problem.

A controller designed with a specific objective, such as synchronous vibration attenuation, may be ineffective during different fault conditions. Sufficient control forces in a fault condition can be evaluated using either a control strategy ensuring stability under open loop failure or by changing the control strategy itself. Cole *et al.* [19] present a method of fault tolerant control through the use of a neural network to identify faults and reconfigure an H_∞ control strategy to deal with the fault. Seo and Kim [20] focus on the design of an H_∞ control strategy robust to linear time-varying parameter uncertainty and actuator failure. The work of Gündes [21] presents a design method to ensure system stability during failure of actuators and sensors.

In order to change the control strategy it is important to be able to identify the onset, duration and type of disturbance. This is required to ensure that appropriate control forces are applied to the rotor to restore the system to an operating condition within acceptable bounds. A wide variety of model-based approaches have been taken to identify faults. Sauter and Hamelin [22] consider a method of fault identification from residuals identified from the systems's input-output relation. Increased residual robustness is achieved with frequency-domain fault-detection filtering, where the effect of the filter is to optimize the ratio of magnitudes between a fault and

disturbance. Maki and Loparo [23] offer a neural network approach to fault detection, which has advantages since little understanding of the system is required. It is also applicable to systems with non-linearities. Sahinkaya *et al.* [24] introduced a stochastic approach to fault detection and tolerance including on-line identification. Bachschmid *et al.* [25] present a method of multiple fault identification by means of model-based identification in the frequency domain.

1.2 Wavelet Analysis And Its Application To Rotor/ Magnetic Bearing Systems And Control

The are many different frequency based techniques used to control rotating machinery. In the simplest case synchronous controllers have been developed to minimize the synchronous vibration often associated with rotor unbalance [3–8]. Multiple frequency based techniques have also been presented. Cole *et al.* consider a method for identifying a control signal from multiple input frequencies [9, 10]. Adaptive open-loop control strategies have mainly concentrated on a periodic update to a Fourier coefficient. However, there are many ways to manipulate a signal with digital signal processing offering alternatives to Fourier analysis. The wavelet transform, like the Fourier transform, is a transformation of a time varying signal into its frequency components. However, unlike the Fourier transform, the wavelet transform provides resolution in both time and frequency subject to an uncertainty principle.

Wavelet analysis is used in a wide variety of applications exploiting its localization characteristics. These include image processing [26, 27], neural networks [28], ultrasound [29], de-noising [30, 31], communication theory [32] and vibration analysis [33–35]. The use of wavelet analysis in signal de-noising is in many ways similar to the open-loop control techniques used for synchronous rotor control. The initial signal is decomposed into its frequency elements, or wavelet coefficients, upon which a decision is made in order to achieve a desired output signal. Threshold techniques of de-noising are among the most common used. In this method a signal is decomposed using a discrete wavelet transform, the coefficients are then modified by a threshold to remove the smaller noise related coefficients (Frodor *et al.* [31] and Donoho [30]).

Newland [33, 36] proposes a method of analyzing a recorded vibratory signal with wavelets leading to an analysis technique involving wavelet maps. It was indicated that the wavelet transform would allow for the detection of small details of waveform that may otherwise go unnoticed [36]. Wavelet maps of the analyzed signal allow for immediate identification of any signal perturbations, while the Fourier transform of the same signal may not [36]. Wavelet analysis is therefore a significant tool for the analysis of time varying signals. However, the methods presented by Newland are limited to post analysis rather than for use as a real-time technique. It is also worth noting that the wavelets developed by Newland [33,36] are harmonic wavelets

and have a magnitude over all time. Harmonic wavelets have also been shown to be useful because of their close relation to the fast Fourier transform algorithm.

Harmonic wavelets were also used by Chancey and Flowers *et al.* [34,37] as a means of studying and characterizing rotor dynamic vibrations. The technique uses the frequency banding capabilities of the harmonic wavelet [37]. This forms an octave based analysis providing good representation of a specific octave dependent frequency. If the frequency band contains only a single significant frequency then the growth function of that particular frequency can be extracted [34]. Chancey and Flowers propose that, from the growth function identification of the modal damping, the characterization of faults is possible from transient data [34].

Staszewski [35, 38] makes use of the continuous wavelet transform in identifying the damping characteristics of multi-degree-of-freedom models. Three techniques are outlined. The simplest is a cross section of the continuous wavelet transform (CWT) along a fixed pseudo frequency. This provides a measure of the damping from analysis of the change in magnitude. An impulse response recovery method and the Ridges and Skeleton method are also presented [35]. The Ridges and Skeleton method is used further by Staszewski in the identification of non-linear systems [38].

Wavelet analysis has further been used to identify fault conditions in a variety of rotating machinery components including rolling element bearings [39], gear boxes [40], cracked [41] and misaligned rotors [42]. Lin and Qu [43] use the Morlet wavelet to extract features from the measured vibration of a gear-box to identify the magnitude and position of gear damage. Boulahbal *et al.* [44] identify cracks in geared systems from measured vibrations and off-line analysis using amplitude and phase wavelet maps.

Wavelets are not only limited to signal processing in off-line techniques, they are increasingly being considered for real-time systems. The use of wavelets as a basis function in a network is presented by Zhang and Benveniste [45]. This is further utilized by Lin and Huang [46] who propose an on-line approach to the control of a servomotor by realizing wavelet based network-learning. The disturbance rejection of repetitive and rapidly varying features is a natural basis for wavelets and is utilized by the learning network. This method may exploit many of the attributes of wavelet analysis, however, it takes no account of the digital implementation and signal processing.

A method of control acting directly on the wavelet coefficients as gains is proposed by Parvez and Goa [47]. A generalized proportional-integral-differential (PID) controller is derived from feedback of scaled wavelet coefficients. The multiple tunable parameters (each for a wavelet coefficient level) offer advantages over PID control, however, steady state error in will always be present since a wavelet of infinite time duration would be required. Zhou *et al.* [48] use a method of wavelet weighted residuals to determine a control signal for piezoelectric sensor plates.

1.3 Research Overview

This work aims to investigate and present methods of transient control for a rotor/active magnetic bearing system using sampled wavelet coefficients. It is both theoretically and experimentally based. The experimental facility is presented in chapter 2 and discussed along with general techniques used for modelling flexible rotors and active magnetic bearings. A discussion considering specific faults associated with rotor/active magnetic bearing systems is presented in chapter 3. These include rotor unbalance, rotor/auxiliary bearing contact, base motion, bearing failure and sensor failure.

Wavelet analysis has been identified as an emerging technique for studying vibrations in rotating machinery. It has also been used in basic control strategies. The aim of this research is to study how wavelet analysis can be applied to rotor/active magnetic bearing systems. Consideration is given to fault identification and steady state prediction with the objective of developing a transient control strategy. During transient rotor vibrations, multiple frequency components are present. During this period wavelet analysis can offer a better representation of rotor vibration than harmonic/Fourier analysis. To qualify this it is important to have an understanding of the wavelets used to represent the signal. Chapter 4 provides an overview of wavelet analysis starting from the transform itself and covering the continuous and discrete cases leading to a digital signal processing approach. The uncertainties involved in the transform are also considered.

Using digital signal processing to evaluate wavelet coefficients, chapter 5 considers fault identification in the wavelet coefficient domain. Chapter 6 considers the system in more detail, identifying the dynamic behaviour of wavelet coefficients. This is expanded in chapter 7 by filtering the wavelet coefficients in order to evaluate the steady state level of the system. In chapter 7 a control strategy is developed and steady state prediction is used to moderate the control signal to improve system performance. This is expanded upon in chapter 8 leading to a control strategy designed to provide transient rotor control using sampled wavelet coefficients. The conclusions of this thesis are presented in chapter 9.

The methods presented in this thesis have been or are to be published. Fault identification using discrete time wavelet coefficients, discussed in chapter 5, is presented in reference [49]. The results presented in chapter 8, considering transient rotor/active magnetic bearing control using sampled wavelet coefficients, have been accepted for publication in the ASME Journal for Engineering for Gas Turbines and Power. The method of controller moderation using steady state prediction, presented in chapters 6 and 7, has been submitted for publication.

Chapter 2

ROTOR/ACTIVE MAGNETIC BEARING SYSTEM OVERVIEW

2.1 Experimental Facility

The aim is to develop novel control methods based on wavelet analysis for vibration attenuation in rotor/magnetic bearing systems. In order to demonstrate controller effectiveness an experimental facility is to be used. This chapter discusses the experimental facility and considers the full model of the system. The design specification and calibration can be found in references [50–52]. An overview of the power electronics specification and performance is also presented.

The system (figure 2.1) consists of a 2m long shaft upon which four movable disks are positioned. The rotor is supported by two radial active magnetic bearings. Each magnetic bearing has 8 poles forming four coil pairs. These are configured as two orthogonal opposing pairs and are positioned at 45^0 to the vertical in order to maximize static load capacity (figure 2.2). Auxiliary rolling element bearings are positioned inside the active magnetic bearings in order to prevent rotor contact with the lamination stacks. The radial clearance between rotor and auxiliary bearing is nominally 750μm. Two further bronze retaining bearing are positioned at the end of the rotor with a radial clearance of 900μm. Rotor displacement is measured using eight eddy current transducers arranged into four orthogonal pairs. Transducer pairs are positioned at the rotor ends and next to the active magnetic bearings on the inner side. Initial rotor control is achieved using proportional-integral-differential (PID) control using the four transducers local to the magnetic bearings. The closed loop is achieved with the addition of a controller and power electronics. A separate motor is used to drive the system, through a flexible coupling. The motor has a

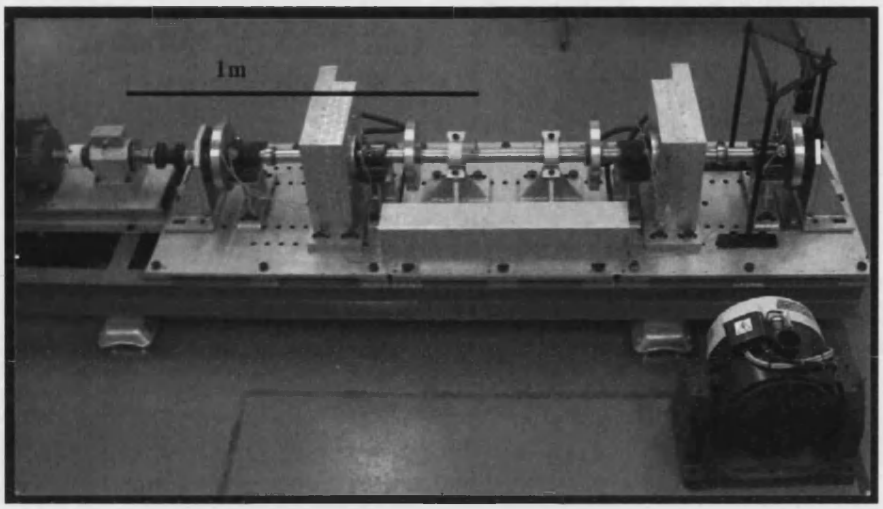

▌Sensor plane location and corresponding sensor numbers 1-8
▌Auxiliary Bearing

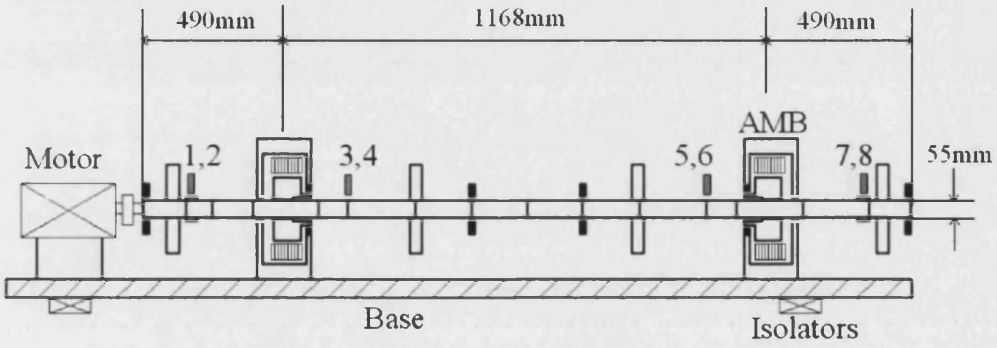

Figure 2.1: Experimental flexible rotor/active magnetic bearing rig photograph and schematic layout.

separate controller and can run at speeds up to 100Hz (6000rpm).

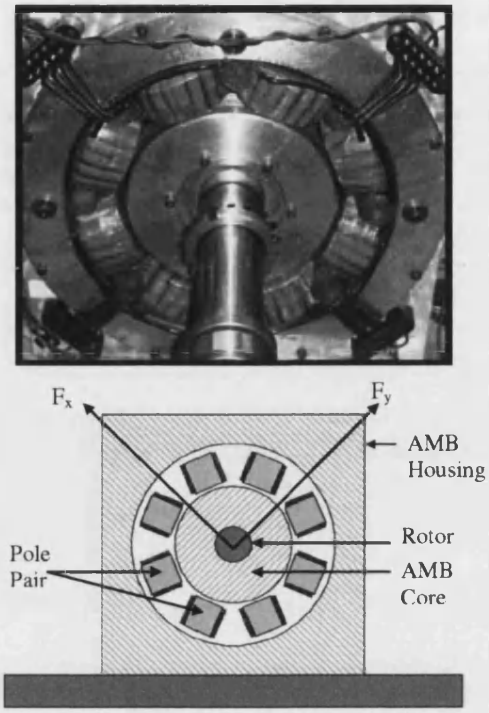

Figure 2.2: Active magnetic bearing coils and laminated stack photograph (left) and schematic (right).

2.2 Rotor Modelling

Flexible rotor systems have been modelled using many different mathematical methods. The chosen technique is based on finite element modelling as presented by Nelson and McVaugh [53] and others [54,55]. The rotor was designed such that the first two critical bending speeds are below the maximum operating speed.

2.2.1 Finite Element Modelling

An overview of finite element modelling as discussed by Nelson and McVaugh is presented. The basis for construction of a finite element model lies in the consistent representation of the mass and elasticity, Nelson and McVaugh [53]. This is achieved through the discretization of a continuous structure into smaller elements, from

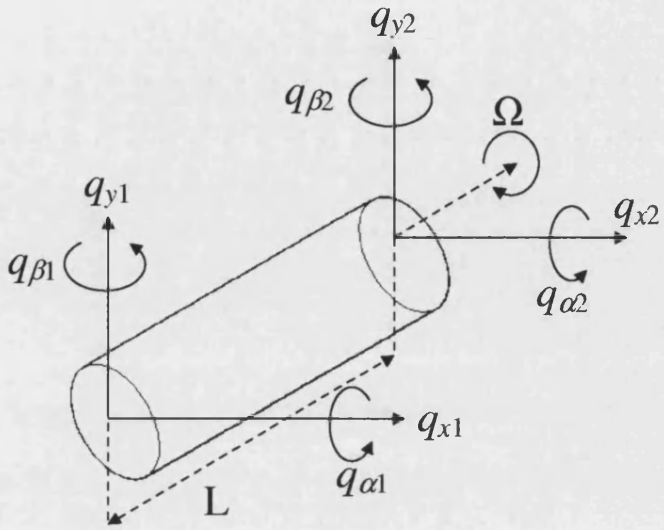

Figure 2.3: Finite element and coordinates.

which the displacements can be described by the nodal positions

$$\mathbf{q} = [q_{x1}, q_{y1}, q_{\alpha 1}, q_{\beta 1}, q_{x2}, q_{y2}, q_{\alpha 2}, q_{\beta 2}, \ldots, q_{xN}, q_{yN}, q_{\alpha N}, q_{\beta N}]^T \tag{2.1}$$

Figure 2.3 shows a finite element representation of a rotor and corresponding coordinate system. The translation, $\mathbf{V}(s,t)$, and rotation, $\mathbf{W}(s,t)$, of a point on the surface of a element are characterized by

$$\mathbf{V}(s,t) = \mathbf{N}_t(s)\mathbf{q}^e(t) \tag{2.2}$$

$$\mathbf{W}(s,t) = \mathbf{N}_r(s)\mathbf{q}^e(t) \tag{2.3}$$

where $\mathbf{N}_{t,r}$ are the shape functions for the element. From consideration of the potential and kinetic energies, equations for the translational and rotational mass, gyroscopic coupling and stiffness matrices can be identified for each element as

$$\mathbf{M}_t = m^e \int_0^L \mathbf{N}_t(s)^T \mathbf{N}_t(s) ds \tag{2.4}$$

$$\mathbf{M}_r = I_d^e \int_0^L \mathbf{N}_r(s)^T \mathbf{N}_r(s) ds \tag{2.5}$$

$$\mathbf{G} = m^e \int_0^L \mathbf{N}_r(s)^T \begin{bmatrix} 0 & 1 \\ -1 & 0 \end{bmatrix} \mathbf{N}_r(s) ds \tag{2.6}$$

$$\mathbf{K}_b = \int_0^L \ddot{\mathbf{N}}_{t,b}(s)^T \ddot{\mathbf{N}}_{t,b}(s) ds + \frac{12}{\Phi L^2} \int_0^L \dot{\mathbf{N}}_{t,b}(s)^T \dot{\mathbf{N}}_{t,b}(s) ds \tag{2.7}$$

$$\mathbf{K}_a = A \int_0^L \ddot{\mathbf{N}}_t(s)^T \ddot{\mathbf{N}}_t(s) ds \tag{2.8}$$

The undamped equation of motion of the element is

$$(\mathbf{M}_t + \mathbf{M}_r)\,\ddot{\mathbf{q}}_e + \Omega \mathbf{G} \dot{\mathbf{q}}_e + (\mathbf{K}_b - \mathbf{K}_a)\,\mathbf{q}_e = \mathbf{F} \tag{2.9}$$

Zorzi and Nelson [54] extended the model to incorporate two forms of linear internal damping. The first is a linearly frequency dependent viscous damping, the second is a frequency independent or hysteretic damping given by ς_v and ς_h, respectively. The damping terms are derived from a comparison between the axial stress and strain from which a damping component can be expressed as

$$\mathbf{K}_c = EI \int_0^L \ddot{\mathbf{N}}_{t,b}(s)^T \begin{bmatrix} 0 & 1 \\ -1 & 0 \end{bmatrix} \ddot{\mathbf{N}}_{t,b}(s) \tag{2.10}$$

The damped equation of motion of an element can be identified as

$$\begin{aligned} &(\mathbf{M}_t + \mathbf{M}_r)\,\ddot{\mathbf{q}}_e + (\varsigma_v \mathbf{K}_c + \Omega \mathbf{G})\,\dot{\mathbf{q}}_e + \\ &\left(\frac{1+\varsigma_h}{\sqrt{1+\varsigma_h}} \mathbf{K}_b - \mathbf{K}_a + \left(\varsigma_v \Omega + \frac{\varsigma_h}{\sqrt{1+\varsigma_h}} \right) \mathbf{K}_c \right) \mathbf{q}_e = \mathbf{F} \end{aligned} \tag{2.11}$$

where ς_v and ς_h represent viscous and hysteretic damping, respectively. The addition of flywheels and couplings to the model can be simplified by assuming them to be slender, axially-symmetric disks. They can be described by their translational mass, m_d, diametral inertia, I_d, and polar inertia, I_p. Their corresponding mass and damping matrices can be identified as

$$\mathbf{M_{disk}} = \begin{bmatrix} m_d + m_c & 0 & 0 & -l_d m_d \\ 0 & m_d + m_c & l_d m_d & 0 \\ 0 & l_d m_d & I_d & 0 \\ -l_d m_d & 0 & 0 & I_d \end{bmatrix} \tag{2.12}$$

$$\mathbf{C_{disk}} = \begin{bmatrix} 0 & 0 & 0 & 0 \\ 0 & 0 & 0 & 0 \\ 0 & 0 & 0 & I_p \\ 0 & 0 & -I_p & 0 \end{bmatrix} \tag{2.13}$$

where l represents the distance between the center of mass of a disk and its geometric centre. m_d and m_c represents the addition of any mass positioned at the node due to flywheels or couplings, respectively. l_d is introduced to represent any offset from the centre of mass of the disk to the element node. From evaluation of all the individual element matrices and those of any additional flywheels and couplings the full model is

$$\mathbf{M}\ddot{\mathbf{q}} + (\Omega \mathbf{G} + \mathbf{C})\dot{\mathbf{q}} + \mathbf{K}\mathbf{q} = \mathbf{B}_f \mathbf{f} + \mathbf{B}_u \mathbf{u} \tag{2.14}$$

where $\mathbf{M}$, $\mathbf{C}$, $\mathbf{K}$ and $\mathbf{G}$ are the mass, damping, stiffness and gyroscopic matrices respectively. $\mathbf{B}_f$ and $\mathbf{B}_u$ are distribution matrices which map the dimensions of $\mathbf{f}$ and $\mathbf{u}$ to that of $\mathbf{q}$. $\mathbf{M}$, $\mathbf{C}$, $\mathbf{K}$ and $\mathbf{G}$ are identified from the superposition of the contributing terms at each node and have dimensions of $4(n+1) \times 4(n+1)$, where n is the number of elements used.

2.2.2 Mode Shapes

Equation (2.14) can be transformed into a first order problem without control, $\mathbf{u}(t) = \mathbf{0}$, as

$$\dot{\mathbf{q}} = \mathbf{A}\mathbf{q} + \mathbf{B}\mathbf{f}, \qquad \mathbf{q} = \begin{bmatrix} \mathbf{x} \\ \dot{\mathbf{x}} \end{bmatrix} \tag{2.15}$$

$$\mathbf{A} = \begin{bmatrix} \mathbf{0} & \mathbf{I} \\ -\mathbf{M}^{-1}\mathbf{K} & -\mathbf{M}^{-1}(\Omega\mathbf{G} + \mathbf{C}) \end{bmatrix}, \quad \mathbf{B} = \begin{bmatrix} \mathbf{0} \\ \mathbf{M}^{-1}\mathbf{B}_f \end{bmatrix} \tag{2.16}$$

where $\mathbf{q}$ denotes the state vector. The system characteristics may be derived from the eigenvalue problem:

$$\mathbf{A}\mathbf{V} = \mathbf{V}\Lambda \tag{2.17}$$

The transformation $\mathbf{q} = \mathbf{V}\rho$ implies that

$$\dot{\rho}(t) = \Lambda\rho(t) + \mathbf{V}^{-1}\mathbf{B}\mathbf{f}(t) \tag{2.18}$$

The response of a specific mode, l, can be isolated by taking a single row of equation (2.18):

$$\dot{\rho}_l(t) = \lambda_l\rho_l(t) + \left(\mathbf{V}^{-1}\mathbf{B}\right)_l \mathbf{f}(t) \tag{2.19}$$

where λ_l is the eigenvalue of mode l, and $\left(\mathbf{V}^{-1}\mathbf{B}\right)_l$ corresponds to the l^{th} row of $\mathbf{V}^{-1}\mathbf{B}$. Taking the Laplace transform of equation (2.19), as indicated by $\bar{\cdot}$, gives

$$s\bar{\rho}_l(s) = \lambda_l\bar{\rho}_l(s) + \left(\mathbf{V}^{-1}\mathbf{B}\right)_l \bar{\mathbf{f}}(s) \tag{2.20}$$

The response of the system can be evaluated by superposing the individual modal contributions:

$$\bar{\mathbf{q}}(s) = \sum_{l=1}^{2N} \frac{\mathbf{V}_l \left(\mathbf{V}^{-1}\mathbf{B}\right)_l}{s - \lambda_l} \bar{\mathbf{f}}(s) \tag{2.21}$$

where $\mathbf{V}_l$ is the l^{th} modal (column) vector. From the eigenvalues and corresponding eigenvectors, the critical speeds, damping and mode shapes of the system can be identified. The first four, zero speed, flexible free-free rotor mode shapes are shown in figure 2.4. Two rigid body modes are present at zero frequency, these are cylindrical and conical in nature.

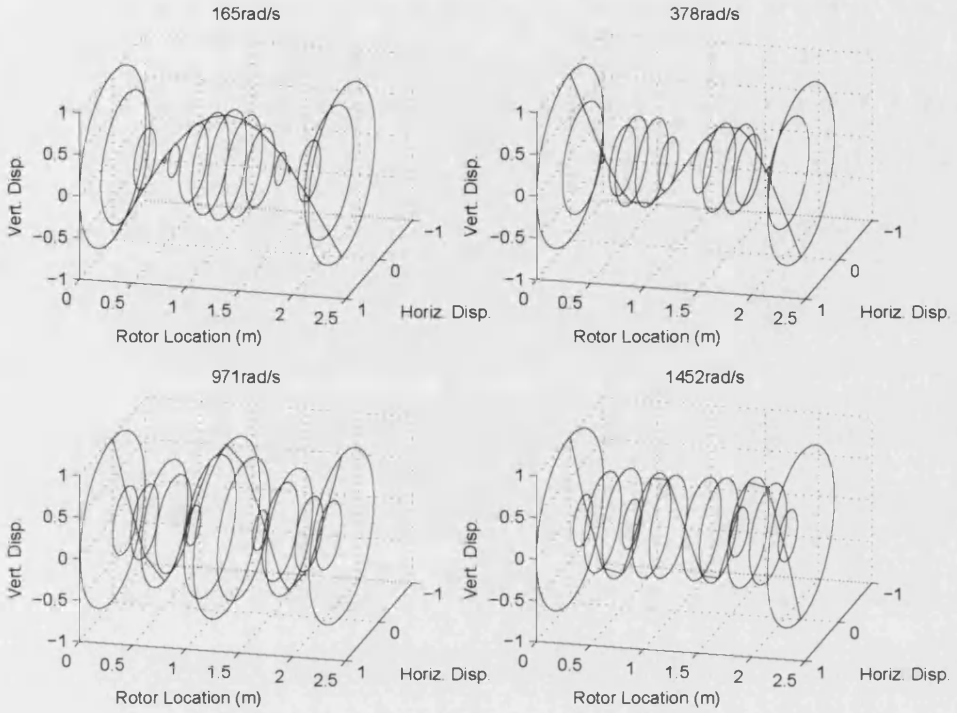

Figure 2.4: Free-free rotor mode shapes

2.2.3 Rotating Reference Frame System Transformation

Equation (2.14) governs the dynamic behaviour of the system model in a fixed reference frame. However, in rotating machinery it is common for the system to experience disturbance forces acting synchronously (e.g. rotor unbalance). Consideration of the rotor response in a rotating reference frame is therefore advantageous for certain problems. Expressing the fixed reference frame coordinate vector, $\mathbf{x}(t)$, in terms of a transformed rotating frame coordinate vector, $\mathbf{r}(t)$, the relevant form is

$$\mathbf{x}(t) = \mathbf{T}\mathbf{r}(t) \tag{2.22}$$

where $\mathbf{T}$ is a reference frame transformation matrix. Expressions for the first and second derivatives of $\mathbf{x}(t)$ are

$$\dot{\mathbf{x}} = \dot{\mathbf{T}}\mathbf{r} + \mathbf{T}\dot{\mathbf{r}} \tag{2.23}$$

$$\ddot{\mathbf{x}} = \ddot{\mathbf{T}}\mathbf{r} + 2\dot{\mathbf{T}}\dot{\mathbf{r}} + \mathbf{T}\ddot{\mathbf{r}} \tag{2.24}$$

Substitution into equation (2.14) gives the equation of motion of the system in a rotating coordinate system as:

$$\begin{aligned}&\mathbf{M}\ddot{\mathbf{Tr}} + (\Omega\mathbf{G} + \mathbf{C})\,\dot{\mathbf{Tr}} + \mathbf{KTr} \\ &+ 2\mathbf{M}\dot{\mathbf{T}}\dot{\mathbf{r}} + (\Omega\mathbf{G} + \mathbf{C})\mathbf{T}\dot{\mathbf{r}} \\ &+ \mathbf{MT}\ddot{\mathbf{r}} \\ &= \mathbf{T}\,(\mathbf{B_f f} + \mathbf{B_u u})\end{aligned} \tag{2.25}$$

For a synchronous rotating reference frame the transform matrix, $\mathbf{T}$, takes the form:

$$\mathbf{T}(t) = \begin{bmatrix} \cos\Omega t & \sin\Omega t \\ -\sin\Omega t & \cos\Omega t \end{bmatrix} \mathbf{S} \tag{2.26}$$

where Ω represents the angular velocity. $\mathbf{S}$ is a distribution matrix which maps the dimensions of $\mathbf{T}$ to that of $4(n+1) \times 4(n+1)$ corresponding to $\mathbf{x}$ and $\mathbf{r}$, of size $4(n+1) \times 1$. Taking the first and second derivatives of the transform matrix with respect to time gives:

$$\ddot{\mathbf{T}} = -\Omega^2\mathbf{T} \tag{2.27}$$

$$\dot{\mathbf{T}} = \Omega\Delta\mathbf{T} \tag{2.28}$$

where Δ represents the coupling between x and y as :

$$\Delta = \begin{bmatrix} 0 & 1 \\ -1 & 0 \end{bmatrix} \tag{2.29}$$

Therefore the amended mass, stiffness and damping matrices for a rotating reference frame can be expressed as:

$$\begin{aligned}\mathbf{M_r} &= \mathbf{M} \\ \mathbf{C_r} &= (\Omega\mathbf{G} + \mathbf{C}) + 2\Omega\Delta\mathbf{M} \\ \mathbf{K_r} &= \mathbf{K} + \Omega\Delta(\Omega\mathbf{G} + \mathbf{C}) + \Omega^2\mathbf{M}\end{aligned} \tag{2.30}$$

2.2.4 Experimental Rotor Model

Table 2.1: Table of rotor data.

Parameter	Rotor Element	Disk	Core
Density	7850 kg/m^3	7850 kg/m^3	6000 kg/m^3
Outer radius	25 mm	125 mm	89 mm
Inner radius	0 mm	25 mm	25 mm
Length	(see figure 2.5)	35 mm	60 mm

Defining critical nodal positions at the sensors planes and active magnetic bearings sets the minimum number of finite elements to seven. The rotor consists of a shaft

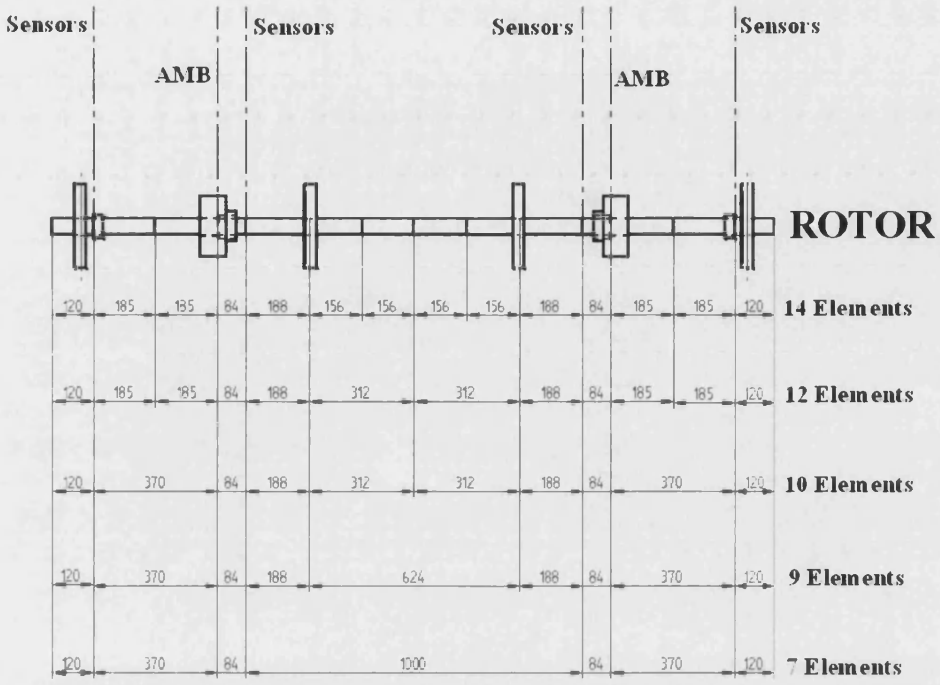

Figure 2.5: Rotor with successive levels of finite element discretization. Dimensions are in mm.

weighing 50kg and 2m in length with four 10kg disks positioned along the rotor. The experimental rig has two active magnetic bearings and therefore two, 5kg, rotor cores are added to the rotor. Figure 2.5 shows examples of the finite element rotor discretization and positioning of the flywheel disks and rotor cores. There is also the addition of two small collars at the outer transducer planes. Table 2.1 contains other data of the rotor, disks and active magnetic bearing cores.

It is important to ensure that there are enough elements to accurately model the rotor, but few enough to ensure computational efficiency for modelling and future controller designs. This was achieved through modelling the rotor with successively more elements until the zero speed natural frequencies of the rotor converged. Figure 2.5 shows the successive discretization of the rotor up to 14 elements. Since there is no grounding force, the first two rigid body modes occur at zero frequency. Figure 2.6 shows the convergence of the first four non-zero natural frequencies of the rotor at zero running speed. Their corresponding mode shapes are shown in figure 2.4.

The effect of increasing the speed of the rotor leads to increased gyroscopic effects and an increase in the stiffness $\mathbf{K}_c$, both of which are coupled in the x-y plane. This

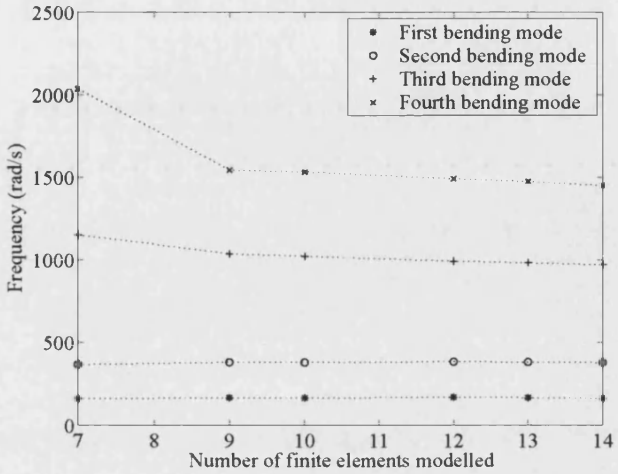

Figure 2.6: Convergence of the first four non-zero natural frequencies with relation to the number of finite elements modelled at zero running speed.

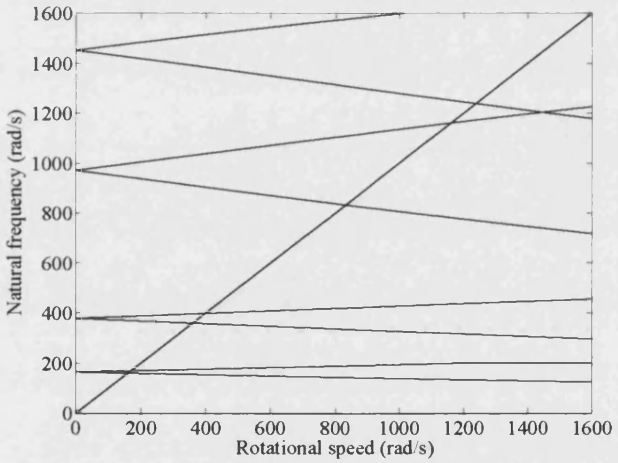

Figure 2.7: Critical speed map of the free-free rotor model

causes splitting of the modal frequencies. Figure 2.7 shows the speed dependence of the first four modes along with the synchronous line (Campbell diagram), evaluated using 14 elements.

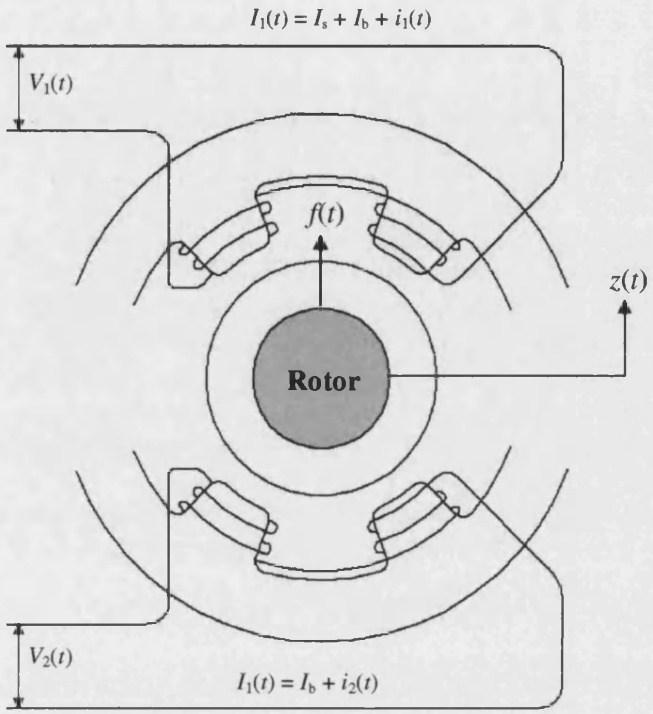

Figure 2.8: Opposing electromagnetic coil pairs. $f(t)$ denotes the force acting on the rotor and $z(t)$ is the rotor displacement. $I_1(t)$ and $I_2(t)$ are the currents in the coils due to voltages $V_1(t)$ and $V_2(t)$.

2.3 Active Magnetic Bearings

Active magnetic bearings consist of an array of electromagnetics. The basic principle of operation is to apply an electromagnetic force in order to achieve rotor levitation and to provide control forces to the system. Rotor levitation is dictated by the static performance of the active magnetic bearing while the control forces are dictated by the dynamic performance. The properties of active magnetic bearings are governed by the laws of electromagnetism and need to be understood in to order fully model the system and evaluate a control strategy. The rotor is supported by two similar radial magnetic bearings (figure 2.1). A schematic diagram of an individual active magnetic bearing is shown in figure 2.8. Specification of the active magnetic bearings is given in Table 2.2.

The currents in a pair of opposing coils can be described as $I_1(t) = I_s + I_b + i_1(t)$

and $I_2(t) = I_b + i_2(t)$, where the current I_s is necessary to levitate the rotor, I_b is the bias current, and $i_1(t)$ and $i_2(t)$ correspond to the control currents. The net force due to a pair of opposing coils can be expressed as, Hammond [56]:

$$F = F_1 - F_2 = \frac{A}{\mu_0}\left(B_1^2 - B_2^2\right) \tag{2.31}$$

where the flux densities, $B_{1,2}$, are given by Ampère's law:

$$B_1 = \frac{\mu_0 N I_1}{c_g + l_g} \qquad B_2 = \frac{\mu_0 N I_2}{c_g - l_g} \tag{2.32}$$

l_g is the deviation of the rotor from the static air gap given by c_g. The air gap between the rotor and the top and bottom electromagnets can therefore be expressed as $c_g - l_g$ and $c_g + l_g$ respectively. The net force due to both electromagnetic can now be evaluated by combining equations (2.31) and (2.32) as:

$$F = \mu_0 N^2 A \left[\left(\frac{I_s + I_b + i_1}{c_g + l_g}\right)^2 - \left(\frac{I_b + i_2}{c_g - l_g}\right)^2\right] \tag{2.33}$$

Equation (2.33) can be arranged so that $i_1 = -i_2$, then the available control force

Table 2.2: Magnetic bearing design parameters.

Parameter	Value
Pole face area	1398 mm^2
Number of turns per pole	158
Coil resistance	0.365 Ω per coil
Coil inductance	0.0732 H
Coil cut-off frequency	30.5 rad/s
Time constant	0.206 s
Peak coil current	10 A
Peak voltage	95.2 V
Peak power	952 W
Maximum air gap	1.6 mm
Nominal air gap	1.2 mm
Saturation flux density	1.2 T

of the opposing coils is shown in figure 2.9. This relationship is linear for zero rotor displacement, $l_g = 0$, and approximately linear for small rotor displacements. This is a convenient relationship and is often used for active magnetic bearing representation. The relation between the force and the rotor displacement is shown in figure 2.9. Linearizing equation (2.31) gives $F = F_0 + f$ where

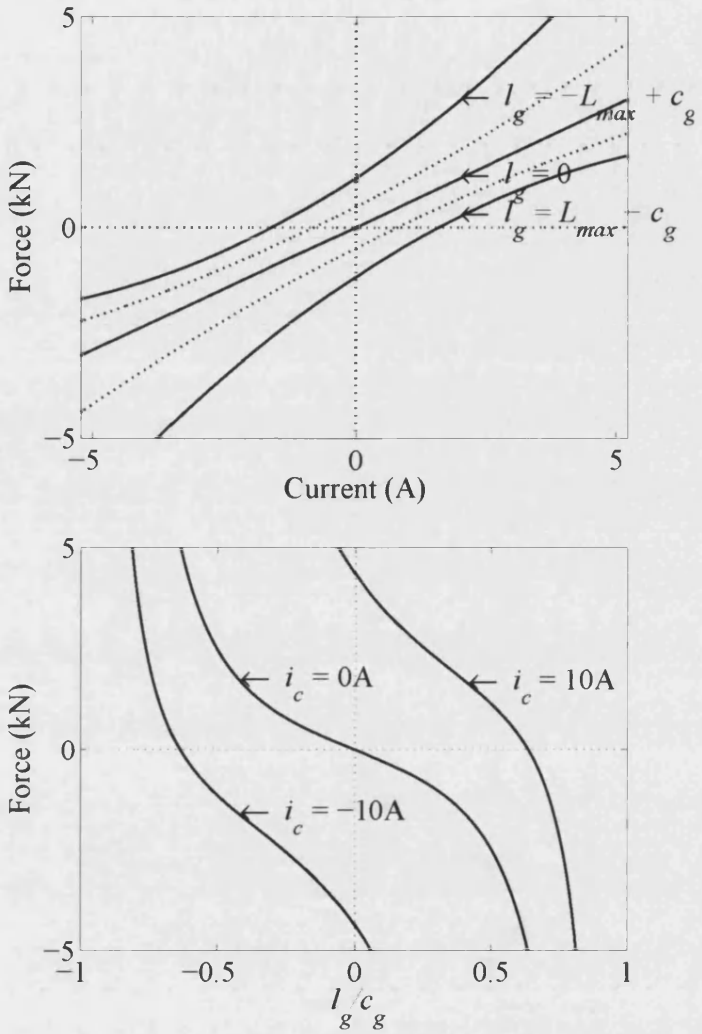

Figure 2.9: Available control force against current and rotor displacement, l_g/c_g, for an opposing coil pair with parameters given in Table 2.2.

$$f = \frac{2A}{\mu_0}(B_{10}b_1 - B_{20}b_2) \tag{2.34}$$

and

$$B_{10} = \frac{\mu_0 N}{c_g}(I_s + I_b), \qquad B_{20} = \frac{\mu_0 N I_b}{c_g}, \tag{2.35}$$

$$b_1 = B_{10}\left[\frac{i_1}{I_s + I_b} - \frac{l_g}{c_g}\right], \qquad b_2 = B_{20}\left[\frac{i_1}{I_b} - \frac{l_g}{c_g}\right], \tag{2.36}$$

F_0 represents the static performance and is dictated by the bias current, I_b, and current required to levitate the rotor, I_s. The control force, f, is also dependent on the control currents $i_{1,2}$. Substituting (2.35) and (2.36) into (2.34), the control force is given as

$$f = K_1 i_1 - K_2 i_2 - K_z l_g \tag{2.37}$$

where

$$K_1 = \frac{2\mu_0 N^2 A}{c_g^2}(I_s + I_b), \quad K_2 = \frac{2\mu_0 N^2 A I_b}{c_g^2} \tag{2.38}$$

and

$$K_z = \frac{2\mu_0 N^2 A}{c_g^3}\left[(I_s + I_b)^2 + I_b^2\right] \tag{2.39}$$

K_z relates the force due to rotor displacement and is accordingly known as the negative stiffness. When the control currents are constrained by $i_1 = -i_2$ (as for opposing pairs) the current gain is:

$$K_{i_1} = \frac{2\mu_0 N^2 A}{c_g^2}(I_s + 2I_b) \tag{2.40}$$

The negative stiffness and the current gain evaluated with the parameters in Table 2.2 are $K_z = 2240$N/mm and $K_i = 572$N/A. Experimental validation of the active magnetic bearings was performed by Rutland and Keogh [50]. This was performed on each magnetic bearing individually by measuring the change in force acting on the rotor with variation of rotor position and control current. A constant bias current providing a force of 325N was required to levitate the rotor. The current gains for both active magnetic bearing are shown in figure 2.10. A least-squares fit to the data over the range $\pm$2V gives the current gains as 539N/A and 544N/A, [50]. The negative stiffness was evaluated from the variation in force due to a change in rotor position (figure 2.11). The negative stiffnesses for the magnetic bearings were identified with least-squares fits over the range $\pm$0.5mm as 2156N/mm and 1994N/mm.

Although Rutland and Keogh perform experimental validation of the current gain and negative stiffness, no error bounds are presented. Furthermore, Rutland and Keogh only consider the active magnetic bearing in the vertical direction (figure 2.8). Consideration of the characteristics normal to the vertical would give cross coupled properties. An alternative method of modelling the current-force-displacement characteristics of an active magnetic bearing from the magnetic flux distribution is presented by Knight *et al.* [57].

The current flow through the active magnetic bearings is dictated by the voltage across the bearings and by their resistance and inductance. They can be related by

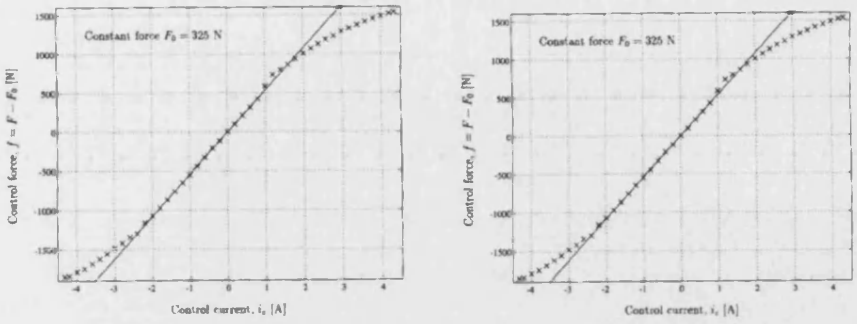

Figure 2.10: Force current characteristic for both active magnetic bearings. Crosses are experimental data, straight lines are least-squares fits to the data over a range of ±2A. The gradient of the straight lines are 539N/A and 544N/A. These results are taken from Rutland and Keogh [50]

Faraday's law (Hammond, [56]) as

$$v_{1,2}(t) = i_{1,2}(t)R + 2NA\frac{db_{1,2}}{dt} \tag{2.41}$$

giving

$$v_{1,2}(t) = i_{1,2}(t)R + L\frac{di_{1,2}}{dt} \tag{2.42}$$

where R is the coil resistance and L is the coil inductance given by

$$L = \frac{2\mu_0 N^2 A}{c_g} \tag{2.43}$$

The time constant and coil cut-off frequency are given as:

$$T = \frac{L}{R} = 0.206\text{s}, \qquad w = \frac{2\pi}{T} = 30.5\text{rad/s} \tag{2.44}$$

2.4 Power Electronics

The active magnetic bearings are driven by eight switching amplifiers. These can be viewed simply as gains between the controller outputs and the inputs to the active magnetic bearings. However, in reality the situation is more complicated. The amplifiers operate by switching between a positive and negative voltage at a set frequency, in this case 10KHz. The ratio of the time spent between positive and negative values is dictated by the current to be amplified. Positive current is

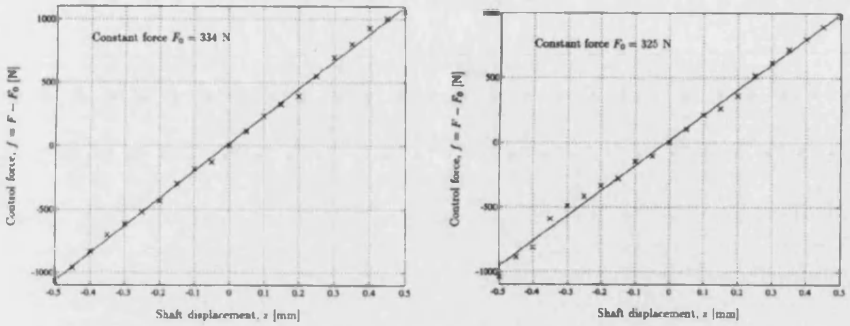

Figure 2.11: Force displacement characteristic for both active magnetic bearings. Crosses show experimental data, straight lines show least-squares fits to the data over the range ±0.5mm with gradients 2156N/mm and 1994N/mm. These results are taken from Rutland and Keogh [50]

achieved by spending more time at the positive voltage relative to the negative, and visa versa for negative currents. Larger currents are specified by increasing this difference. Due to the switching involved in amplifying the control currents will contain high frequency noise.

To produce an accurate model of the system the characteristics between the switching amplifiers and the active magnetic bearing coils must be understood. This can be achieved by identifying the static and dynamic bearing force measurements and their dependence on control current. This could form part to the full system model. The operating bandwidth of the active magnetic bearings is limited by their voltage-flux frequency response. It is assumed that over this operating frequency range the amplifier-coil current gain is constant.

2.5 Controller Hardware Specification

In order to implement a control strategy a microprocessor is used. Figure 2.12 show a schematic block diagram of the full system including power electronics and controller hardware.

Initial controller design in performed on a standard desktop personal computer (PC) using Matlab® and Simulink®. The desktop PC is connected to dSPACE hardware through a fibre optic cable. This allows the PC to read and write data, including the controller program, to the dSPACE memory. The exchange of data also allows the PC to operate as a user interface. The PC can vary parameters within the

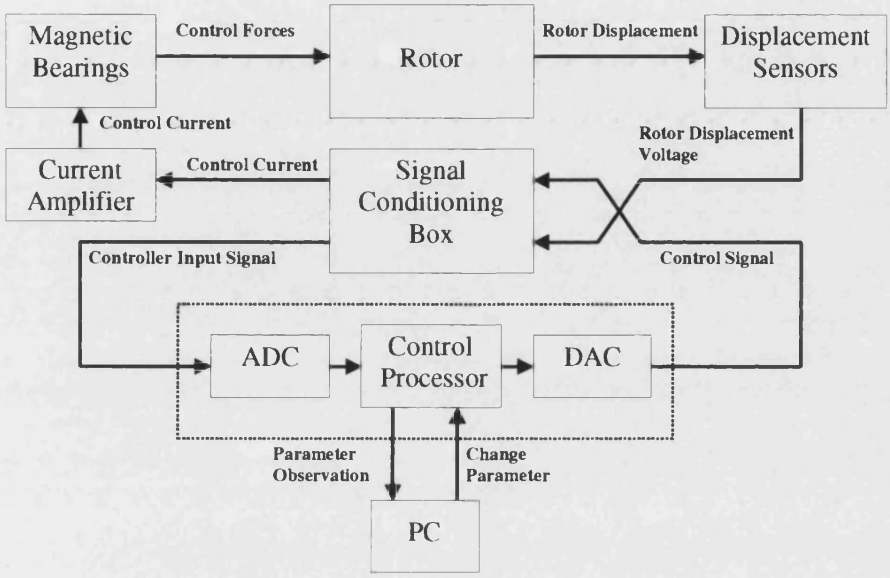

Figure 2.12: Schematic diagram showing full signal/measurement flow

control strategy or display/measure/record data such as rotor displacement, control currents and controller parameters etc.

The dSPACE processor card, DS1005, provides the computing power for the controller. The DS1005 card operates with an IBM PowerPC 750GX microprocessor operating at 1GHz. It has 128MB SDRAM global memory and 16MB flash memory for user specified applications. The analogue input signal must be converted into a digital signal using an analogue-digital-converter (ADC) before any computational manipulation can occur. The dSPACE contains an ADC card, DS2002, with 32 input channels with a maximum of 16bit resolution and minimum sample time of 5.0μs. The ADC has an input voltage range of ± 5 or ± 10V. The output from the dSPACE microprocessor must conversely be converted from digital to analogue to form the control signal. This is achieved using a digital-analogue-converter (DAC). The DAC card, DS2103, has 32 output channels with 200ns resolution.

The controller hardware is limited by the input and output voltage ranges of the analogue-digital and digital-analogue converters. The measured displacement signals are conditioned to provide signals suitable for analogue-digital conversion. The output control signals are conditioned to provide suitable control currents prior to amplification.

2.6 Closed Loop Properties

Initial rotor stabilization is achieved using a combination of proportional, integral and differential control action (PID). This provides an initially stable system if there is sufficient proportional control to overcome the negative stiffness. This is useful technique to employ as the PID controlled rotor/active magnetic bearing system can have additional control action applied in parallel. The PID controller is configured such that controller inputs are taken from the inner sensors adjacent to the active magnetic bearings (figure 2.1). The PID controller can be represented in state space form, indicated using the subscript k, with the rotor displacement vector $\mathbf{y}_k$ forming the input and outputting a control force $\mathbf{u}_k$ as

$$\dot{\mathbf{x}}_k = \mathbf{A}_k\mathbf{x}_k + \mathbf{B}_k\mathbf{y}_k \tag{2.45}$$

$$\mathbf{u}_k = \mathbf{C}_k\mathbf{x}_k + \mathbf{D}_k\mathbf{y}_k \tag{2.46}$$

The rotor/PID model can be identified by combining the rotor and PID system states as $\tilde{\mathbf{x}} = [\mathbf{x}^T \quad \mathbf{x}_k^T]^T$. This can be expressed in state space form, where $\mathbf{f}$ represents a disturbance force acting on the system, as

$$\begin{bmatrix} \dot{\mathbf{x}} \\ \dot{\mathbf{x}}_k \end{bmatrix} = \begin{bmatrix} \mathbf{A} - \mathbf{B}\mathbf{D}_k\mathbf{C} & -\mathbf{B}\mathbf{C}_k \\ \mathbf{B}_k\mathbf{C} & \mathbf{A}_k \end{bmatrix} \begin{bmatrix} \mathbf{x} \\ \mathbf{x}_k \end{bmatrix} + \begin{bmatrix} \mathbf{B} \\ \mathbf{B}_k\mathbf{D}_k \end{bmatrix} \mathbf{y}_k + \begin{bmatrix} \mathbf{B} \\ \mathbf{0} \end{bmatrix} \mathbf{f} \tag{2.47}$$

$$\mathbf{u} = [\mathbf{C} \quad \mathbf{0}] \begin{bmatrix} \dot{\mathbf{x}} \\ \dot{\mathbf{x}}_k \end{bmatrix} + [\mathbf{D}]\mathbf{y}_k \tag{2.48}$$

When the PID gains are zero the system is initially unstable due to negative stiffness associated with the active magnetic bearings. There must therefore be sufficient proportional gain to overcome the negative stiffness in order to achieve stability. Figure 2.13 shows the change in natural frequency of the first five zero speed mode shapes of the rotor as a function of proportional gain, with integral and differential control gains set to zero. Without control the first two mode shapes occur at 0Hz. These are the conical and cylindrical mode shapes and correspond to translational modes of vibration. When the proportional gain is sufficient, the first two natural frequencies become non-zero and the system is stabilized. The proportional gain required to stabilize the system is larger than the negative stiffness due to the difference in location of the feedback sensors and the active magnetic bearings.

The PID control parameters are dictated by the desired system performance and limitations of the magnetic bearings:

- The design dictates the first two flexible modes of rotor vibration are reasonably damped and below the maximum operating speed of the motor, 100Hz.
- The minimum proportional gain must overcome the negative stiffness.
- The maximum differential gain is dictated by the performance limitations

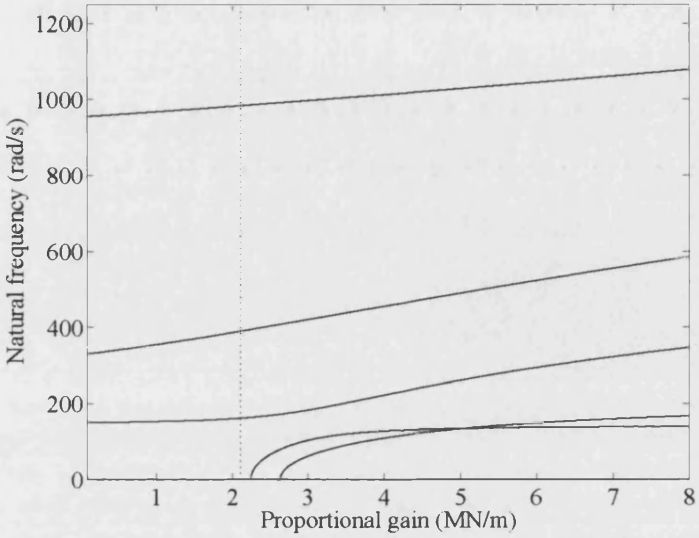

Figure 2.13: Natural frequencies as a function of proportional gain.

of the magnetic bearings. The maximum control force that can be applied through each magnetic bearing is 1KN. The rotor clearance is 750μm giving a maximum rotor movement of 1.5mm. The differential control parameter is therefore specified in the Laplace domain by $k_d s/(1+\tau s)$, where τ is a cut-off frequency used to ensure the system is realizable.

- An integral gain is included to ensure zero steady state error.

The system PID control parameters are specified in Table 2.3. A differential cut-off frequency is applied to the controller in accordance with the roll-off of the magnetic bearings. A bode plot for the PID controller is shown in figure 2.14. The singular values are shown as a function of frequency for the system model in figure (2.16). The first four mode shapes are also presented. These are the two mainly rigid body modes and the first two dominantly flexible modes of vibration, figure 2.15.

Table 2.3: PID controller parameters.

Parameter	Value
Proportional gain	3.0 MN/m
Integral gain	0.1 MN/ms
Differential gain	0.003 KNs/m
Differential gain cut-off frequency	1500 rad/s

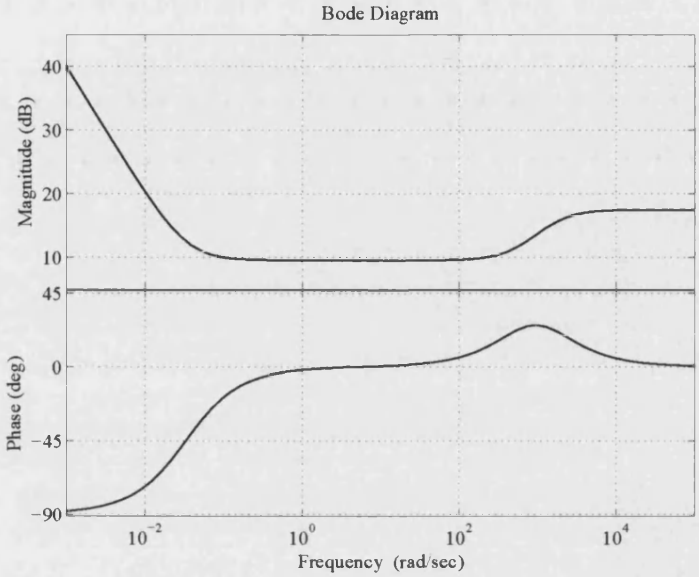

Figure 2.14: Bode plot for control parameters specified in Table 2.3.

2.7 System Identification

In order to validate the closed-loop system model, system identification was undertaken experimentally. There are many different method of identifying a system including comparison of power spectral densities. A simple method is to identify the gain matrix from input disturbance to output displacement for a range of frequencies. Consider the state space system

$$\dot{\mathbf{x}}(t) = \mathbf{A}\mathbf{x}(t) + \mathbf{B}\mathbf{u}(t) \tag{2.49}$$

$$\mathbf{y}(t) = \mathbf{C}\mathbf{x}(t) + \mathbf{D}\mathbf{u}(t) \tag{2.50}$$

where $\mathbf{D} = \mathbf{0}$. The system is disturbed with a periodic time varying signal, $\mathbf{u}(t)$, such that the steady state system response, $\mathbf{x}(t)$, will also be a periodic time varying signal, i.e.

$$\mathbf{u}(t) = \mathbf{U}e^{i\omega t}, \qquad \mathbf{x}(t) = \mathbf{X}e^{i\omega t}, \qquad \mathbf{y}(t) = \mathbf{Y}e^{i\omega t} \tag{2.51}$$

Equations (2.49) and (2.50) can be expressed as

$$\mathbf{X} = [i\omega\mathbf{I} - \mathbf{A}]^{-1}\,\mathbf{B}\mathbf{U} \tag{2.52}$$

$$\mathbf{Y} = \mathbf{C}\,[i\omega\mathbf{I} - \mathbf{A}]^{-1}\,\mathbf{B}\mathbf{U} \tag{2.53}$$

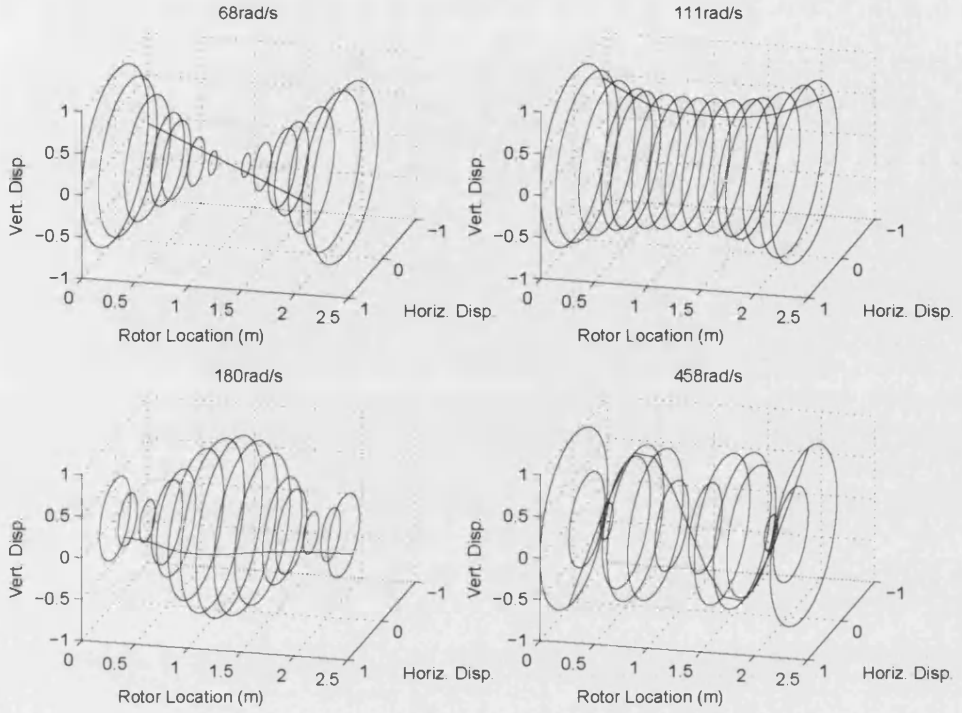

Figure 2.15: PID controlled rotor mode shapes

The transfer function from $\mathbf{U}$ to $\mathbf{Y}$ represents the system frequency response through

$$\mathbf{G}(i\omega) = \mathbf{C}\left[i\omega\mathbf{I} - \mathbf{A}\right]^{-1} \tag{2.54}$$

$\mathbf{G}(i\omega)$ represents the frequency dependent gain matrix from input disturbance to output displacement and can be identified experimentally. Figure 2.17 shows the measured singular values of $\mathbf{G}(i\omega)$ along with the predicted singular value response of the system.

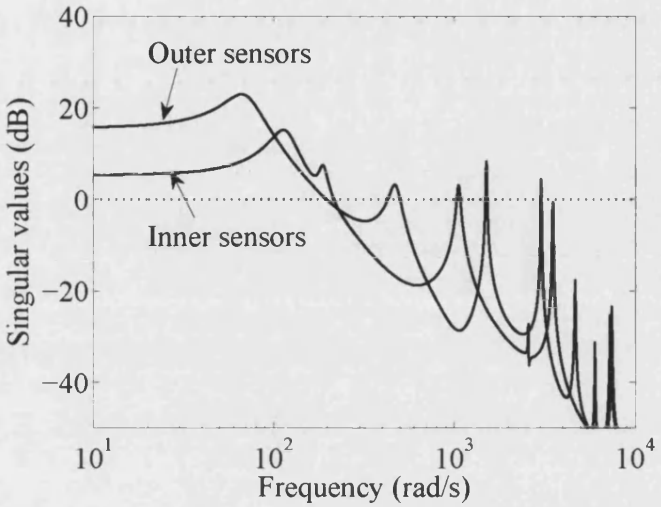

Figure 2.16: Rotor PID model singular values from active magnetic bearing to measurement sensor.

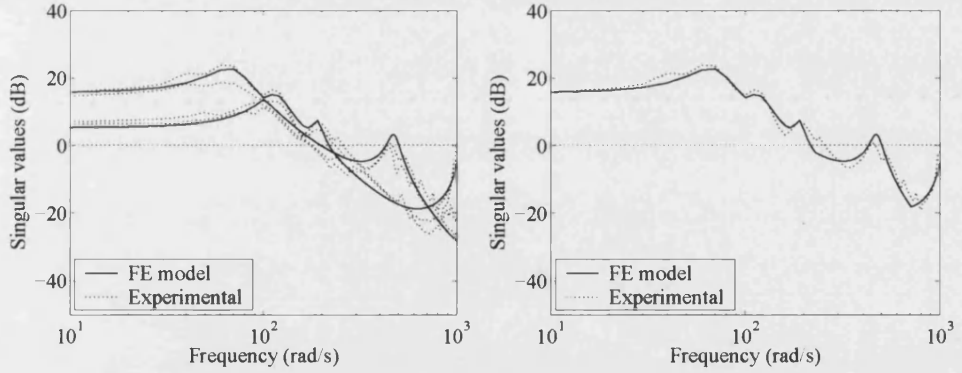

Figure 2.17: Predicted and measured singular value response (left) of the rotor/active magnetic bearing system and maximum singular values (right).

2.8 Closure

In order to design a control strategy or understand the system dynamics it is important to have an accurate model. This chapter considers the whole rotor/active magnetic bearing rig including the control systems and power amplifiers. Although this is a specific example the techniques are general and applicable to all rotor/magnetic bearing systems.

The rotor was represented using finite elements to produce a linear dynamic model. A theoretical examination of the active magnetic bearing was performed identifying the current gain and the negative stiffness. Experimental validation undertaken by Rutland and Keogh [52] is also presented for completeness. The rotor/active magnetic bearing system was combined with a PID controller to provide an initially stable closed loop system. The mode shapes, critical frequencies and singular values were identified.

Chapter 3

ROTOR/MAGNETIC BEARING FAULTS

3.1 Introduction

The safe operation a of rotor/magnetic bearing system is dependent upon the response to external and internal fault conditions along with system disturbances. A discussion of safety and reliability in active magnetic bearings is presented in [58]. Fault-tolerant control can be ensured by either designing a controller robust to fault conditions or reconfiguring a controller to take account of the fault condition. The latter requires knowledge of the fault onset time and type.

3.2 Rotor/Magnetic Bearing Faults

When designing a rotor/active magnetic system or a robust fault tolerant controller it is important to have an understanding of possible faults and their corresponding consequences. Fault conditions can be classified as either internal or external to the system.

3.2.1 Internal Faults

Internal faults are associated with failure of the system or its components. There is an unlimited number of possible fault conditions that can occur. The main components of the system will be considered with the exception of signal transmission lines. These are considered as part of the sensors, control hardware and power electronics due to their similarities in failure. The faults are discussed along with their

consequences for system stability. A summary of internal rotor/magnetic bearing fault conditions is shown in Table 3.1

Sensor Failure

The displacement of the rotor is measured using a number of sensors positioned along it. Failure of a sensor to measure the displacement accurately may arise from damage or shifting of the sensor, or the sensor signal may be corrupted along its transmission line. The extent of the signal corruption may be small, or extreme when the signal fails completely. Examples of these include small sensor dislocation or severe sensor damage. Noise may also be present in the signal.

In the case of a significantly damaged sensor or short circuit, in the sensor or the transmission line, the measured signal will be significantly offset, or zero. Corruption of the sensor signal can occur anywhere between its measurement point and the controller. It is possible for damage to occur at the sensor surface, including the build up of debris, or for the signal to become significantly noisy.

It is common for there to be redundancy in the number of sensors used. Therefore, complete failure of a sensor or the corruption of a sensor signal is not a significant problem provided it can be identified. In a system without sensor redundancy complete failure will result in failure of a control axis. System robustness to noise can be accounted for during controller design.

Power Electronics

The demand control current signal is amplified by the power amplifier to provide sufficient current for a active magnetic bearing. Failure can occur before or after the amplifier in the transmission lines. Failure of a transmission line will result in zero control current to the magnetic bearing. In the case of opposing coil pairs then failure of a single pole will result in an uncompensated attractive force due to the single working pole. This will result in rotor/auxiliary bearing contact. The power electronics usually include their own internal closed loop system and are inherently reliable. However, over loading may result in trip outs resulting in zero control current at an active magnetic bearing pole. This will have the same effect as a failure in a control current transmission line.

Magnetic Bearing/Coil Failure

Failure of an active magnetic bearing or electromagnetic coil is an uncommon problem, however, it is possible for damage to occur resulting in a short circuit inside

Table 3.1: Summary of internal fault conditions.

Fault Area	Fault Characteristics	System Response
Power electronics	Loss of magnetic bearing pole(s)	Rotor/auxiliary bearing contact
Magnetic bearing/coil failure	Loss of magnetic bearing pole(s)	Rotor/auxiliary bearing contact
Sensor failure	Inconsistent or constant sensor signal	Reduced performance
Control hardware failure	Failure to evaluate control currents	System instability
Control software failure	Incorrectly evaluated control currents	Possible system instability

a coil or complete coil failure. A short circuit will reduce the number of effective windings and therefore the maximum operational control force. Complete failure of an individual coil can be considered as similar to failure of the power electronics resulting in rotor/auxiliary bearing contact.

Controller Hardware/Software Failure

Controller hardware failure will result in a computational inability to update the demand control currents. This will cause system instability. Secondary controller hardware acting as a reserve may provide a solution. Failure of the software can occur in a number of different ways including failure to evaluate the control currents in sufficient time, programming errors and numerical computation errors. The result of software failure on the control signal can result in a small loss of system performance or complete control system failure. These issues are best addressed at the controller design stage and are arguably avoidable.

3.2.2 External Faults

External faults can be characterized by a fault condition originating from outside the system. It can also be applied to fault conditions which, although internal to the system, can be modelled as occurring outside the system. External faults will always

result in transient rotor vibration and often have a steady state component. Some of the main fault conditions are discussed below along with a description of their associated forces. A summary of external rotor/magnetic bearing fault conditions is shown in Table 3.2.

Rotor Contact

Auxiliary/retainer bearings are present within in the system to prevent rotor contact with the active magnetic bearing lamination stacks. They can also be present to limit the rotor vibration to ensure safe operating conditions. It should therefore be expected that contact between the rotor and auxiliary bearings may be a common occurrence during a fault condition. Rotor contacts may also occur as a result of system operation. In the case of pumps a foreign object present in the fluid flow may impact with the rotor or turbine blades resulting in a contact. The control issues involved in rotor/auxiliary bearing contact are considered in [59–61].

Rotor Faults

The rotor is an integral working part of rotor/magnetic bearings and can therefore be subjected to damage and wear. Examples of rotor damage include cracking, deformation, and mass-loss. Rotor cracks and deformation can both be considered as variation of the system parameters. It is therefore possible, within reason, to maintain system stability using robust controller design. Mass-loss, and also rotor deformation, can result in rotor unbalance due to a shift in the centre of mass. It can therefore be considered as a disturbance force. A change in rotor unbalance can occur progressively or suddenly, an example of the latter is a sudden rotor mass-loss. Rotors used in pumps may suffer progressive blade deposition or blade erosion/wear.

Consider a small change in the centre of mass of the rotor at a finite element node (figure 3.1). The dynamic equation of motion of the system, equation (2.14), can be modified to account for the change in the centre of mass as,

$$\mathbf{M}\frac{d^2}{dt^2}\left(\mathbf{x}-\mathbf{M}^{-1}\mathbf{B}_{ml}mee^{i\Omega t}\right)+(\Omega\mathbf{G}+\mathbf{C})\,\dot{\mathbf{x}}+\mathbf{K}\mathbf{x}=\mathbf{B}_f\mathbf{f}+\mathbf{B}_u\mathbf{u} \tag{3.1}$$

where $\mathbf{B}_{ml}$ is a force distribution matrix introduced to match the scalar mass-loss disturbance force to that of $\mathbf{x}$. Evaluating the modified mass term

$$\mathbf{M}\frac{d^2}{dt^2}\left(\mathbf{x}+\mathbf{M}^{-1}\mathbf{B}_{ml}mee^{i\Omega t}\right)=\mathbf{M}\ddot{\mathbf{x}}+\mathbf{B}_{ml}me\Omega^2e^{i\Omega t} \tag{3.2}$$

The dynamic equation of motion of the system can be expressed as

$$\mathbf{M}\ddot{\mathbf{x}}+(\Omega\mathbf{G}+\mathbf{C})\dot{\mathbf{x}}+\mathbf{K}\mathbf{x}=\mathbf{B}_{ml}me\Omega^2e^{i\Omega t}+\mathbf{B}_u\mathbf{u} \tag{3.3}$$

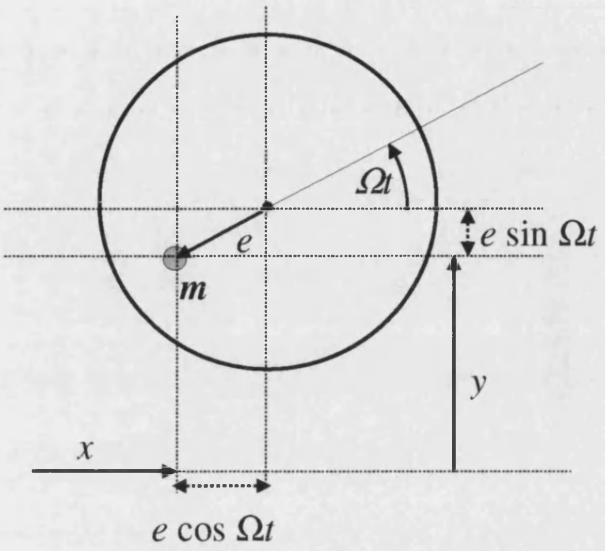

Figure 3.1: Schematic diagram showing rotor unbalance.

In the case of a sudden change in rotor unbalance the synchronous disturbance can be expressed as $\mathbf{B}_{ml} m e \Omega^2 e^{i\Omega t} H(t)$, where $H(t)$ is the Heaviside step function. Forces associated with rotor unbalance and mass-loss disturbance can be compensated for if the active magnetic bearings can provide sufficient control forces.

Rotor Load

The load on the rotor in pump applications is dependent on the fluid flow through the system. Sudden changes in the fluid flow will result in sudden variation of axial loading. The loading characteristics may also vary due to changes in the rotor condition such as due to cracks and other damage. These can occur suddenly or progressively. Within reason, it is possible to design multi-variable control strategies robust to changes in the system parameters, allowing for continued safe operation.

Base Motion

Transmitted forces arising from motion of the housing relative to the rotor can be a common problem in transport applications. It is also possible that base motion may

Table 3.2: Summary of external fault conditions.

Fault Area	Fault Characteristics	System Response
Rotor damage	Forcing on rotor	Transient and steady state vibration
Mass-loss	Synchronous forcing on rotor	Transient and steady state vibration
Base motion	Typically low frequency due to seismic activity	Transient and steady state vibration
Rotor contact	Impulse force	Transient vibration
Sudden/progressive change in rotor load	Sudden/progressive change in rotor disturbance force	Transient and steady state vibration

occur due to movement of a normally static environment, such as a building during seismic activity. Base motion arising from vibrating machinery in close proximity may also be present.

Base motion can be considered as a disturbance force acting on the rotor. Starting with

$$\mathbf{M}\ddot{\mathbf{x}} + (\Omega\mathbf{G} + \mathbf{C})\dot{\mathbf{x}} + \mathbf{K}\mathbf{x} = \mathbf{B}_f\mathbf{f} + \mathbf{B}_u\mathbf{u} \tag{3.4}$$

The motion of the base, $\mathbf{y}(t)$, can be incorporated into the system modelling as a translation in the displacement terms relating to the stiffness and damping:

$$\mathbf{M}\ddot{\mathbf{x}} + (\Omega\mathbf{G} + \mathbf{C})(\dot{\mathbf{x}} - \dot{\mathbf{y}}) + \mathbf{K}(\mathbf{x} - \mathbf{y}) = \mathbf{B}_f\mathbf{f} + \mathbf{B}_u\mathbf{u} \tag{3.5}$$

Making the transformation $\mathbf{r} = \mathbf{x} - \mathbf{y}$ then

$$\mathbf{M}\ddot{\mathbf{r}} + (\Omega\mathbf{G} + \mathbf{C})\dot{\mathbf{r}} + \mathbf{K}\mathbf{r} = \mathbf{B}_f\mathbf{f} + \mathbf{B}_u\mathbf{u} - \mathbf{M}\ddot{\mathbf{y}} \tag{3.6}$$

where $\mathbf{r}$ represents the motion of the rotor relative to the base.

3.3 Fault Tolerant Control

Control strategies designed to provide robust control during fault conditions fall into two categories, namely, those which are robust to the fault and those which reconfigure themselves to compensate for the fault.

3.3.1 Robust Control

Robust control strategies are based around a desired performance characteristic of a plant. Consideration of variations in the plant leads to the identification of a nominal plant and plant perturbation, which are then accounted for in the robustness criteria. The performance can then be optimized. This forms a combined performance/robustness problem. Full discussions, and design methods, for robust multi-variable controllers can be found in [62–64].

The H_∞ control problem has been applied to many rotor/magnetic bearing systems and is well documented. Robust control using H_∞ controller design can be achieved by applying a bound to the H_∞ norm of the plant sensitivity function. Robustness is ensured by applying bounds to the H_∞ norms of the control sensitivity and the complementary sensitivity functions. These can also be considered to represent the multiplicative and additive plant uncertainties, respectively. Favourable results have also been shown in rotor/magnetic bearing systems using μ synthesis [17]. In this case a more accurate representation of the plant is derived from an understanding of variation of the system parameters.

There is, however, an inherent compromise between the system performance and its robustness to variations in the plant. As the uncertainty in the plant increases the system will become more conservative. Therefore, in order to design a controller robust to large plant perturbations the controller will have limited performance and may not be suitable. It may even fail to stabilize the system during normal operation.

3.3.2 Reconfigurable Control

In the case of robust control, a single controller is designed to ensure system stability for a variety of plant perturbations, though at the cost of reduced performance. An alternative approach is to have multiple controllers designed to stabilize a number of perturbed plants and using the control signal most suited to system. The advantage of reconfigurable control strategies is that each controller can provide optimum performance for each variation of the plant parameters. The drawback is that it is essential to use the correct controller. A method of fault detection is therefore required to quickly and accurately evaluate any fault conditions within the system.

3.4 Fault Detection

Fault identification/detection is an important aspect of modern machinery allowing for improved maintenance monitoring, fault tolerance and condition monitoring.

Fault detection is also an important aspect of reconfigurable control, to enable control to be changed at the onset of a fault condition. There are many different ways to identify fault onset and type.

Trend checking approaches are the simplest methods of fault identification. In the most basic cases they may be simple parameter thresholds. More complicated approaches identify fault onset and type from artifacts present in the frequency domain of a measured signal. A frequency domain approach to identify different fault conditions in electric motors, such as rotor stator contact, is given in [65]. These methods are reliable and offer high speed identification, however, they are only able to react to a significant change in the system behaviour.

Model based fault identification through parameter estimation in dynamic systems is presented by Isermann [66]. This technique is best suited to systems having slow dynamic characteristics and fault conditions can occur by suddenly changing the plant parameters. Examples include chemical processing and nuclear reactors. Model based control offers improvements over trend checkers during subtle fault conditions, however, an accurate representation of the linear model is required. Fault identification using neural networks as decision makers has also been documented [19].

3.5 Closure

Specific internal and external fault conditions within rotor/active magnetic bearings systems and their consequences have been considered. These include failure of sensors, coils, power electronics, together with rotor contact, base motion and rotor damage.

Control of rotor/active magnetic bearing systems can be achieved by the application of a fault tolerant control strategy or by reconfiguring the system controller to one more suited to the fault condition. The latter method overcomes problems associated with overly conservative fault tolerant control due to the performance robustness compromise. However, it is dependent on fast and accurate fault identification.

Chapter 4

WAVELET ANALYSIS AND FILTERBANKS

4.1 Introduction

This chapter gives an overview of the techniques used in wavelet analysis, the implementation of digital filterbanks, and a discussion about the choice of wavelet family. Wavelet analysis and filterbanks are well understood and accordingly there is a large amount of published literature. Therefore, only the most significant details are considered along with the techniques required for practical implementation. Full discussions can be found in [67–69].

Wavelet analysis is similar to Fourier Analysis in its approach. However, unlike Fourier analysis, wavelet analysis is a compromise between resolution in time and frequency. The basis functions are no longer *sines* and *cosines* and are replaced by more complicated waveforms. The basis functions used in Fourier analysis are pure harmonics and have infinite duration. This provides perfect resolution in frequency, however, it offers no indication of when that frequency may have occurred. The basis functions used in wavelet analysis, derived from the mother wavelet, have zero mean and are only non-zero for a finite time period. That wavelets have zero mean implies that they must be oscillatory in nature. This provides resolution in frequency. That they are only non-zero for a finite period provides resolution in time. The total resolution achievable in time and frequency is subject to an uncertainty principle.

Wavelet analysis provides a technique of identifying what frequencies are present and when they occur in a vibrator signal. However, wavelet analysis may also be a more natural method for analyzing transient rotor vibrations. Consider a sudden change in rotor unbalance. The steady state vibration will be a synchronous harmonic dictated by the operating speed. However, during the transient period immediately

after the change in forcing the rotor vibration will contain many different frequencies. This is reflected in the multi-frequency content present in the mother wavelet.

A discussion is made as to what makes a good wavelet, and more importantly, what makes a good wavelet for the analysis of rotor/magnetic bearing systems. Consideration is made to the construction of the most common families of wavelets including Daubechies, Coifman and Symlets [69]. Measures of the resolving power of the wavelets are examined. From an understanding of rotor/magnetic bearing systems the wavelets most suited to analysis and control are identified.

4.2 Wavelet Analysis

4.2.1 The Wavelet Transform

Wavelet analysis provides a multi-resolution time-frequency analysis of a signal. This is achieved by evaluating a signal with an appropriate mother wavelet at different translations and dilations. The mother wavelet, $\psi(t)$, has zero mean:

$$\int_{-\infty}^{\infty} \psi(t)dt = 0 \tag{4.1}$$

The wavelet transform of the function $f(t)$ can be expressed as:

$$c(a,b) = |a|^{-1/2} \int_{-\infty}^{\infty} f(t)\psi\left(\frac{t-b}{a}\right) dt \tag{4.2}$$

where a and b give the dilation and translation of the wavelet respectively. Since wavelets are localized in both time and frequency this relates to the time window and pseudo-frequency. In a sampled system the wavelet coefficients, $c(a,b)$, can be evaluated on a discrete grid where a and b are assigned regularly spaced values: $a = ma_0$ and $b = nb_0$, where m and n are integer values.

4.2.2 Discrete Time Analysis Using the Haar Wavelet

Consider the simplest of wavelets, the Haar wavelet [67]. The Haar wavelet (figure 4.1) is defined in the continuous domain as

$$\psi(t) = \begin{cases} 1 & 0 \leq t < 1/2 \\ -1 & 1/2 \leq t < 1 \\ 0 & \text{otherwise} \end{cases} \tag{4.3}$$

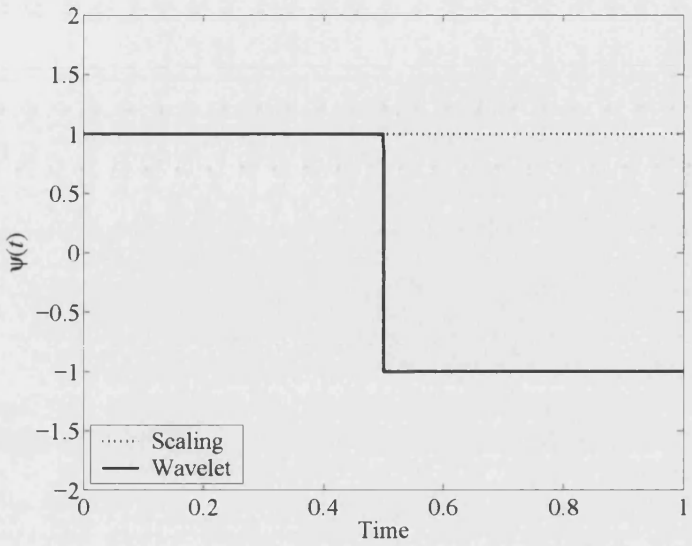

Figure 4.1: Haar wavelet.

In discrete time the Haar wavelet can be separated into even and odd (scaling and wavelet functions) basis functions respectively as

$$\psi_{2k}[n] = \begin{cases} 1/\sqrt{2} & n = 2k, \quad 2k+1, \\ 0 & \text{otherwise} \end{cases}, \qquad \psi_{2k+1}[n] = \begin{cases} 1/\sqrt{2} & n = 2k, \\ -1/\sqrt{2} & n = 2k+1, \\ 0 & \text{otherwise} \end{cases} \tag{4.4}$$

where k is used to specify the translation of the wavelet in discrete time, n. The pseudo-frequency of the wavelet is dictated by the sample time of n. For a wavelet filter duration of two time steps ($a = 2$), then the $|a|^{-1/2}$ term in equation (4.2) gives the $1/\sqrt{2}$. It can be seen from equation (4.4) that the basis functions are translations of themselves

$$\psi_{2k}[n] = \psi_{2k}[n-2k], \qquad \psi_{2k+1}[n-2k] = \psi_{2k+1}[n-2k] \tag{4.5}$$

The wavelet transform, equation (4.2), of a signal $x[n]$ is therefore

$$X[2k] = \frac{1}{\sqrt{2}}x[2k] + \frac{1}{\sqrt{2}}x[2k+1], \qquad X[2k+1] = \frac{1}{\sqrt{2}}x[2k] - \frac{1}{\sqrt{2}}x[2k+1] \tag{4.6}$$

This shows the two-point average and difference operation. The same argument can be followed using a filtering approach. Consider the filters $h_0[n]$ and $h_1[n]$ with

impulse responses

$$h_0[n] = \begin{cases} 1/\sqrt{2} & n = -1,\ 0, \\ 0 & \text{otherwise} \end{cases}, \qquad h_1[n] = \begin{cases} 1/\sqrt{2} & n = 0, \\ -1/\sqrt{2} & n = -1, \\ 0 & \text{otherwise} \end{cases} \tag{4.7}$$

These correspond to low pass and high pass filters, respectively. The average operation corresponds to a low pass filter averaging out high frequency components. The difference operation acts as a high pass filter extracting only high frequency information and ignoring long term behaviour. The convolution of a signal $x[n]$ with the filters at any $2k$ interval gives $X[2k]$ and $X[2k+1]$ as

$$\begin{aligned} h_0[n] * x[n]|_{2k} &= \sum_{k \in Z} h_0[2k-l]x[l] = \frac{1}{\sqrt{2}}x[2k] + \frac{1}{\sqrt{2}}x[2k+1] = X[2k] \\ h_1[n] * x[n]|_{2k} &= \sum_{k \in Z} h_1[2k-l]x[l] = \frac{1}{\sqrt{2}}x[2k] - \frac{1}{\sqrt{2}}x[2k+1] = X[2k+1] \end{aligned} \tag{4.8}$$

Filtering the signal $x[n]$ with $h_0[n]$ and $h_1[n]$ at even index corresponds to average and difference output signals down-sampled by two. This corresponds to the digital Haar wavelet analysis approach of equation (4.6). This process of filtering forms the basis of wavelet analysis. The original signal is filtered with a high and low pass filter, $h_0[n]$ and $h_1[n]$, and down-sampled by two. This filtering approach is often referred to as an analysis filter-bank. The original signal can be reconstructed from the sum of the wavelet coefficients and corresponding wavelet at any time giving:

$$x[n] = \sum_{k \in Z} X[k]\psi_k[n] \tag{4.9}$$

as with any orthonormal basis set. The reconstruction filters $g_0[n]$ and $g_1[n]$ are defined as

$$g_0[n] = \psi_{2k}[n], \qquad g_1[n] = \psi_{2k+1}[n], \tag{4.10}$$

Combining equations (4.9) and (4.10) with the output signals $X[2k]$ and $X[2k+1]$ gives

$$x[n] = \sum_{k \in Z} X[n-2k]\psi_{2k}[n] + X[2k+1]\psi_{2k+1}[n-2k] \tag{4.11}$$

The original signal can be reconstructed by filtering and up-sampling the low and high frequency signals. Up-sampling a signal is performed by inserting a zero between adjacent sample intervals and halving the sample time. This forms the basics of digital wavelet analysis using filterbanks. In this case the Haar wavelet has been used to decompose the signal into two output signals corresponding to the output from a high or low pass filter down-sampled by two. The high pass signal corresponds to the wavelet coefficient and the low pass output forms a residue signal. It has also been shown that the original signal can be fully reconstructed using the Haar wavelet. This is referred to as synthesis. Similar arguments considering other mother wavelets can be found in [67,68].

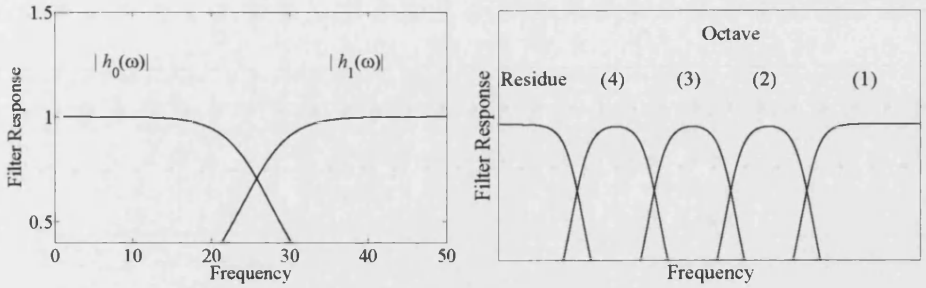

Figure 4.2: Filterbank frequency response (left), multi-level filterbank frequency response (right).

4.2.3 Wavelet Filter-Bank Analysis

The twin channel filtering described separates the input signal into two output signals containing high and low frequencies. This can be expanded to form a multi-resolution approach through successive decompositions of the approximate coefficients. These correspond to the low frequency output signal $X[2k+1]$. If the coefficient at different levels correspond to orthonormal wavelet functions then a controller can manipulate each level individually. This is an important consideration when designing practical wavelet filter-banks.

Consider a twin channel analysis filter-bank with decomposition filters $h_0[n]$ and $h_1[n]$ and reconstruction filters $g_0[n]$ and $g_1[n]$, where $h_0[n] = g_0[-n]$ and $h_1[n] = g_1[-n]$. In the case of the Haar wavelet, h_0 and h_1 have an impulse responses specified by equation (4.7). However, h_0 and h_1 can be defined from any wavelet. Defining h_0, h_1, g_0 and g_1 to be equal to the impulse response of any wavelet then the output signals from the convolution of $x[n]$ with the decomposition filters at $2k$ intervals will be $X^{(1)}[2k]$ and $X^{(1)}[2k+1]$, where $X^{(1)}[2k]$ corresponds to the wavelet coefficient and $X^{(1)}[2k+1]$ forms a residual signal. $X^{(1)}[2k+1]$ can be decomposed again to form the output signals $X^{(2)}[4k]$ and $X^{(2)}[4k+1]$. The superscript, j, indicates the wavelet decomposition level, or octave index. This process can be repeated to give output signals of the form $X^{(j)}[2^j k]$ and $X^{(j)}[2^j k+1]$. The frequency octaves identified by the single level decomposition and the multi-level filterbanks as shown in figure 4.2. Schematic diagrams showing the one dimensional decomposition and reconstruction filterbanks are presented in figure 4.3.

This process is easier to see in reverse. Starting from the reconstruction of the signal $x[n]$ from the wavelet coefficients $X^{(1)}[2k]$ and residual signal $X^{(1)}[2k+1]$ then

$$x[n] = \sum_{k \in Z} X^{(1)}[n-2k] g_1[n-2k] + \sum_{k \in Z} X^{(1)}[2k] g_0[n-2k] \qquad (4.12)$$

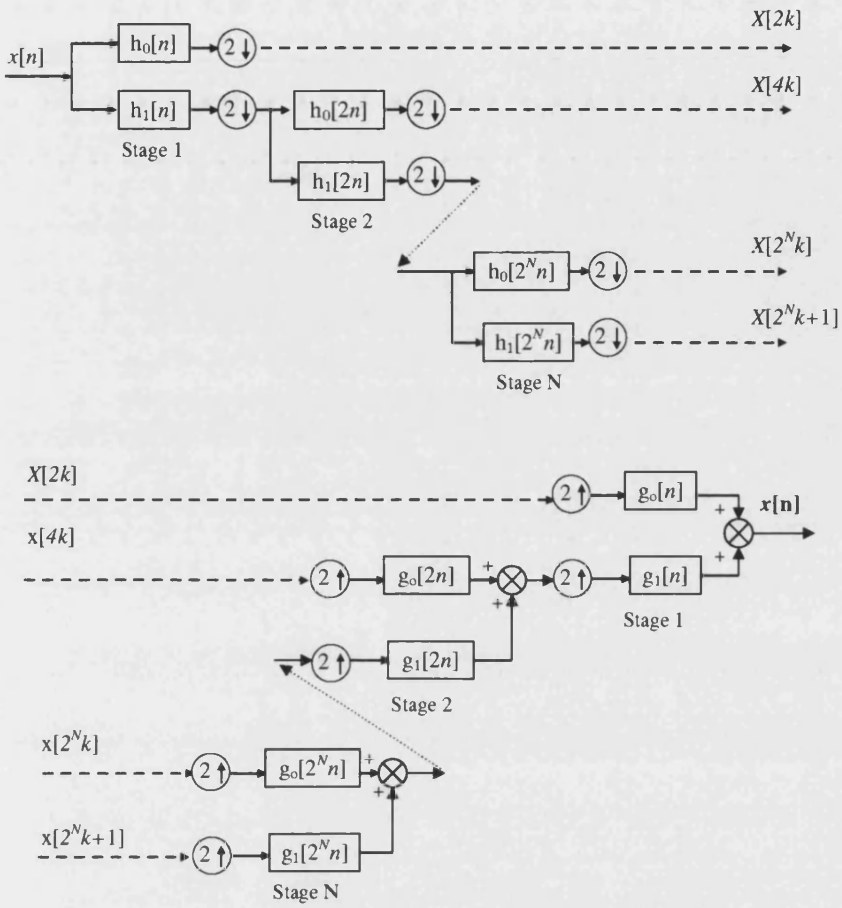

Figure 4.3: Multi-level decomposition (top) and reconstruction (bottom) filterbanks.

where

$$X^{(1)}[2k] = \langle h_0[2^1 k - n], x[n] \rangle , \qquad X^{(1)}[2k+1] = \langle h_1[2^1 k - n], x[n] \rangle \qquad (4.13)$$

are the convolutions of the input signal $x[n]$ with decomposition filters $h_0[n]$ and $h_1[n]$ evaluated at even and odd indexes of $2k$. However, suppose that residual signal $X^{(1)}[2k+1]$ was the construction of two signals $X^{(2)}[2^2 k]$ and $X^{(2)}[2^2 k+1]$. Then the original signal $x[n]$ can be expressed as the combination of the three signals

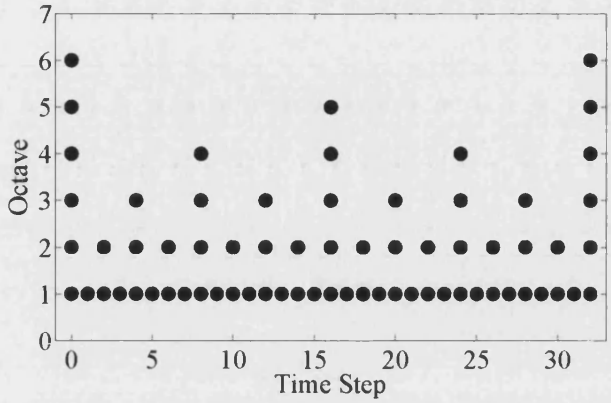

Figure 4.4: Dyadic sampling showing samples at different octaves.

$X^{(1)}[2k]$, $X^{(2)}[2^2k]$ and $X^{(2)}[2^2k+1]$ using

$$\begin{aligned} x[n] = &\sum_{k\in Z} X^{(1)}[n-2k]g_1[n-2k] \\ &+ \sum_{k\in Z} X^{(2)}[n-2^2k]g_1[n-2^2k] \\ &+ \sum_{k\in Z}^{(2)}[2^2k]g_0[n-2^2k] \end{aligned} \tag{4.14}$$

This can be expanded to cover J octaves by

$$x[n] = \sum_{j=1}^{J}\sum_{k\in Z} X^{(j)}[n-2^jk]g_1[n-2^jk] + \sum_{k\in Z} X^{(j)}[2^jk]g_0[n-2^jk] \tag{4.15}$$

The double summation term corresponds to the J different wavelet coefficient levels and the single summation corresponds to the residual signal. The sample time at each individual subband j is scaled by 2^j for each octave. This arises from the down-sampling by 2 at each level of decomposition. This is called Dyadic sampling. Figure 4.4 shows how the sampling varies with each level of decomposition. This forms the basis for wavelet filter bank. For completeness general properties of this approach are now discussed.

Orthogonality

For a two channel orthogonal filter-bank,

$$\langle g_u[n-2k], g_v[n-2l] \rangle = \delta[u-v]\delta[k-l] \tag{4.16}$$

Therefore discrete time wavelets are orthogonal.

Shift

In general multi-rate systems are not shift-invariant, however, twin channel filter-banks down-sampled by 2 are shift-invariant with respect to even shifts only. Therefore a J octave discrete time wavelet coefficient series will be time invariant for all shifts equal to multiples of 2^J. In a discrete time wavelet coefficient series expanded over J-octaves the input signal, $x[n]$, is transformed into $X_j[2k+1]$. Therefore after a shift of $m2^J$

$$x[n-m2^J] = X_j[2(k-m2^{J-j})+1] \tag{4.17}$$

The output signal can be defined as:

$$y[n] = x[n-m2^J] \tag{4.18}$$

which has the transform:

$$Y_j[2^j k+1] = \langle h_1[2^j k-n], x[n-m2^j] \rangle \tag{4.19}$$

Defining n to be the time shifted position of the signal where $n = n' + m2^J$, where m is an integer value, then

$$Y_j[2^j k+1] = \langle h_1[2^j k-n'+2m^J], x[n'] \rangle \tag{4.20}$$

which is equivalent to

$$Y_j[2k+1] = X_j[2(k-m2^{J-j})+1] \tag{4.21}$$

Therefore the discrete time wavelet coefficient series expanded over J octaves is time invariant when shifted by $m2^J$ samples. This can be seen in figure 4.4 where the image shifted by $m2^J$ is identical to the original image.

4.2.4 Polyphase Signal Processing

The previous sections show that it is possible to separate a signal into a detail signal, corresponding to wavelet coefficients, and an approximate signal using filters and down-sampling. Multiple wavelet coefficients can be identified by successively filtering and down-sampling the approximate signal. The output signal from such

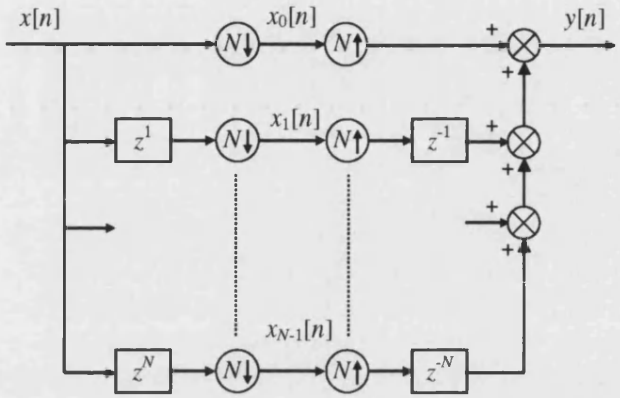

Figure 4.5: N^{th} order polyphase filterbank with decomposition and reconstruction filters.

a filter-bank will therefore contain multiple coefficients each with different sample times.

For a time in-variant system, if an input $x[n]$ produces an output $y[n]$ then the input $x[n+m]$ will produce the output $y[n+m]$. In a time varying system this is not true. However, if there is a periodicity within the time varying system, i.e. it is periodically time variant, an input $x[n]$ produces an output $y[n]$ then an input $x[n+Nm]$ will produce an output $y[n+Nm]$ where N represents the period of the system.

A downsampler is a periodically time-varying system where the input and output have different time scales. Then the input $x[n]$ produces $y[n]$ and the input $x[n+Nm]$ has the output $y[n+m]$. N represents the level of downsampling, i.e. if $N=2$ then every other element is kept.

This provides an elegant method by which a time-varying signal can be transformed and mapped into N sequences each being a downsampled and phase shifted version of the input signal. Such a transform is called a *polyphase transform*. The simplest case is when $N=2$, where the signal is subdivided into odd and even sample indices. This is of most importance when considering downsampling and upsampling by two. The size of N is unlimited such that a size N polyphase transform of a signal , $x[n]$, can be represented as vector, $\mathbf{X}[n]$, containing all the subsequences, $x_i[n]$, of the form

$$\mathbf{X}[n] = [x_0[n]\ x_1[n]\ \ldots\ x_{N-1}[n]]^T \tag{4.22}$$

where the downsampled input signal is

$$x_i[n] = x[nN + i] \tag{4.23}$$

These are referred to as the signal polyphase components. Total signal recovery is simply obtained by interleaving the different subsequences. In the Z-transform domain, $X(z)$ can be written as the summation of shifted and upsampled polyphase components:

$$X(z) = \sum_{i=0}^{N-1} z^i X_i(z^n) \tag{4.24}$$

where

$$X_i(z) = \sum_{i=-\infty}^{\infty} x[nN + 1]z^{-n} \tag{4.25}$$

The forward shift requires that the system is non-causal. To make the system causal and therefore of any use for on-line digital signal analysis, a delay operation must be performed. Therefore, for a causal system, a delay of $N - 1$ samples is required between the forward and inverse polyphase transform. Causality can therefore achieved by multiplying the non-causal forward polyphase transform by z^{-N+1}. Let us now consider the output of filtering with H followed by downsampling in terms of the polyphase components. This can be simplified if we define the polyphase decomposition of the filter to have the reverse phase of the one used for the signal:

$$H(z) = \sum_{i=0}^{N-1} z^i H_i(z^n) \tag{4.26}$$

with

$$H_i(z) = \sum_{i=-\infty}^{\infty} h[nN + 1]z^{-n} \tag{4.27}$$

Therefore the product of $H(z)X(z)$ after downsampling by N is:

$$Y(z) = \sum_{i=0}^{N-1} H_i(z)X_i(z) \tag{4.28}$$

It is therefore possible to separate a signal into N polyphase component signals of size $1/N$ of the original signal and to reconstruct the polyphase components into the original signal. Causality is achieved using a delay of $N - 1$. Figure 4.5 shows an N^{th} order polyphase filterbank with decomposition and reconstruction filters.

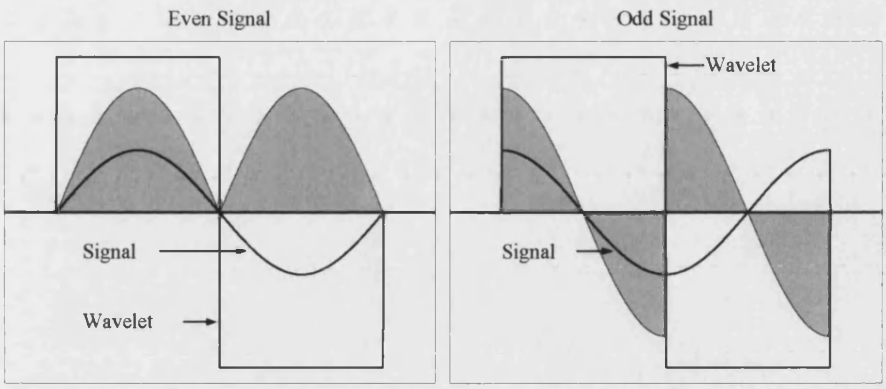

Figure 4.6: Odd and even phase signals and wavelet coefficient evaluation. The sum of the area indicates the wavelet coefficient magnitude. The even wavelet function gives a finite magnitude for the wavelet coefficient whereas the odd wavelet function has zero magnitude.

4.3 Practical Implementation of Wavelet Filterbanks and Signal Phase

Filterbanks have been shown to provide a digital signal processing method of identifying the wavelet coefficients present in measured data. The one dimensional wavelet transform filterbank architecture is shown in figure 4.3 for both decomposition and reconstruction arrangements. In the case of Fourier analysis there exist odd and even basis functions, *sine* and *cosine*. This overcomes problems arising when a signal is 90^0 out of phase with the basis set. Wavelet analysis in the continuous domain addresses phase through the evaluation of the signal through a continuum of translations, and therefore considers all phase angles. In digital signal processing the wavelet transform is evaluated at fixed translations. This is a problem when there is a 90^0 phase difference between signal and wavelet. This results in a zero wavelet coefficient value. Figure 4.6 shows two signals with a 90^0 phase difference between them. In the even case the signal and wavelet have identical phases. In the odd case the wavelet and signal are 90^0 out of phase and the wavelet coefficient will be zero. A digital signal processing approach needs to take into account the odd and even signal components with appropriate odd and even wavelets. This can be achieved by using odd and even filter channels with odd and even wavelets, each with a 90^0 phase shift achieved using a quarter period delay on the input channel.

4.4 Mother Wavelet Discussion

Wavelet analysis is centered on a basis set expansion of a signal with an appropriate wavelet function. The only requirement of the wavelet function is that it has zero mean.

It is noted that within this condition both *sine* and *cosine* are wavelets. However, as already discussed, *sine* and *cosine* have zero resolution in time. In order to achieve finite time dispersion, windowing techniques can be used. There are many different windowing methods. A common choice is to multiply (*sine*, *cosine*) by a Gaussian function. A Gaussian windowed *sine* wave was proposed by Gabor in 1946 and forms one of the earliest wavelets [70]. Another wavelet based on the Gaussian function is the Mexican-Hat wavelet, which is derived from the second derivative of a Gaussian function.

It is advantageous from a control design point of view to consider orthogonal wavelets. This means that $\psi(t)$ is orthogonal to all its dilations and translations. For control, this allows the wavelet coefficients to be manipulated individually in order to evaluate a control force.

In 1988, Daubechies [71] proposed what has become one of the most popular family of wavelets. In the literature on filters, the Daubechies wavelets are often refereed to as *maxflat* filters. Wavelets 1, 2, 4 and 8 are shown in figure 4.7. Both scaling and wavelet functions are presented. These correspond to the impulse response of the high and low pass filters corresponding to the choice of wavelet. The construction of these filters is based on two key properties. Firstly, the filters, or wavelets, are orthogonal. Secondly, the frequency response of the filters must have maximum flatness, corresponding to the rate of change of the frequency response equalling zero, at $\omega = 0$ and $\omega = \pi$. This is seen in figure 4.8 showing the frequency content of Daubechies wavelets 1, 2, 10 and 40. It is often desirable that the filter should have maximum flatness in as many derivatives as possible, although this is not a rigid design criteria.

Daubechies filters are constructed from half of the $p-1$ zeros inside the unit circle in order to retain minimum phase, where p indicates the order. The coefficients of the filter are then evaluated using spectral factorization, a full derivation can be found in [69]. However, other choices lead to wavelets with increased symmetry, [69]. These wavelets are called Symlets, figure 4.9 shows Symlet wavelets 1, 2, 4 and 8. These filters are finite impulse responses with $2p$ coefficients (e.g. the Daubechies 1 filter has two coefficients). As the size of the filter, p, increases the filters become increasingly regular, this corresponds to the wavelets becoming smoother [68].

The Daubechies wavelet with the least coefficients is also known as the Haar wavelet and has length two. Although part of the Daubechies family, the Haar wavelet also occurs as part of other wavelet families. The Haar wavelet is also the only

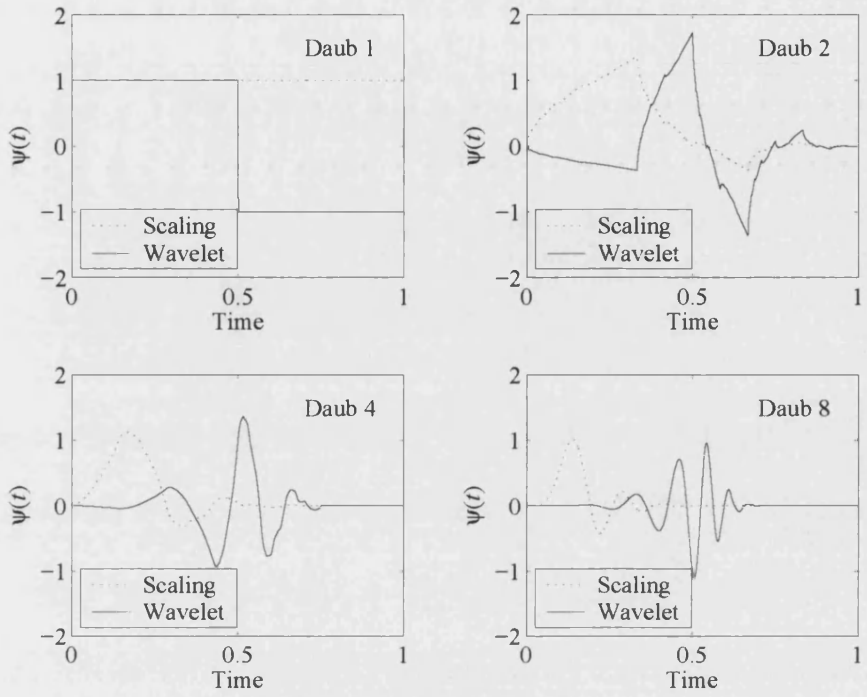

Figure 4.7: Daubechies wavelets.

solution providing a wavelet of length two. It is therefore the wavelet with optimum resolution in time.

Coifman wavelets, also know as Coiflets, are orthogonal wavelets for which the wavelet and scaling functions have several vanishing moments [72]. Figure 4.10 shows the first four Coifman wavelets. Fourier transforms of the Coifman wavelet at different orders are are shown in figure 4.11. The derivation of Coifman wavelets is similar to that of Daubechies wavelets, however, there are several differences. Unlike Daubechies wavelets which are inherently orthogonal, Coiflets are not. In order to ensure orthogonality conditions are applied to solution of the wavelet equation. There is also no need for spectral factorization. A full derivation of Coifmans wavelets can be found in [72].

Taking the Fourier transform of Daubechies wavelets, as order of the wavelet increases the frequency content converges toward a box, (figure 4.8), i.e. the frequency content is zero apart from a region where it is a finite value. Newland [33] starts with the assumption that the frequency content of a wavelet is zero except for a frequency band where it is a constant. The wavelet is then evaluated from the inverse Fourier transform. The real and imaginary parts of the solution give odd and even

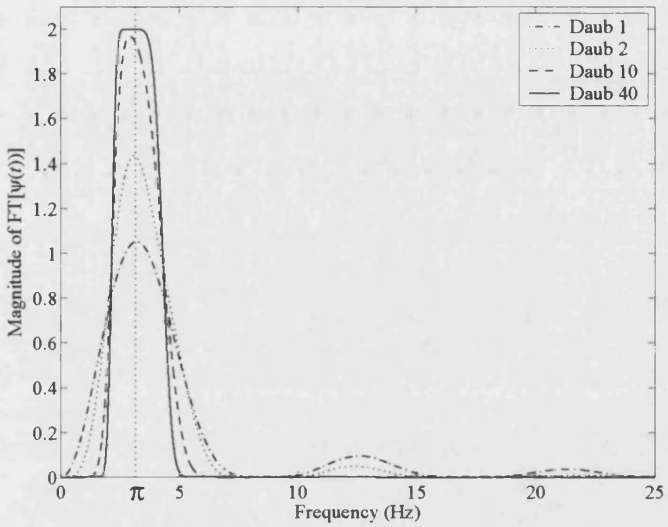

Figure 4.8: Fourier transform of Daubechies wavelets of order 1, 2, 10 and 40.

wavelets, respectively. These correspond to the odd and even parts of the Fourier series expansion. These wavelets are called harmonic wavelets, which can be shown to be orthogonal [33]. From the construction of harmonic wavelets it is inherent that they have excellent resolution in frequency. However, they have finite magnitude throughout time. The filterbank wavelet coefficient evaluation time will therefore be infinite.

The wavelets considered thus far are orthogonal. Greater flexibility in the construction of a wavelet basis can be achieved by considering non-orthogonal wavelets. However, orthogonality may be desirable when designing a control strategy. This can be addressed by considering bi-orthogonal wavelet basis. In depth discussions concerning bi-orthogonal wavelets and their derivations can be found in [68,69,72]. These include bi-orthogonal Daubechies wavelets and spline wavelets such as the Battle-Lemarié type.

4.5 Wavelet Uncertainty?

Important factors in the choice of wavelet include its resolution in time and frequency. This leads to Heisenberg's uncertainty principle. Consideration of the ratio between resolutions has been proposed by Monro [73] leading to a balanced uncertainty.

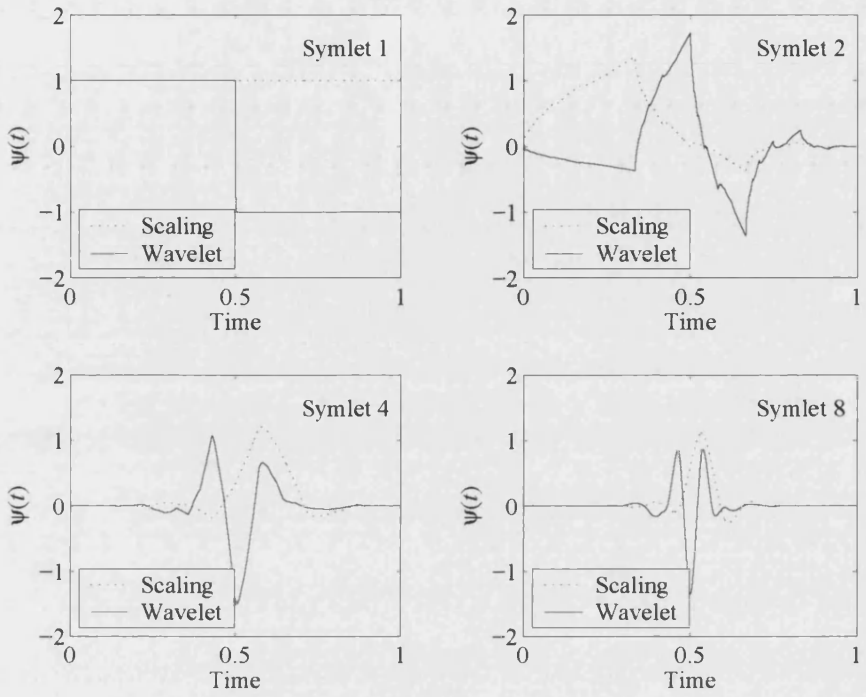

Figure 4.9: Symlet wavelets.

4.5.1 Heisenberg uncertainty

The lower limit on the time-frequency resolution that can be obtained is determined by Heisenberg's uncertainty principle which states [70]:

$$\Delta\omega\Delta t \geq 1/2 \tag{4.29}$$

where $\Delta\omega$ and Δt represent the uncertainty in frequency and time (or bandwidth and time–dispersion), respectively. Lower uncertainties correspond to better resolution. Therefore the lower the uncertainty the better the resolving power of the wavelet. The only wavelet to achieve the lower limit of uncertainty is the infinite time Gabor wavelet [70]. The frequency resolution $\Delta\omega$ of $f(t)$ is defined from [72]

$$(\Delta\omega)^2 = \int_{-\infty}^{\infty} \omega^2 |F(\omega)|^2 d\omega \tag{4.30}$$

and the time resolution Δt from

$$(\Delta t)^2 = \int_{-\infty}^{\infty} t^2 |f(t)|^2 dt \tag{4.31}$$

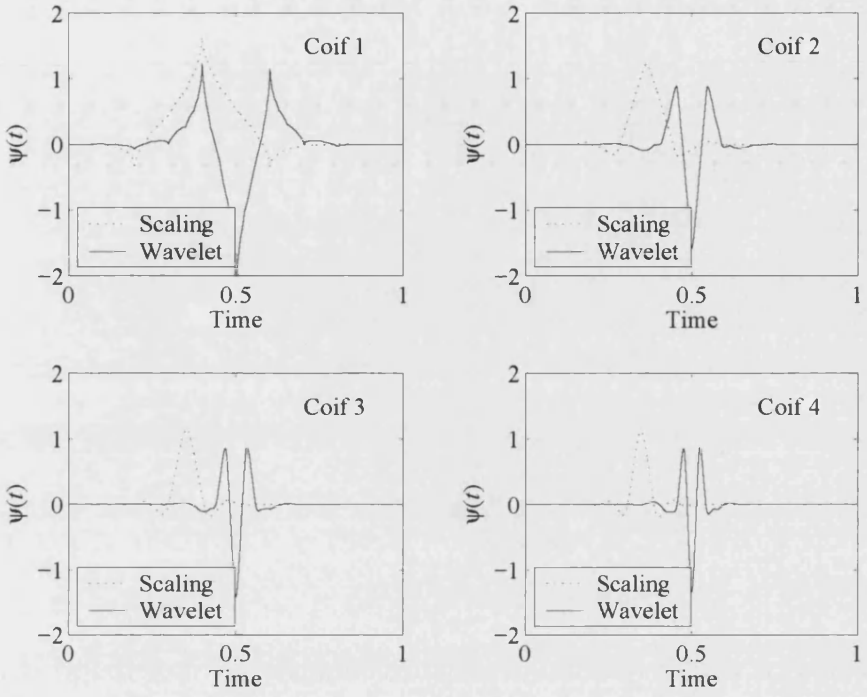

Figure 4.10: Coifman wavelets.

The time dispersion and bandwidth can be evaluated directly from the coefficients of a finite impulse response filter [68]. The bandwidth takes the form [72]

$$(\Delta\omega)^2 = \frac{\pi^2}{3} + 4\sum_{n=0}^{L-2}\sum_{m=n+1}^{L-1}\frac{(-1)^{m-n}}{P(m-n)^2}h_m h_n \tag{4.32}$$

where:

$$P = \sum_{n=0}^{L-2} h_n^2 \tag{4.33}$$

If the filter is is derived from an orthogonal wavelet then $P = 1$. The time-dispersion can be evaluated from

$$(\Delta t)^2 = \sum_{n=0}^{L-1}(n-\alpha)^2 h_n^2 \tag{4.34}$$

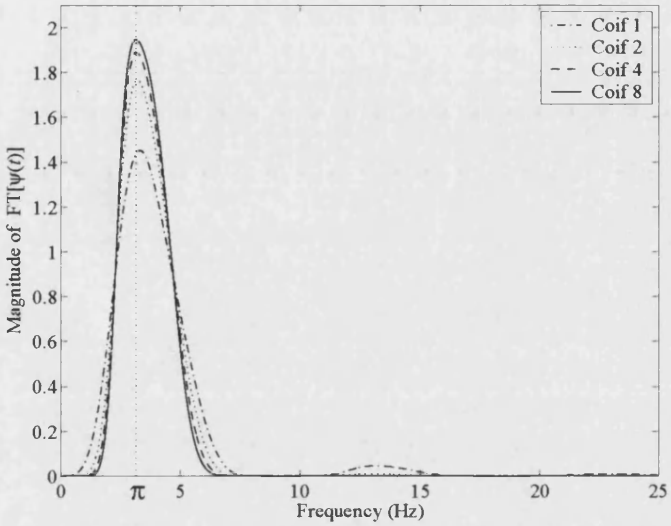

Figure 4.11: Fourier transform of Coifman wavelets of order 1, 2, 3 and 4.

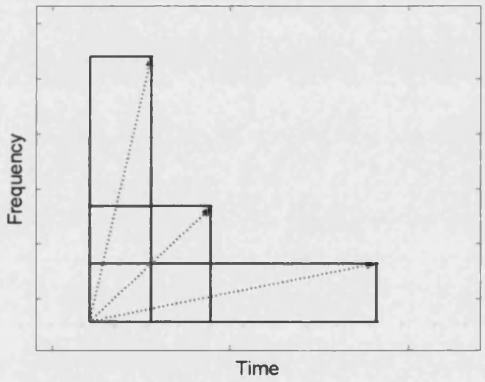

Figure 4.12: Wavelets with equal uncertainty but with different time-dispersions and bandwidths.

where

$$\alpha = \frac{\sum_{n=0}^{L-1} n h_n}{\sum_{n=0}^{L-1} h_n} \tag{4.35}$$

Table 4.1: Wavelet uncertainties, $k = 1$.

Wavelet	$\Delta\omega$	Δt	$\Delta\omega\Delta t$	$M(1)$
Daubechies 1 (Haar)	1.136	0.5000	0.5677	1.540
Daubechies 2	1.033	0.6124	0.6328	1.443
Daubechies 4	0.9731	0.9002	0.8759	1.757
Daubechies 8	0.9407	1.436	1.351	2.947
Daubechies 16	0.9240	2.420	2.236	6.712
Symlets 2	1.033	0.6124	0.6328	1.443
Symlets 4	0.9731	0.6669	0.6489	1.392
Symlets 8	0.9407	0.8550	0.8043	1.616
Coifman 1	1.030	0.5540	0.5703	1.367
Coifman 2	0.9696	0.6527	0.6329	1.366
Coifman 4	0.9383	0.7783	0.7302	1.486
Discrete Meyer	0.9146	1.107	1.013	2.063

4.5.2 Balanced Uncertainty

The product of the time-dispersion and bandwidth, $\Delta\omega\Delta t$, gives a measure of the resolving power of the wavelet. However, it provides no information to as the relative uncertainties. Figure 4.12 shows the uncertainty for 3 different filters. The magnitudes of the uncertainties are identical, however, the time-dispersion and bandwidth are different in each case.

Monro [73] proposes a method of characterizing the resolution of a wavelet filter from the size of the ratio between time-dispersion and bandwidth. A balanced uncertainty favouring a minimum ratio between time-dispersion and bandwidth $M(k)$ is defined as

$$M(k) = (\Delta\omega)^2 + k(\Delta t)^2 \tag{4.36}$$

k is introduced to assign relative importance to the time and frequency resolution.

4.6 The Best Wavelet?

Table 4.1 shows the Heisenberg and balanced uncertainties for common wavelets. In all cases, it can be seen that as the order of the wavelet increases, its resolution in

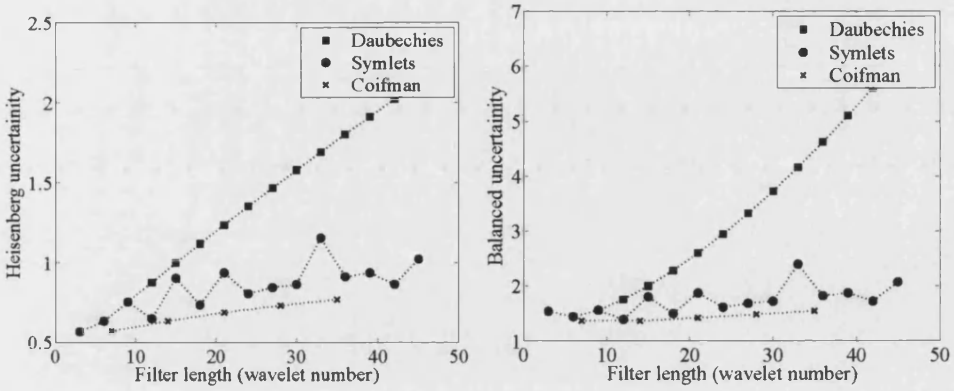

Figure 4.13: Heisenberg and balanced uncertainty ($k = 1$) for the Daubechies, Symlets and Coifman wavelet families for different length filters

frequency improves. However, the resolution in time is reduced. The total resolution of the wavelet, given by the Heisenberg uncertainty, is also seen to increase with wavelet order. Consideration of the balanced uncertainties indicates that the ratio between time-dispersion and bandwidth, $M(k = 1)$, for low order wavelets, $N \leq 10$, remain similar. However, as the order increases, $N > 10$, then the balanced uncertainty increases. Figure 4.13 shows the Heisenberg and balanced uncertainties against wavelet order. The time taken to evaluate wavelet coefficients using filterbanks is also dependent on the sample time and the wavelet length, as dictated by the order number. The objective of this research is to identify and control fault conditions in rotor/magnetic bearings during the transient response. Time dispersion and the delay associated with filterbank evaluation is therefore an important consideration. It is therefore reasonable to favour low order wavelets/filters.

4.7 Closure

This chapter considers wavelet analysis starting with the wavelet transform. An overview of discrete time wavelet analysis using filterbanks is provided along with digital signal processing techniques relevant to the polyphase signals involved. This provides a mechanism that allows wavelet analysis of a digital signal to be performed on-line in real-time.

The different families of wavelet including Daubechies, Symlets, Coifman and others are discussed. Consideration is made to the possible performance benefits of different wavelets when considering transient rotor vibratory responses. The resolving power of the wavelets has also been considered.

Chapter 5

FAULT IDENTIFICATION USING DISCRETE TIME WAVELET COEFFICIENTS

5.1 Fault Disturbance Classification

In order to maintain safe operation of a rotor/magnetic bearing system it is important to identify the onset time and disturbance type in order to evaluate the correct control forces. Correct identification of the disturbance from the response requires an understanding of both the system and the disturbance acting upon it.

5.1.1 Direct Synchronous Forcing

Direct synchronous forcing within the system arising from unbalance may be present at a residual level or it may occur suddenly. The most dramatic case is a step change. This can be represented in fixed or synchronous rotating reference frames as

$$f_x(t) + if_y(t) = me\Omega^2 e^{i\Omega t} H(t-\tau) \tag{5.1}$$

$$f_u(t) + if_v(t) = me\Omega^2 H(t-\tau) \tag{5.2}$$

where $H(t)$ is the Heaviside step function, m is the unbalance mass, e is the eccentricity and Ω is angular frequency of rotation. f_x and f_y represent the forces in the directions of the x and y axes respectively. The forces f_u and f_v represent the components in the directions of the u and v axes, where the u and v are orthogonal in a rotational reference frame with a synchronous angular frequency. A rotating

reference frame is a natural choice for the analysis of direct synchronous forcing since the force can be represented as a constant rather than an oscillatory vector. The response of the rotor, $\mathbf{q}(t)$, can be described in both reference frames by:

$$\mathbf{q}(t) = \begin{cases} 0 & t < \tau \\ \mathbf{q}_{trans}(t) + \mathbf{q}_{ss}(t) & t \geq \tau \end{cases} \tag{5.3}$$

where $\mathbf{q}_{trans}(t)$ and $\mathbf{q}_{ss}(t)$ represent the transient and the steady state responses, respectively. In the case of a rotating reference frame the steady state response of the system is a constant for a circular orbit. From equation (5.3) it is possible to take the continuous wavelet transform of rotor displacement, $\mathbf{q}(t)$, in the u and v directions at a specific element node. Defining some time T_{ss} to be the time at which the system reaches a nominal steady state where the transient response becomes negligible, then for a single component

$$c(a,b) = \begin{cases} 0 & b < \tau - a \\ \int_{-\infty}^{\infty} q_{trans}(t)\psi(\frac{t-b}{a})dt & \tau - a \leq b < T_{ss} + \tau \\ 0 & T_{ss} + \tau < b \end{cases} \tag{5.4}$$

Therefore in a rotating reference frame, since a wavelet has zero mean, the wavelet coefficients only have non-zero values in the region of transient response.

5.1.2 Auxiliary Bearing Contact

Auxiliary bearing contact with the rotor may occur from a wide variety of fault conditions. In order to identify contact from a sensor signal it is important to understand the system dynamics. The force exerted by the auxiliary bearing on the rotor, during a short duration contact, normal and tangential to contact may be written as

$$f_x(t) + if_y(t) = [-f_c - i\mu f_c]P(t)e^{i\theta} \tag{5.5}$$

where μ is the friction coefficient of contact, θ is a phase angle and f_c is the radial force acting on the rotor from the auxiliary bearing. $P(t)$ is a parameter representing the contact period and is zero when no contact occurs. This is based on a Hertzian stress formulation.

The rotor response to the short duration contact in both the fixed and rotating reference frames will take the form of equation (5.3). Therefore, a wavelet analysis of the rotor displacement will contain non-zero wavelet coefficients during the transient response only, shown in equation (5.4). However, unlike sudden unbalance the

wavelet coefficients will be localized in the rotating reference frame.

5.2 Simulated Fault Conditions

The system is considered as described in chapter 2. Simulation of the rotor response to the different fault conditions was undertaken at a speed coincident with the natural frequency of the second bending mode (67Hz). The wavelet decomposition filter banks were configured with a wavelet sampling frequency of 0.46ms, matching the synchronous frequency at the 5^{th} octave. The filter banks were set with a frequency range of eight octaves. This provides information of frequencies both higher and lower than the running speed of the rotor. A rotor unbalance response was obtained by applying a synchronous disturbance force to the right hand end of the rotor equivalent to 300N amplitude. Wavelet analysis was undertaken on the rotor displacement at sensor 1, in order to demonstrate non-local fault detection. The octaves have been indexed such that highest frequency is unity.

The simulated rotor response at a frequency of 67Hz, corresponding to the natural frequency of the second bending mode, is presented in figure 5.1. The component wavelet coefficients are presented in figure 5.2. Figure 5.1 shows the rotor undergoing a transient period before settling into a steady state vibration. This is further seen in figure 5.2(c) at the 5^{th} octave, matching the synchronous frequency. In a rotating reference frame the wavelet coefficients only have non-zero values in the region of the transient response. This is seen in figure 5.3 showing peaks in the coefficients immediately after the onset of direct synchronous forcing. It is clear from figures 5.2 and 5.3 that high and low frequencies are excited by the sudden change in forcing condition on the rotor. This is further seen in figures (5.7-5.12) showing the fixed and rotating wavelet coefficients at 18Hz and 29Hz. These frequencies correspond to the second rigid body and first flexible modes of vibration of the rotor respectively. In a rotating reference frame the wavelet coefficients are present immediately after the disturbance before decaying to zero. In the fixed reference frame the low frequencies are seen to decay while frequencies higher than and including the synchronous frequency remain. The response time of the different octaves to the fault is dependent on the sampling frequency such that the higher octaves and lower frequencies take longer to resolve.

Auxiliary bearing contact was simulated with a steadily orbiting rotor, undergoing direct synchronous forcing that slowly reduced with time. Progressive misalignment of the right end auxiliary bearing (figure 2.1) was imposed until contact occurred. Immediately after contact the bearing was returned to its original location in order to prevent further contacts. Direct synchronous forcing was used to excite the rotor into a steady state orbit so that a comparison can be made between the wavelet coefficients of both faults allowing them to be distinguished. Simulation of the rotor/bearing contact shows the short duration contact assumption to be reasonable with simulation contact time lasting $\sim 1/20^{th}$ of a rotor period.

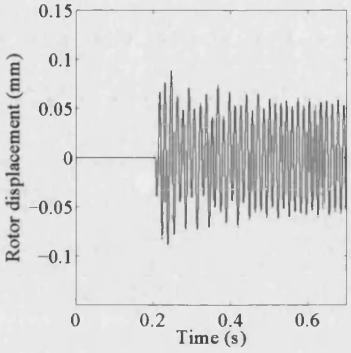

Figure 5.1: Rotor displacement in the fixed frame x direction at sensor 3 due to rotor unbalance at 425 rad/s.

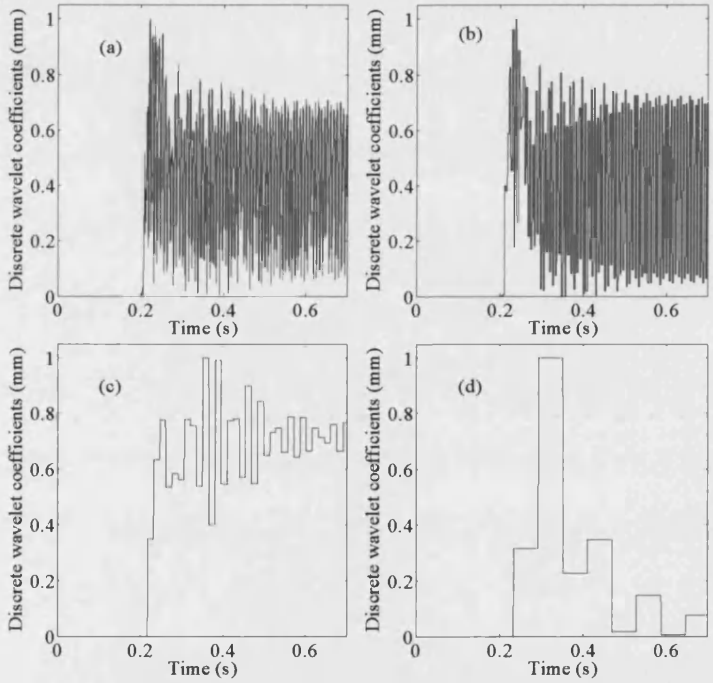

Figure 5.2: (a)-(d) show the absolute normalized discrete time wavelet series of the rotor displacement at the 1^{st}, 3^{rd}, 5^{th} and 7^{th} octaves respectively.

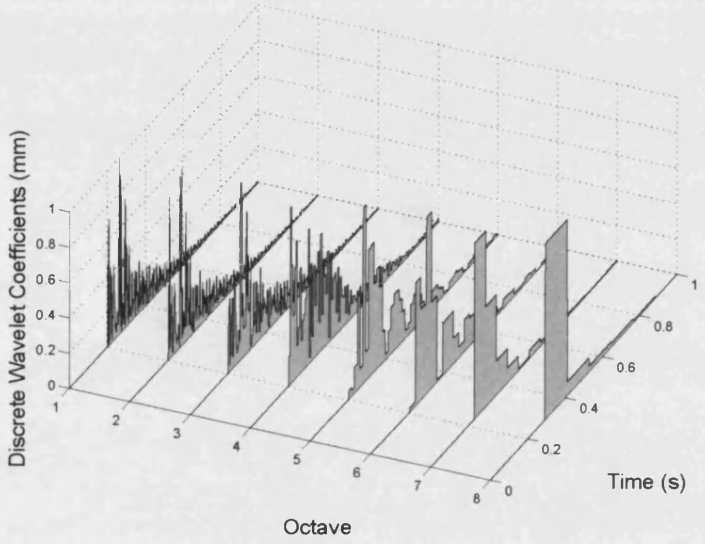

Figure 5.3: Absolute normalized discrete time wavelet series of the rotor displacement (u) in a rotating reference frame in sensor plane (3,4) following a sudden change in unbalance at $0.2s$.

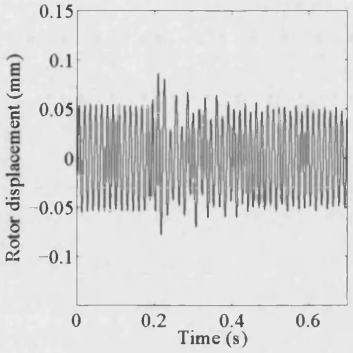

Figure 5.4: Rotor displacement in the fixed frame x direction at sensor 3 due to rotor unbalance and rotor/auxilary bearing contact at 425 rad/s.

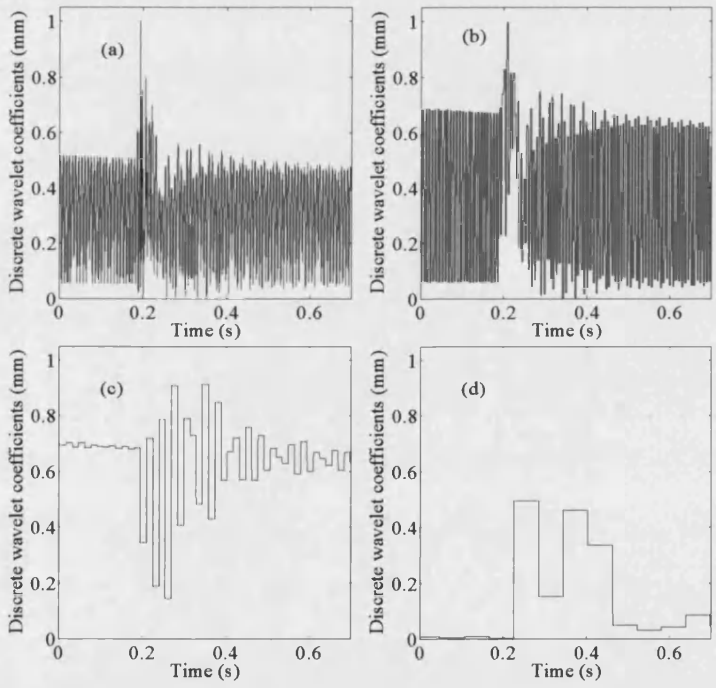

Figure 5.5: (a)-(d) show the absolute normalized discrete time wavelet series of the rotor displacement at the 1^{st}, 3^{rd}, 5^{th} and 7^{th} octaves respectively.

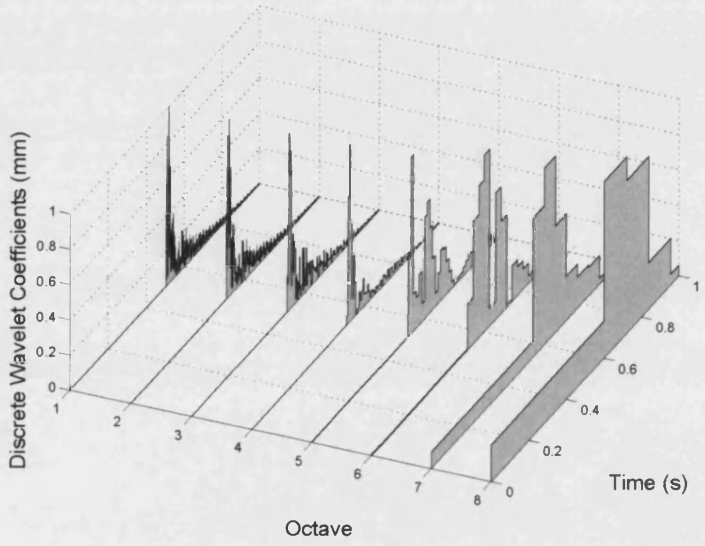

Figure 5.6: Absolute normalized discrete time wavelet series of the rotor displacement (u) in a rotating reference frame in sensor plane (3,4) during rotor unbalance with a rotor/auxiliary bearing contact.

Figure 5.4 shows the rotor vibration, the wavelet coefficients evaluated in a fixed reference frame at the 1^{st}, 3^{rd}, 5^{th} and 7^{th} octaves are presented in figure 5.5. Localized excitation of the wavelet coefficients due to the contact is clearly visible. This is further seen in figure 5.6 showing localized excitation of high and low frequency wavelet coefficients immediately after rotor/bearing contact. However, in a fixed reference frame residual wavelet coefficients associated with the steady state rotor orbit are also present in the wavelet coefficients corresponding to frequencies higher than and including the rotor speed (figure 5.5). This is further seen in figures 5.13-5.18 showing rotor/auxiliary bearing contact at 18Hz and 29Hz corresponding to the second rigid body and first flexible modes of vibration, respectively.

The method of fault identification presented is based around the compact support of the mother wavelet. It is therefore independent of the choice of wavelet used. Figures 5.19-5.26 show the wavelet coefficient responses in the fixed and synchronous rotating reference frames due to mass loss and rotor/auxiliary bearing contact at 67Hz corresponding to Daubechies mother wavelets 2 and 4 respectively. In both cases the onset time and fault type are identifiable. However, in the case of Daubechies 4 the natural frequency of the mother wavelet is longer than for Daubechies 1 (Haar wavelet) or 2. This results in a longer evaluation time when identifying a specific vibratory frequency, which can be considered undesirable when monitoring for a fault condition.

Figures 5.1-5.26 show that the onset time of both sudden unbalance or rotor/bearing contact can be identified. This is based around using wavelets to identify the discontinuities present in the measured rotor response due to fault condition. The localized discontinuities, with multiple frequency components, are shown as spikes in the wavelet coefficients at multiple levels. A thresholding method can then be used to identify the onset of a fault condition. It is also possible to differentiate between fault conditions as well as identify the onset time from a comparison of the wavelet coefficients in fixed and synchronously rotating reference frames. Rotor/bearing contact will result in transient excitation in both reference frames. Sudden rotor unbalance will result in a transient and steady state response in the fixed reference frame. The synchronously rotating reference frame filters out the steady state response leaving only the transients. This allows for the different fault conditions to be identified. Table 5.1 shows how the different responses can be used to identify the fault condition.

Table 5.1: Wavelet coefficient response characteristics due to sudden rotor unbalance and rotor/bearing contact.

Reference Frame		Fixed	
		Transient	Steady state
Synchronous	Transient	Both	Sudden mass loss
	Steady state	Unidentified	Unidentified

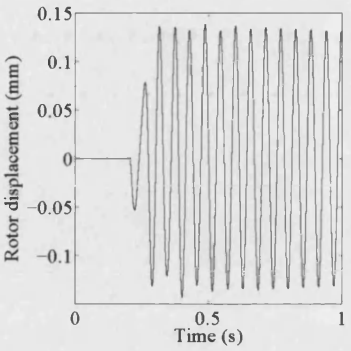

Figure 5.7: Rotor displacement in the fixed frame x direction at sensor 3 due to rotor unbalance at 111 rad/s.

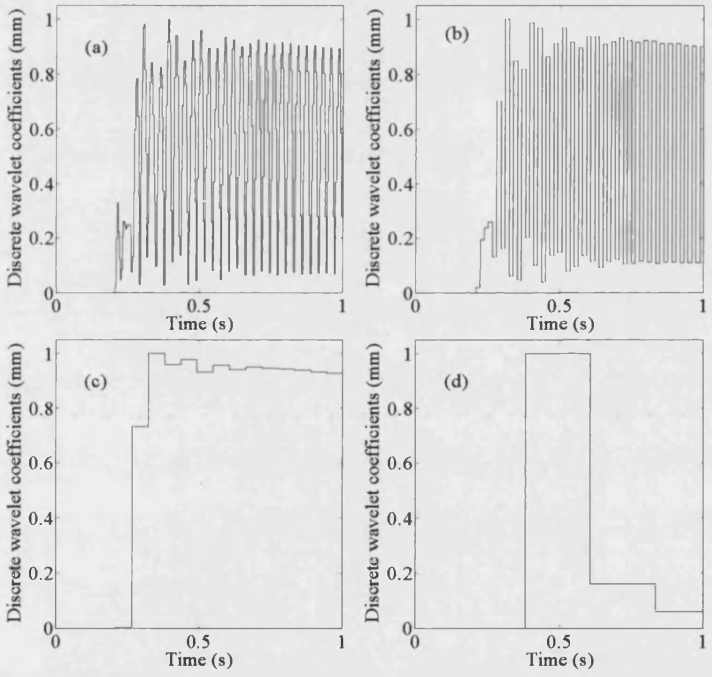

Figure 5.8: (a)-(d) show the absolute normalized discrete time wavelet series of the rotor displacement at the 1^{st}, 3^{rd}, 5^{th} and 7^{th} octaves respectively.

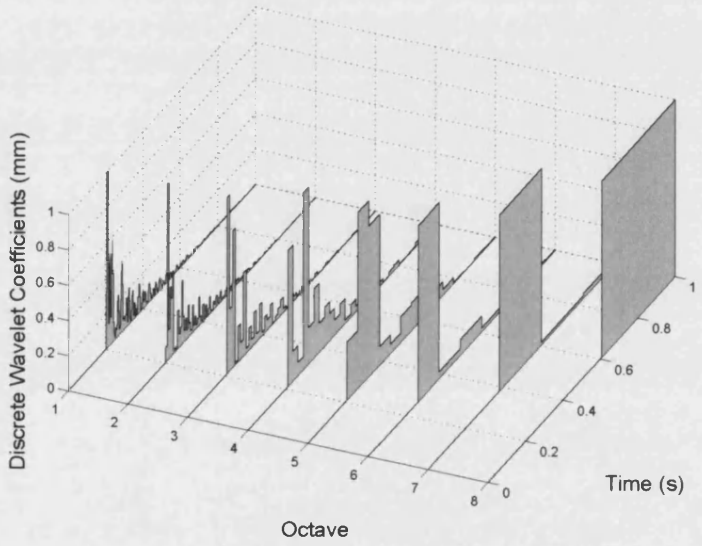

Figure 5.9: Absolute normalized discrete time wavelet series of the rotor displacement (u) in a rotating reference frame in sensor plane (3,4) during rotor unbalance at 111 rad/s.

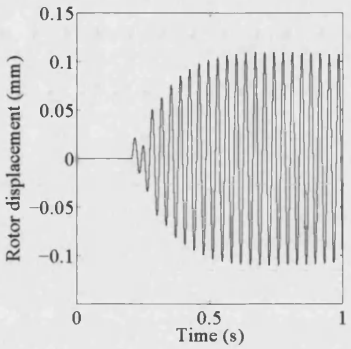

Figure 5.10: Rotor displacement in the fixed frame x direction at sensor 3 due to rotor unbalance at 180 rad/s.

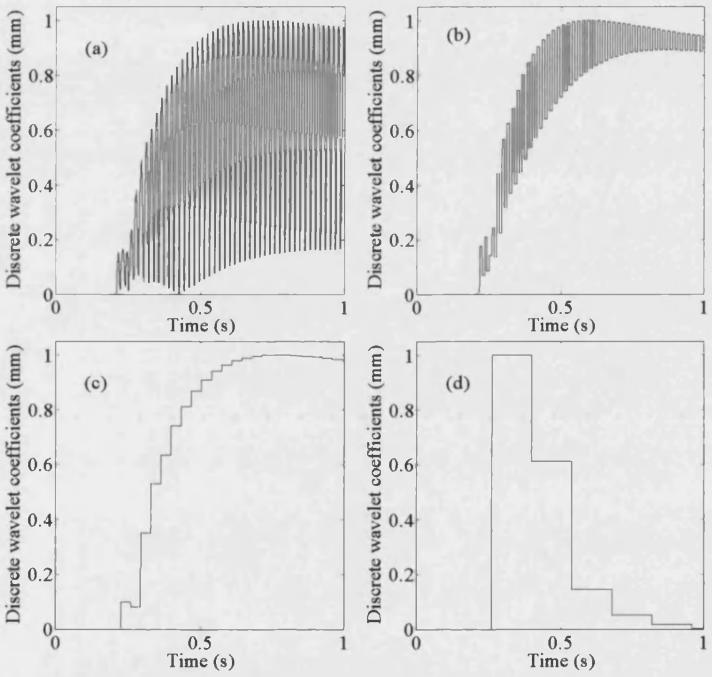

Figure 5.11: (a)-(d) show the absolute normalized discrete time wavelet series of the rotor displacement at the 1^{st}, 3^{rd}, 5^{th} and 7^{th} octaves respectively.

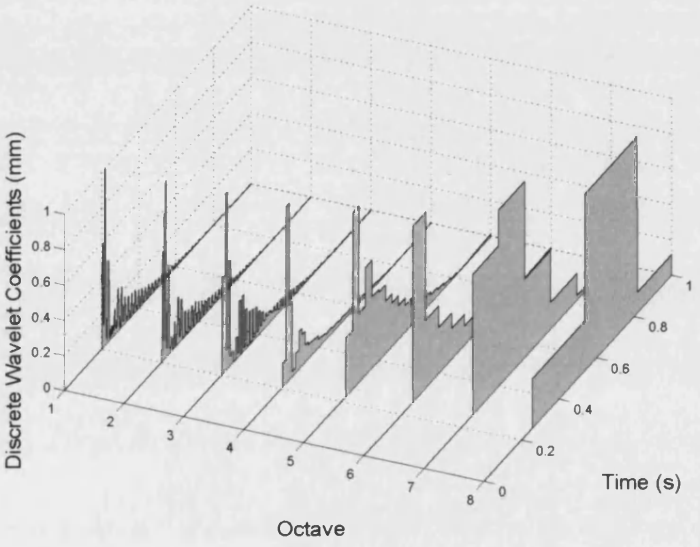

Figure 5.12: Absolute normalized discrete time wavelet series of the rotor displacement (u) in a rotating reference frame in sensor plane (3,4) during rotor unbalance at 180 rad/s.

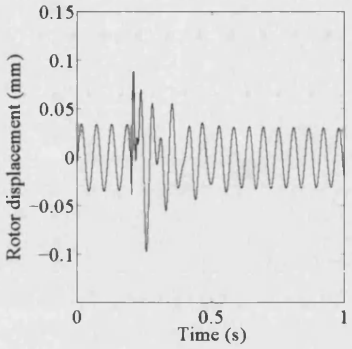

Figure 5.13: Rotor displacement in the fixed frame x direction at sensor 3 due to rotor unbalance and rotor/auxiliary bearing contact at 111 rad/s.

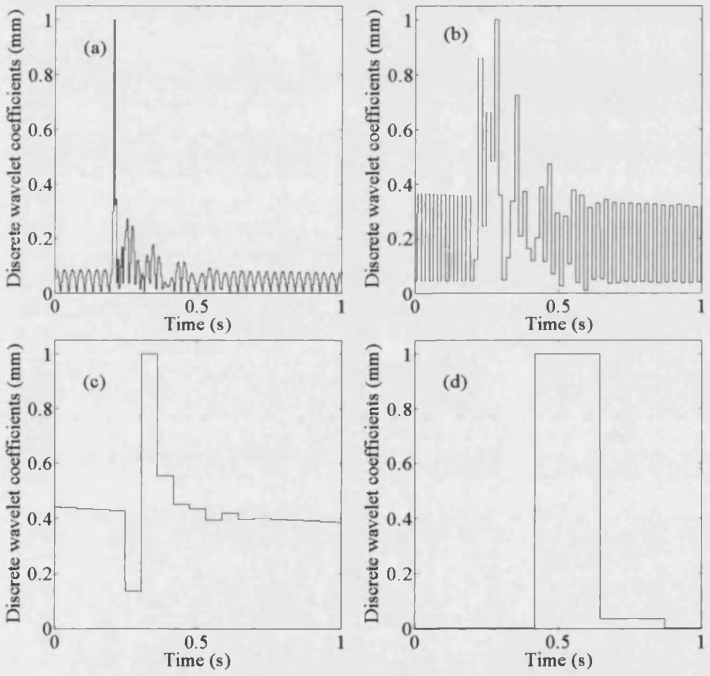

Figure 5.14: (a)-(d) show the absolute normalized discrete time wavelet series of the rotor displacement at the 1^{st}, 3^{rd}, 5^{th} and 7^{th} octaves respectively.

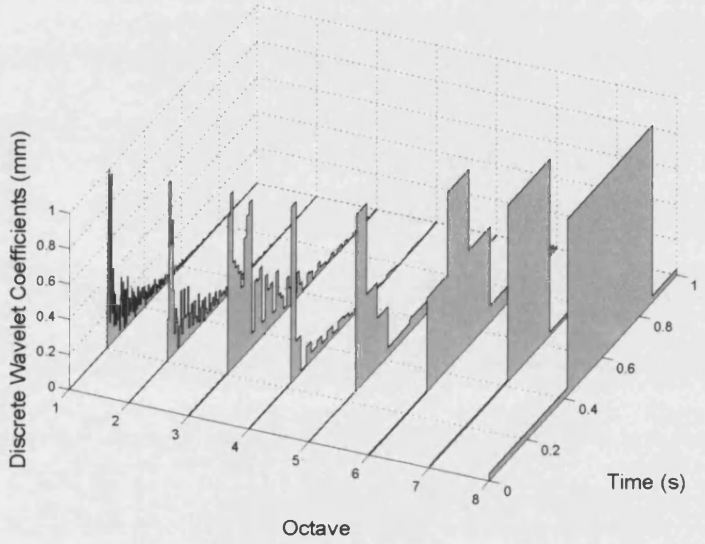

Figure 5.15: Absolute normalized discrete time wavelet series of the rotor displacement (u) in a rotating reference frame in sensor plane (3,4) during rotor unbalance and rotor/auxiliary bearing contact at 111 rad/s.

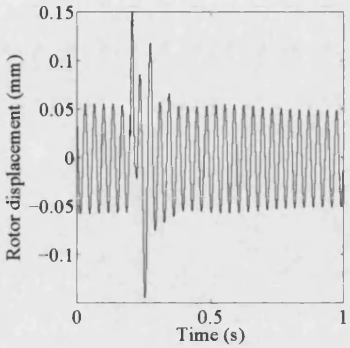

Figure 5.16: Rotor displacement in the fixed frame x direction at sensor 3 due to rotor unbalance and rotor/auxiliary bearing contact at 180 rad/s.

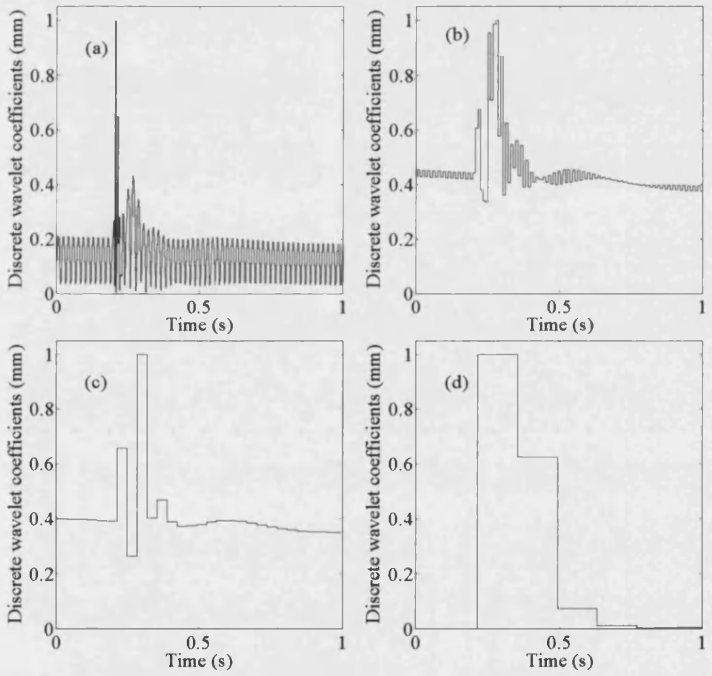

Figure 5.17: (a)-(d) show the absolute normalized discrete time wavelet series of the rotor displacement at the 1^{st}, 3^{rd}, 5^{th} and 7^{th} octaves respectively.

ts

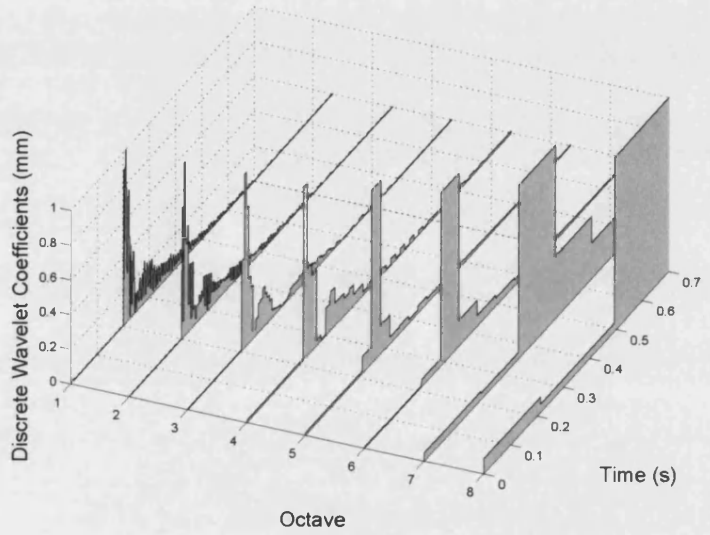

Figure 5.18: Absolute normalized discrete time wavelet series of the rotor displacement (u) in a rotating reference frame in sensor plane (3,4) during rotor unbalance and rotor/auxiliary bearing contact at 180 rad/s.

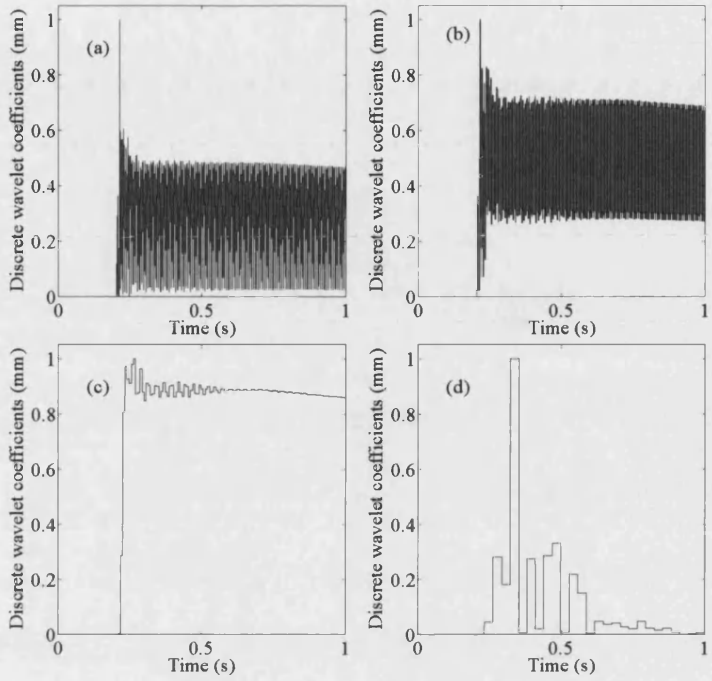

Figure 5.19: Absolute normalized discrete time wavelet series evaluated using Daubechies wavelet 2 in a fixed reference frame due to a sudden change in rotor unbalance at 425 rad/s. The graphs presented correspond to the 1^{st} (a), 3^{rd} (b), 5^{th} (c) and 7^{th} (d) octaves respectively.

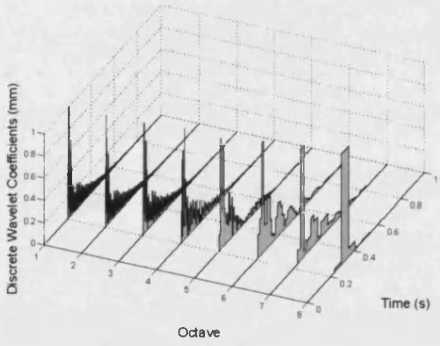

Figure 5.20: Absolute normalized discrete time wavelet series evaluated using Daubechies wavelet 2 in a rotating reference frame due to a sudden change in rotor unbalance at 425 rad/s.

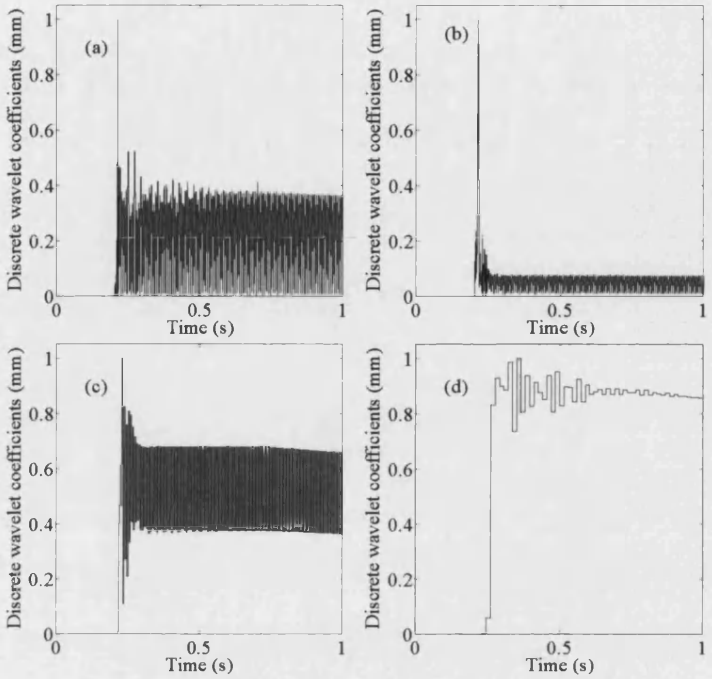

Figure 5.21: Absolute normalized discrete time wavelet series evaluated using Daubechies wavelet 4 in a fixed reference frame due to a sudden change in rotor unbalance at 425 rad/s. The graphs presented correspond to the 1^{st} (a), 3^{rd} (b), 5^{th} (c) and 7^{th} (d) octaves respectively.

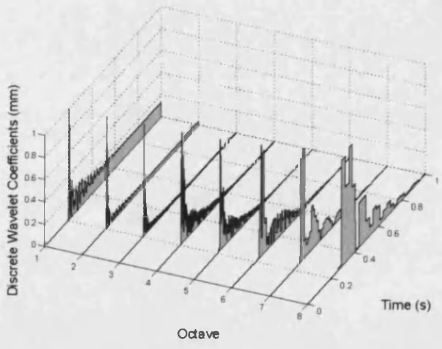

Figure 5.22: Absolute normalized discrete time wavelet series evaluated using Daubechies wavelet 4 in a rotating reference frame due to a sudden change in rotor unbalance at 425 rad/s.

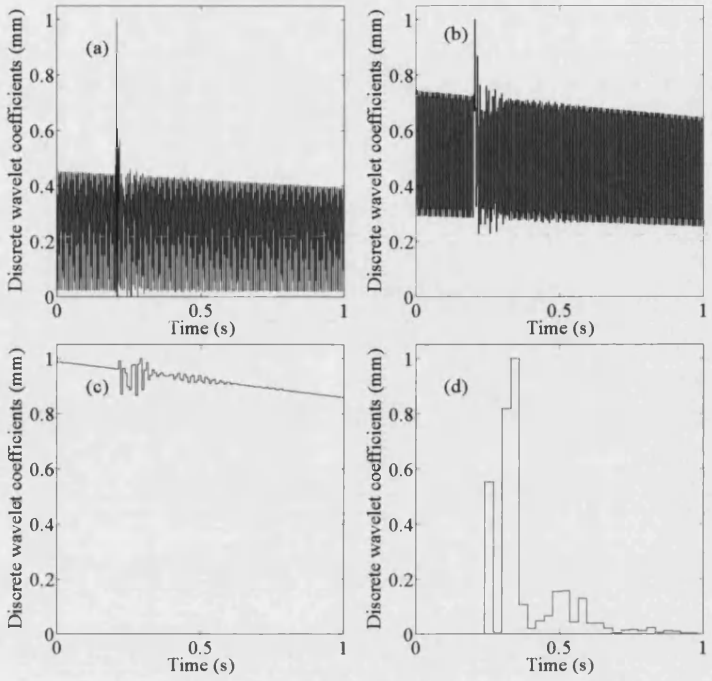

Figure 5.23: Absolute normalized discrete time wavelet series evaluated using Daubechies wavelet 2 in a fixed reference frame due to a rotor unbalance with rotor/auxiliary bearing contact at 425 rad/s. The graphs presented correspond to the 1^{st} (a), 3^{rd} (b), 5^{th} (c) and 7^{th} (d) octaves respectively.

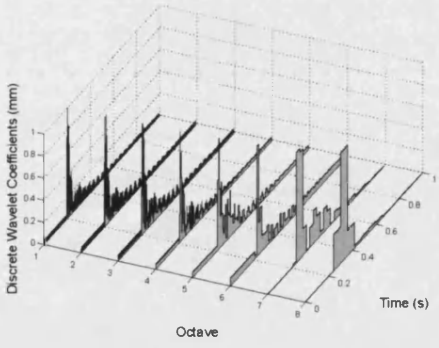

Figure 5.24: Absolute normalized discrete time wavelet series evaluated using Daubechies wavelet 2 in a fixed reference frame due to a rotor unbalance with rotor/auxiliary bearing contact at 425 rad/s.

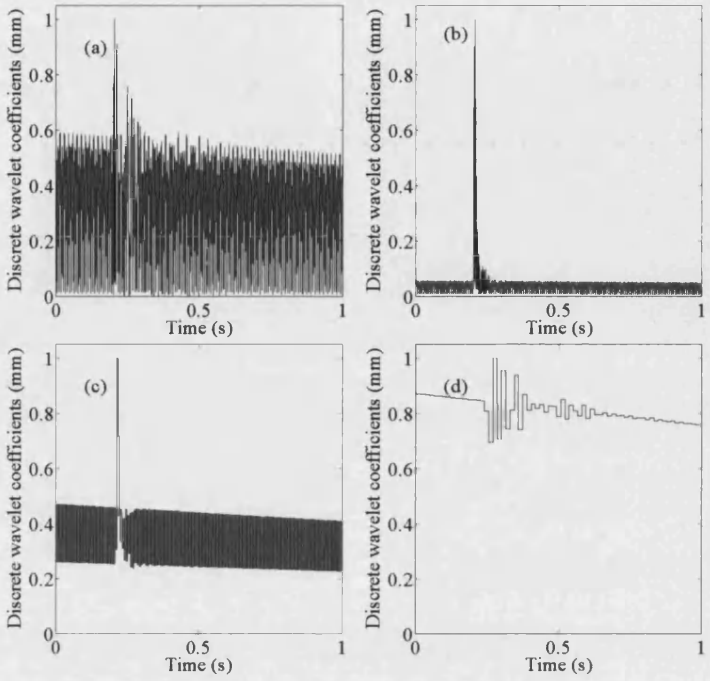

Figure 5.25: Absolute normalized discrete time wavelet series evaluated using Daubechies wavelet 4 in a fixed reference frame due to a rotor unbalance with rotor/auxiliary bearing contact at 425 rad/s. The graphs presented correspond to the 1^{st} (a), 3^{rd} (b), 5^{th} (c) and 7^{th} (d) octaves respectively.

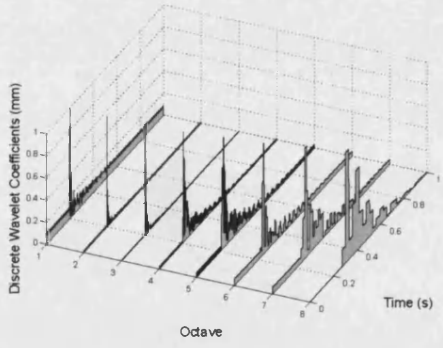

Figure 5.26: Absolute normalized discrete time wavelet series evaluated using Daubechies wavelet 4 in a fixed reference frame due to a rotor unbalance with rotor/auxiliary bearing contact at 425 rad/s.

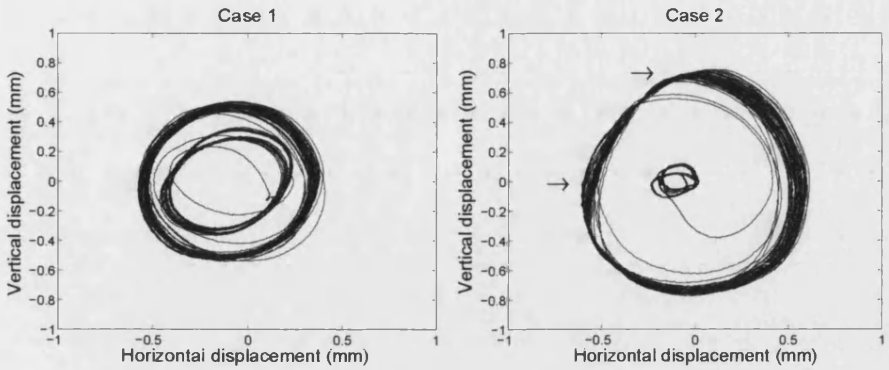

Figure 5.27: Measured rotor orbits at right end rotor disk (sensor plane (7,8)) due to sudden unbalance loss. Contacts occur in case 2 at positions indicated by arrows.

5.3 Experimental Validation

Experimental validation was undertaken using a flexible rotor/ active magnetic bearing system similar to the one modelled in figure 2.1. Mass-loss experiments were performed on the rotor from two different states of initial unbalance. In the first test (case 1) the initial unbalance condition of the rotor was indeterminate. A tied on mass was removed from the right end disk using a blade mechanism, equivalent to causing a sudden unbalance of 516gcm. In the second test (case 2) the initial unbalance condition was changed by adding 250gcm adjacent to the mass loss position on the right end disk. For the second test the sudden unbalance loss was again 516gcm. In both cases, a rotational speed of 19Hz was chosen to excite rotor vibrations above the third critical speed, but sufficiently low to ensure safe operation. On-line digital signal processing of all the sensor signals was undertaken to provide 5 levels of wavelet coefficient for each with pseudo-frequencies corresponding 8, 4, 2, 1, 0.5 times the rotational speed of the rotor, Ω. Figure 5.27 shows the rotor orbit measured at the right hand end of the rotor. Arrows have been added to figure 5.27 to show rotor/bearing contact locations for case 2. The displacements observed in the x direction at the left hand active magnetic bearing (sensor 1) are presented in figure 5.28 for cases 1 and 2. In order to demonstrate the ability to detect non-local fault conditions these signals will be considered along with their constituent wavelet coefficients.

Figure 5.29 shows the absolute values of the synchronous wavelet coefficients present in the signal observed at sensor 1 in fixed and rotating reference frames. The change in rotor vibration is clearly visible in the synchronous coefficients evaluated in a fixed reference frame. The wavelet coefficients evaluated in a synchronously rotating reference frame show a peak (d) for case 2, however, it is harder to identify the

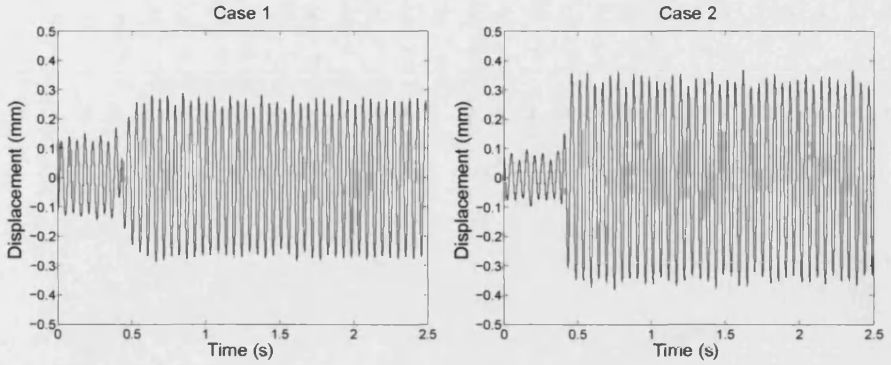

Figure 5.28: Measured motor displacement in the x direction at sensor 3 due to cases 1 and 2.

smaller unbalance response change in rotor vibration for case 1.

During rotor/bearing contact, wavelet coefficients with pseudo-frequencies higher than the rotational speed are excited. This can be seen in figure 5.30 showing the absolute values of the wavelet coefficients with a pseudo-frequency corresponding to 4Ω. In order to highlight rotor/ bearing contact figure 5.30 also shows the change in wavelet coefficients with each sample. It is clear from figures 5.30(c) and 5.30(d) that spikes associated with the sudden change in rotor unbalance are present together with spikes associated with rotor/ bearing contact. It is possible to identify the spikes due to a change in rotor unbalance, indicated by a horizontal arrow. The remaining spikes associated with rotor/ bearing contact in case 2 are present in figure 5.30(d), indicated by vertical arrows. In practice, a threshold setting for the absolute values of the wavelet coefficients could be used to determine whether contact events have occurred.

5.4 Closure

A digital signal processing approach based on filterbank analysis has been undertaken to identify the discrete time wavelet coefficients of rotor displacement in order to ascertain fault onset and type. From an understanding of the fault condition, specific artifacts associated with it can be identified within the wavelet coefficients. The Haar wavelet was chosen as the mother wavelet since its shape is suited for step changes in unbalance and for short duration contacts. Daubechies wavelets 2 and 4 were also considered during simulation.

Consideration of sudden rotor unbalance indicates that in a synchronously rotat-

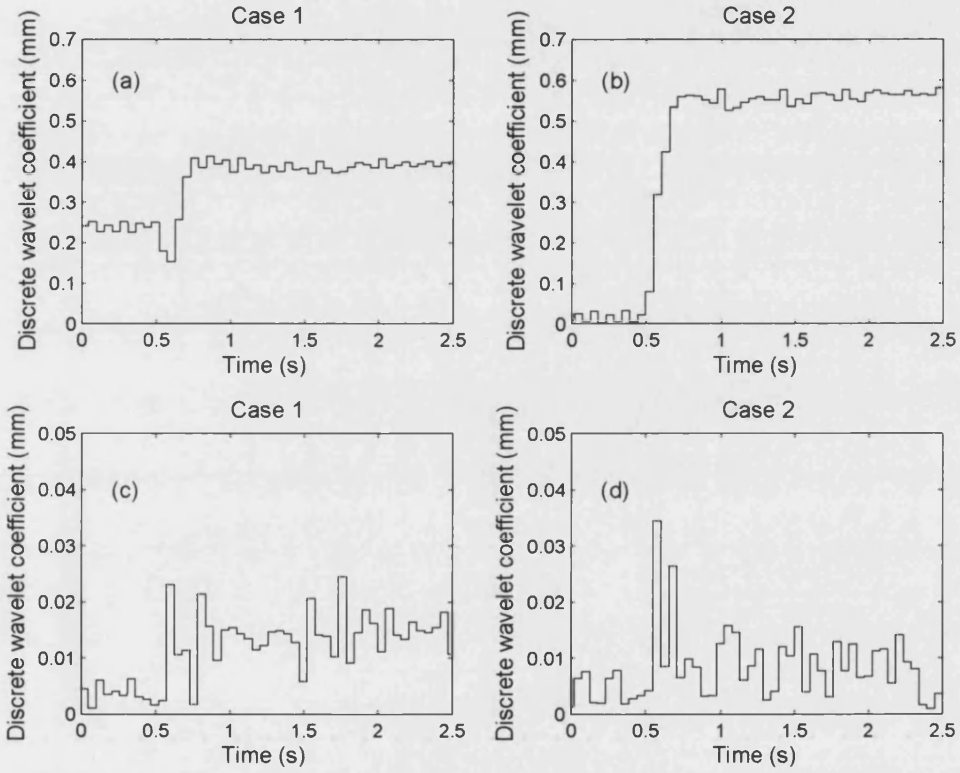

Figure 5.29: Discrete absolute wavelet coefficients corresponding to a pseudo-frequency 1Ω in a fixed reference frame (sensor 3), (a) and (b), and in a synchronously rotating reference frame in sensor plane (3,4), (c) and (d).

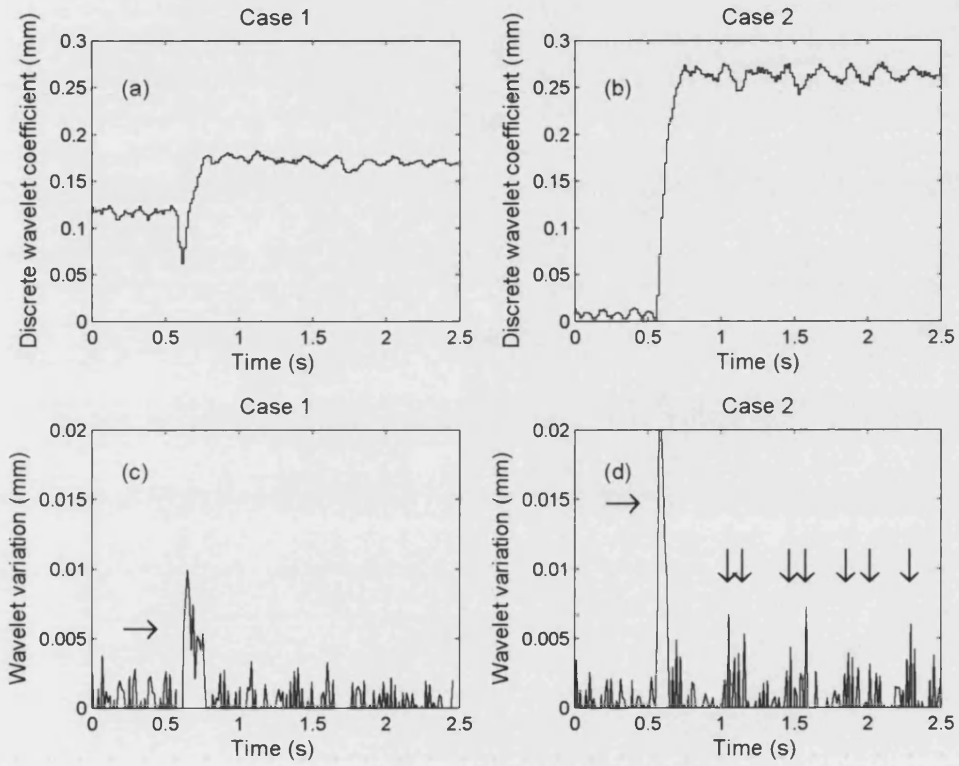

Figure 5.30: Discrete absolute value wavelet coefficients with pseudo frequency 4Ω evaluated in a synchronously rotating reference frame in sensor plane (3,4), (a) and (b). Absolute change in the 4Ω wavelet coefficients with sample time, (c) and (d). Horizontal arrows show the onset of sudden change in rotor unbalance and vertical arrows show excitement of wavelet coefficients due to rotor/ bearing contact.

ing reference frame wavelet coefficients will only be non-zero during the transient response. In the case of rotor/bearing contact it has been shown that non-zero coefficients will also be present only during the transient response. However, in the contact case this is argued to be independent of the reference frame. Furthermore, the non-linearities associated with sudden changes in rotor unbalance and contact will excite multiple pseudo-frequency components. This enables their detection when compared to vibrations of limited bandwidth, such as those induced by base motion or variations in rotor load.

Simulations of a flexible rotor/magnetic bearing system were undertaken at a running speed close to the natural frequency of the second flexible mode of vibration. Rotor displacement resulting from direct synchronous forcing due to a sudden unbalance was shown to contain localized high and low frequency wavelet coefficients in a rotating reference frame. It was also possible to detect the rotor orbit using a wavelet coefficient comparable to the synchronous frequency. Rotor/bearing contact was simulated by progressively increasing the bearing misalignment until contact occurred. After contact the bearing was returned to its original position. High and low frequency vibrations were detected in both the fixed and rotating reference frames along with synchronous vibrations. The onset times of fault conditions were detected and identification of the fault condition could be made from a comparison of wavelet coefficients between the fixed and rotating reference frames. The method of fault identification presented is based around the compact support of the mother wavelet. It is therefore independent of the choice of wavelet used. Simulation of mass loss and rotor/bearing contact were performed using Daubechies wavelets 2 and 4. From simulated results the onset and fault time can be identified for both mother wavelets. However, the Daubechies wavelet 4 corresponds to a longer frequency such that it takes twice as long to evaluate each wavelet coefficient.

Experimental validation was undertaken using a flexible rotor/active magnetic bearing facility subject to sudden rotor unbalance changes sufficient to induce rotor responses with and without auxiliary bearing contact. Artifacts in the wavelet coefficients associated with both the sudden mass loss and the rotor/bearing contact could be distinguished.

Chapter 6

SYSTEM DYNAMICS IN THE WAVELET COEFFICIENT DOMAIN

6.1 Introduction

When analyzing a system or designing a control strategy it is important to have an accurate model of the system. Chapter 2 considers the rotor/active magnetic bearing system and specifies the dynamic equations of motion. However, one of the objectives of this thesis is to identify and realize a control strategy acting in the wavelet coefficient domain. Therefore, the system dynamics of the wavelet coefficients needs to be understood. Figure 6.1 shows three wavelets, ψ_1, ψ_2 and ψ_3, with different translations and dilations. The corresponding bandwidth and time-dispersion are shown as the shaded areas. How will wavelet coefficients of ψ_1 associated with force affect the observed wavelet coefficients at ψ_2 and ψ_3.

The wavelet coefficients of the system states, $\mathbf{x}_{p,q}(kT)$, and the input force, $\mathbf{f}_{a,b}(kT)$, can be expressed as

$$\begin{aligned} \mathbf{x}_{p,q}(kT) &= |p|^{-1/2} \int_{kT-q/2^p}^{kT} \mathbf{x}(t)\psi_x\left(2^p t - q\right) dt, \\ \mathbf{f}_{a,b}(kT) &= |a|^{-1/2} \int_{kT-b/2^a}^{kT} \mathbf{f}(t)\psi_f\left(2^a t - b\right) dt \end{aligned} \tag{6.1}$$

Here, ψ_x and ψ_f are the mother wavelets associated with displacement and force, respectively. The system states and the input disturbance can be represented in

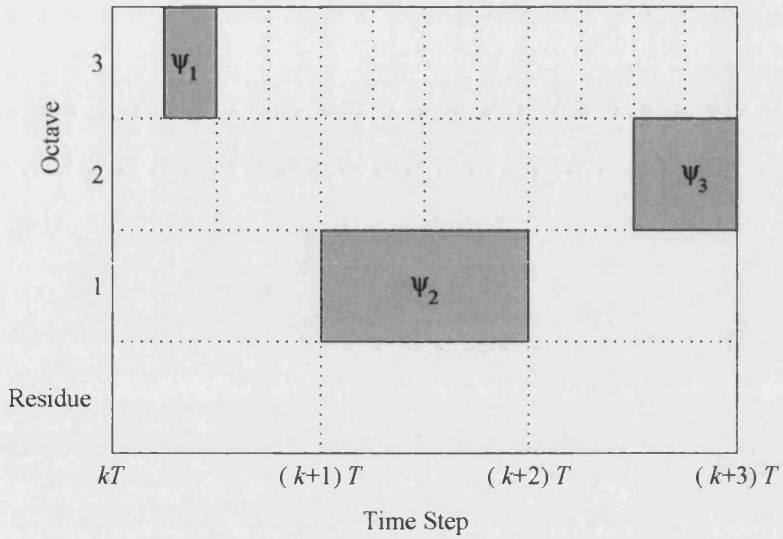

Figure 6.1: Diagram showing three wavelets with different dilations and translations on a sampled grid.

terms of their discrete wavelet coefficients over a limited time period T as:

$$\begin{aligned} \mathbf{x}(t) &= \mathbf{x}^0(T) + \sum_{p=0}^{\infty} \sum_{q=0}^{2^p-1} \mathbf{x}_{p,q}(T)\psi_x\left(2^p t - q\right), \quad 0 \le t < T \\ \mathbf{f}(t) &= \mathbf{f}^0(T) + \sum_{a=0}^{\infty} \sum_{b=0}^{2^a-1} \mathbf{f}_{a,b}(T)\psi_f\left(2^a t - b\right), \quad 0 \le t < T \end{aligned} \tag{6.2}$$

where $\mathbf{x}^0(T)$ and $\mathbf{f}^0(T)$ are the average values of each signal over $[0, T]$. The system states can be represented over successive periods as

$$\mathbf{x}(t) = \begin{cases} \mathbf{x}^0(T) + \sum_{p=0}^{\infty} \sum_{q=0}^{2^p-1} \mathbf{x}_{p,q}(T)\psi_x\left(2^p t - q\right), & 0 \le t < T \\ \mathbf{x}^0(2T) + \sum_{p=0}^{\infty} \sum_{q=0}^{2^p-1} \mathbf{x}_{p,q}(2T)\psi_x\left(2^p t - q\right), & T \le t < 2T \\ \vdots \qquad\qquad\qquad\qquad\qquad\qquad\quad \vdots & \\ \mathbf{x}^0(kT) + \sum_{p=0}^{\infty} \sum_{q=0}^{2^p-1} \mathbf{x}_{p,q}(kT)\psi_x\left(2^p t - q\right), & (k-1)T \le t < kT \\ \vdots \qquad\qquad\qquad\qquad\qquad\qquad\quad \vdots & \end{cases} \tag{6.3}$$

A similar expression can be written to represent the input disturbances on the

system:

$$\mathbf{f}(t) = \begin{cases} \mathbf{f}^0(T) + \sum_{a=0}^{\infty}\sum_{b=0}^{2^a-1} \mathbf{f}_{a,b}(T)\psi_f\left(2^a t - b\right), & 0 \le t < T \\ \mathbf{f}^0(2T) + \sum_{a=0}^{\infty}\sum_{b=0}^{2^a-1} \mathbf{f}_{a,b}(2T)\psi_f\left(2^a t - b\right), & T \le t < 2T \\ \vdots \qquad\qquad\qquad\qquad\qquad\quad \vdots & \\ \mathbf{f}^0(kT) + \sum_{a=0}^{\infty}\sum_{b=0}^{2^a-1} \mathbf{f}_{a,b}(kT)\psi_f\left(2^a t - b\right), & (k-1)T \le t < kT \\ \vdots \qquad\qquad\qquad\qquad\qquad\quad \vdots & \end{cases} \tag{6.4}$$

6.2 Wavelet Coefficients Relation Between Rotor Vibration and Input Disturbance

It is important to have an accurate model of the system in order to evaluate its dynamics or realize a control strategy. The objective is to understand how input disturbances affect rotor vibration. Likewise, when considering the wavelet coefficients in the system it is important to understand how wavelet coefficients of the input disturbance affect wavelet coefficients of the rotor vibration. The Laplace transform of the input disturbance, $\mathbf{f}(t)$, can be expressed in terms of the wavelet coefficient series as

$$\bar{\mathbf{f}}(s) = \sum_{k=1}^{\infty}\int_{(k-1)T}^{kT}\left[\mathbf{f}^0(kT) + \sum_{a=0}^{\infty}\sum_{b=0}^{2^a-1}\mathbf{f}_{a,b}(kT)\psi_f\left(2^a t - b\right)\right]e^{-st}dt \tag{6.5}$$

Define

$$e_1(s,k,T) = -\frac{1}{s}\left(e^{-skT} - e^{-sk(k-1)T}\right) \tag{6.6}$$

and

$$e_2(s,k,T,a,b) = \int_{(k-1)T}^{kT}\psi_f\left(2^a t - b/2^a\right)e^{-st}dt \tag{6.7}$$

$e_1(s,k,t)$ relates to the Laplace transform of the average input disturbance, $\mathbf{f}^0(kT)$, over a single period. $e_2(s,k,t,a,b)$ represents the Laplace transform of the mother wavelet at a specific translation and dilation. The Laplace transform of the input disturbance can then be simplified to

$$\bar{\mathbf{f}}(s) = \sum_{k=1}^{\infty}\left[\mathbf{f}^0(kT)e_1(s,k,T) + \sum_{a=0}^{\infty}\sum_{b=0}^{2^a-1}\mathbf{f}_{a,b}(kT)e_2(s,k,T,a,b)\right] \tag{6.8}$$

The response of the system can be evaluated by superposing the individual modal contributions (see equation (2.21)):

$$\overline{\mathbf{q}}(s) = \sum_{l=1}^{2N} \frac{\mathbf{V}_l \left(\mathbf{V}^{-1}\mathbf{B}\right)_l}{s - \lambda_l} \overline{\mathbf{f}}(s) \tag{6.9}$$

From equation (6.9), the Laplace transform of the system states can be evaluated in terms of the input disturbance wavelet coefficients as

$$\overline{\mathbf{q}}(s) = \sum_{k=1}^{\infty}\sum_{l=1}^{2N} \frac{\mathbf{V}_l \left(\mathbf{V}^{-1}\mathbf{B}\right)_l}{s - \lambda_l} \left[\mathbf{f}^0(kT) e_1(s,k,T) + \sum_{a=0}^{\infty}\sum_{b=0}^{2^a-1} \mathbf{f}_{a,b}(kT) e_2(s,k,T,a,b)\right] \tag{6.10}$$

Poles exist at $s = 0$ and $s = \lambda_l$. Therefore the inverse Laplace transform gives the dynamic system response in the form

$$\mathbf{q}(t) = \sum_{k=1}^{\infty}\sum_{l=1}^{2N} \mathbf{V}_l \left(\mathbf{V}^{-1}\mathbf{B}\right)_l \left[\mathbf{f}^0(kT) u_1(t,\lambda_l,k,T) + \sum_{a=0}^{\infty}\sum_{b=0}^{2^a-1} \mathbf{f}_{a,b}(kT) u_2(t,\lambda_l,k,T,a,b)\right] \tag{6.11}$$

where

$$\begin{aligned} u_1(t,\lambda_l,k,T) &= -\frac{1}{\lambda_l}\left[(e^{\lambda_l(t-kT)} - 1)H(t-kT) - (e^{\lambda_l(t-(k-1)T)} - 1))H(t-(k-1)T)\right] \\ u_2(t,\lambda_l,k,T,a,b) &= \mathcal{L}^{-1}\left[\frac{1}{s-\lambda_l} e_2(s,k,T,a,b)\right] \end{aligned} \tag{6.12}$$

Here $\mathcal{L}^{-1}[.]$ indicates the inverse Laplace transform, and $H(t)$ is the Heaviside step function. The mother wavelets of the input disturbance and the system states are $\psi_f(t)$ and $\psi_x(t)$, which may be different. The relation between the wavelet coefficients of the input disturbance and the system states can be realized from the wavelet transform of $\mathbf{q}(t)$. Define

$$\begin{aligned} g_1(k,mT,\lambda_l,p,q) &= |p|^{-1/2} \int_{(m-1)T}^{mT} u_1(t,\lambda_l,k,T)\psi_x\left(2^p t - q\right) dt \\ g_2(mT,\lambda_l,k,T,a,b,p,q) &= |p|^{-1/2} \int_{(m-1)T}^{mT} u_2(t,\lambda_l,k,T,a,b)\psi_x\left(2^p t - q\right) dt \end{aligned} \tag{6.13}$$

Equation (6.11) can be transformed into the wavelet coefficient domain as:

$$\mathbf{q}_{p,q}(mT) = \sum_{k=1}^{m-1}\sum_{l=1}^{2N}\mathbf{V}_l\left(\mathbf{V}^{-1}\mathbf{B}\right)_l\Big[\mathbf{f}^0(kT)g_1(k,mT,\lambda_l,p,q) + \sum_{a=0}^{\infty}\sum_{b=0}^{2^a-1}\mathbf{f}_{a,b}(kT)g_2(mT,\lambda_l,k,T,a,b,p,q)\Big] \tag{6.14}$$

The change in response of the system over successive periods can be identified from the difference equation $\mathbf{q}_{p,q}((m+1)T) - \mathbf{q}_{p,q}(mT)$:

$$\begin{aligned}\mathbf{q}_{p,q}((m+1)T) - \mathbf{q}_{p,q}(mT) = &\sum_{l=1}^{2N}\mathbf{V}_l\left(\mathbf{V}^{-1}\mathbf{B}\right)_l \times \\ &\left[\left(\mathbf{f}^0((m+1)T)g_1((m+1),(m+1)T,\lambda_l,p,q) - \mathbf{f}^0(mT)g_1(m,mT,\lambda_l,p,q)\right)\right. \\ &+\sum_{a=0}^{\infty}\sum_{b=0}^{2^a-1}\left(\mathbf{f}_{a,b}((m+1)T)g_2(mT,\lambda_l,(m+1),T,a,b,p,q)\right. \\ &\left.\left.-\mathbf{f}_{a,b}(mT)g_2(mT,\lambda_l,m,T,a,b,p,q)\right)\right]\end{aligned} \tag{6.15}$$

Taking the Z-transform of equation (6.15) and using the notation

$$\begin{aligned}\mathbf{q}_{p,q}(mT) &\rightarrow \mathbf{Q}_{p,q}(z)\\ \mathbf{f}_{a,b}(mT) &\rightarrow \mathbf{F}_{p,q}(z)\\ \mathbf{f}^0(mT) &\rightarrow \mathbf{F}^0(z)\\ g_1(m,mT,\lambda_l,p,q) &\rightarrow G_1(z,\lambda_l,p,q)\\ g_2(mT,\lambda_l,m,T,a,b,p,q) &\rightarrow G_2(z,\lambda_l,T,a,b,p,q)\end{aligned} \tag{6.16}$$

gives

$$\begin{aligned}(z-1)\mathbf{Q}_{p,q}(z) = &\sum_{l=1}^{2N}\mathbf{V}_l\left(\mathbf{V}^{-1}\mathbf{B}\right)_l \times \\ &\left[\mathbf{F}^0(z)(z^2-1)G_1(z,\lambda_l,p,q) + \sum_{a=0}^{\infty}\sum_{b=0}^{2^a-1}(z^2-1)\mathbf{F}_{a,b}(z)G_2(z,\lambda_l,T,a,b,p,q)\right]\end{aligned} \tag{6.17}$$

The relation between the input disturbance wavelet coefficients and the system states wavelet coefficients can now be expressed as:

$$\mathbf{Q}_{p,q}(z) = \mathbf{G}^0_{p,q}(z)\mathbf{F}^0(z) - \sum_{a=0}^{\infty}\sum_{b=0}^{2^a-1}\mathbf{G}_{p,q,a,b}(z)\mathbf{F}_{a,b}(z) \tag{6.18}$$

where

$$\begin{aligned}\mathbf{G}^0_{p,q}(z) &= \sum_{l=1}^{2N}(z+1)\mathbf{V}_l\left(\mathbf{V}^{-1}\mathbf{B}\right)_l G_1(z,\lambda_l,p,q)\\ \mathbf{G}_{p,q,a,b}(z) &= \sum_{l=1}^{2N}(z+1)\mathbf{V}_l\left(\mathbf{V}^{-1}\mathbf{B}\right)_l G_2(z,\lambda_l,T,a,b,p,q))\end{aligned} \tag{6.19}$$

$\mathbf{G}^0_{p,q}(z)$ is the transfer function relating a constant input disturbance over a fixed time period to the measured rotor displacement. $\mathbf{G}_{p,q,a,b}(z)$ relates wavelet coefficients present in the input disturbance to the wavelet coefficients in the rotor vibration.

6.3 Evaluation of Transfer Function Using Haar Wavelet

The relation between the wavelet coefficients present in the input disturbance and the system states has been formulated. However, in order to evaluate the system transfer functions the input disturbance and the system states mother wavelets need to be specified. The simplest wavelet to represent mathematically is the Haar wavelet:

$$\psi_{x,f}(t) = \begin{cases} 1 & 0 \le t < 1/2 \\ -1 & 1/2 \le t < 1 \\ 0 & \text{otherwise} \end{cases} \tag{6.20}$$

$g_1(k, mT, \lambda_l, p, q)$ has been defined in equation (6.13) as:

$$g_1(k,mT,\lambda_l,p,q) = |p|^{-1/2}\int_{(m-1)T}^{mT} u_1(t,\lambda_l,k,T)\psi_x\left(2^p t - q\right)dt \tag{6.21}$$

Taking the Z-transform gives

$$\begin{aligned}&G_1(z,\lambda_l,p,q) = \\ &\left[\frac{1}{|p|^{1/2}\lambda_l^2}\left(1-e^{-\lambda_l T}\right)\left(2e^{-2^p+2^{-q/2}} - e^{-2^p+2^{-q}} - e^{-2^p}\right)\right]\left(\frac{z(z+1)}{z-e^{-2\lambda_l T}}\right)\end{aligned} \tag{6.22}$$

$G_1(k,z,\lambda_l,p,q)$ represents the Z-domain transfer function between the average input disturbance over a single period to the wavelet coefficients present in the system states. $G_2(z,\lambda_l,a,b,p,q)$ corresponds to the Z-domain transfer function relating the input wavelet disturbance to the wavelet coefficients in the system states. Evaluating $G_2(z,\lambda_l,a,b,p,q)$ for the Haar wavelet requires $g_2(mT,\lambda_l,k,T,a,b,p,q)$ to be evaluated. $g_2(mT,\lambda_l,k,T,a,b,p,q)$ has been defined in equation (6.13):

$$g_2(mT,\lambda_l,k,T,a,b,p,q) = |p|^{-1/2}\int_{(m-1)T}^{mT} u_2(t,\lambda_l,k,T,a,b)\psi_x\left(2^p t - q\right)dt \tag{6.23}$$

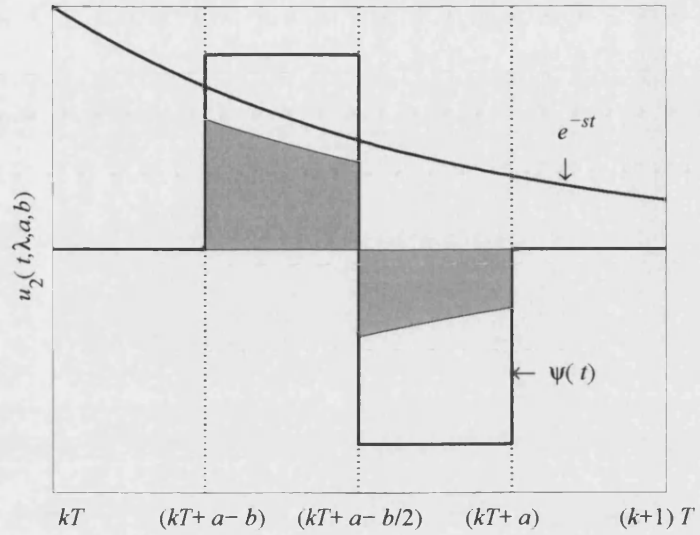

Figure 6.2: $u_2(t, \lambda_l, a, b)$ (shaded). The Laplace variable, s, is assumed positive for diagrammatic purposes.

where

$$u_2(t, \lambda_l, k, T, a, b) = \mathcal{L}^{-1}\left[\frac{1}{s-\lambda_l}\int_{(k-1)T}^{kT} \psi_f\left(2^a t - b\right) e^{-st} dt\right] \tag{6.24}$$

The Haar wavelet is only non-zero within the region dictated by its translation and dilation. The maximum size of the dilation is fixed to the size of the period over which the signal is observed. Larger scale wavelets are considered as part of the average signal. The Laplace transform of the mother (Haar) wavelet over a single period is

$$\int_{(k-1)T}^{kT} \psi_f\left(2^a t - b\right) e^{-st} dt = -\frac{e^{(k-1)T}}{s}\left[2e^{sr_2(a,b)} - e^{sr_3(a,b)} - e^{sr_1(a,b)}\right] \tag{6.25}$$

where $r_i(a, b)$ is used to define the delays associated with the step changes in the Haar wavelet:

$$\begin{aligned} r_1(a,b) &= -2^a \\ r_2(a,b) &= -2^a + 2^{-b/2} \\ r_3(a,b) &= -2^a + 2^{-b} \end{aligned} \tag{6.26}$$

From equation (6.24) the inverse Laplace transform can be used to evaluate $u_2(t, \lambda_l, k, T, a, b)$:

$$\begin{aligned} u_2(t,\lambda_l,k,T,a,b) =& \frac{e^{(k-1)T}}{\lambda_l}\left(e^{\lambda_l(t-r_1(a,b))}-1\right)H(t-r_1(a,b)) \\ &+\frac{e^{(k-1)T}}{\lambda_l}\left(e^{\lambda_l(t-r_3(a,b)}-1\right)H(t-r_2(a,b)) \\ &-\frac{2e^{(k-1)T}}{\lambda_l}\left(e^{\lambda_l(t-r_2(a,b)}-1\right)H(t-r_3(a,b)) \end{aligned} \tag{6.27}$$

The expressions $u_2(t, \lambda_l, k, T, a, b)$ may be substituted into equation (6.23) and used to evaluate the integral. The constant terms will disappear as wavelets have zero mean. The step functions will be unity since $1 \leq k \leq m-1$. Therefore

$$\begin{aligned} &\int_{(m-1)T}^{mT} u_2(t,\lambda_l,k,T,a,b)\psi_x\left(2^p t-q\right)dt = \\ &\int_{(m-1)T}^{mT} \frac{1}{\lambda_l}e^{(k-1)T}\left[e^{\lambda_l(t-r_1(a,b))}+e^{\lambda_l(t-r_3(a,b))}-2e^{\lambda_l(t-r_2(a,b))}\right]\psi_x\left(2^p t-q\right)dt \end{aligned} \tag{6.28}$$

giving

$$\begin{aligned} &\int_{(m-1)T}^{mT} u_2(t,\lambda_l,k,T,a,b)\psi_x\left(2^p t-q\right)dt = \\ &\frac{-e^{\lambda_l(k+m)T}e^{-2\lambda_l T}}{\lambda_l^2}\left[e^{-\lambda_l r_1(a,b)}+e^{-\lambda_l r_3(a,b)}-2e^{-\lambda_l r_2(a,b)}\right]\times \\ &\left[e^{\lambda_l r_1(p,q)}+e^{\lambda_l r_3(p,q)}-2e^{\lambda_l r_2(p,q)}\right] \end{aligned} \tag{6.29}$$

Define

$$\begin{aligned} R_1(\lambda_l,a,b) &= \left[e^{-\lambda_l r_1(a,b)}+e^{-\lambda_l r_3(a,b)}-2e^{-\lambda_l r_2(a,b)}\right] \\ R_2(\lambda_l,p,q) &= \left[e^{\lambda_l r_1(p,q)}+e^{\lambda_l r_3(p,q)}-2e^{\lambda_l r_2(p,q)}\right] \end{aligned} \tag{6.30}$$

Here $R_1(\lambda_l, a, b)$ and $R_1(\lambda_l, p, q)$ are dictated by the input and output mother wavelets. Converting equation (6.23) to the Z-domain gives

$$G_2(z,\lambda_l,a,b,p,q) = \frac{e^{-2\lambda_l T}}{|p|^{1/2}\lambda_l^2}R_1(\lambda_l,a,b)R_2(\lambda_l,p,q)\left(\frac{z(z+1)}{z-e^{-2\lambda_l T}}\right) \tag{6.31}$$

$\mathbf{G}_{p,q,a,b}(z)$ can then be evaluated as

$$\mathbf{G}_{p,q,a,b}(z) = \sum_{l=1}^{2N}\mathbf{V}_l\left(\mathbf{V}^{-1}\mathbf{B}\right)_l\frac{e^{-2\lambda_l T}}{|p|^{1/2}\lambda_l^2}R_1(\lambda_l,a,b)R_2(\lambda_l,p,q)\left(\frac{z(z+1)}{z-e^{-2\lambda_l T}}\right) \tag{6.32}$$

Also

$$\mathbf{G}^0_{p,q}(z) = \sum_{l=1}^{2N} \mathbf{V}_l \left(\mathbf{V}^{-1}\mathbf{B}\right)_l \frac{1}{|p|^{1/2}\lambda_l^2} \left(1 - e^{-\lambda_l T}\right) R_2(\lambda_l, p, q) \left(\frac{z(z+1)}{z - e^{-2\lambda_l T}}\right) \quad (6.33)$$

From $\mathbf{G}_{p,q,a,b}(z)$ and $\mathbf{G}^0_{p,q}(z)$ a full model of the system in the wavelet coefficient domain can be evaluated. There are similarities between $\mathbf{G}_{p,q,a,b}(z)$ and $\mathbf{G}^0_{p,q}(z)$ arising from similarities between the step changes in the Haar wavelet and the step changes in average system disturbance. This is seen by the inclusion of $R_1(\lambda_l, a, b)$ in $\mathbf{G}_{p,q,a,b}(z)$ representing the input disturbance wavelet.

6.4 System Identification

From equation (6.18), the transient response of the system is determined by knowledge of $\mathbf{G}_{p,q,a,b}(z)$. In principle, equation (6.19) may be evaluated from system modelling. However, this may lead to uncertainties due to discretization errors. An alternative method is to identify $\mathbf{G}_{p,q,a,b}(z)$ using direct measurement. The rotor response due to a step input in the wavelet coefficients at a level a, applied through the magnetic bearings, can be measured. Gain matrices, $\mathbf{A}^{(k)}_{p,q,a,b}$, can then be identified to represent the transfer function of the system at a given time step and level p:

$$\mathbf{G}_{p,q,a,b}(z) = \sum_{k=1}^{\infty} \frac{\mathbf{A}^{(k)}_{p,q,a,b}}{z^k} \quad (6.34)$$

The pseudo-inverse transfer function can then be expressed as:

$$\mathbf{G}_{p,q,a,b}(z)^* \mathbf{B}_u = \sum_{k=1}^{\infty} \frac{\mathbf{B}^{(k)}_{p,q,a,b}}{z^k} \quad (6.35)$$

where the $\mathbf{B}^{(k)}_{p,q,a,b}$ are derived from sets of linear equations.

Experimental determination of the system transfer functions is based around a step change in the system disturbance applied through an active magnetic bearing control axis. The system transfer function between control axis and measurement sensor can then be identified. This process can be repeated to identify the transfer functions due to all magnetic bearing control axis and sensor combinations. Experimentally determined inverse system transfer functions are presented for the system at the natural frequencies 11Hz and 18Hz (figures 6.3 and 6.4). A multiple wavelet approach to inverse system identification was undertaken at 22Hz. The inverse system transfer functions at wavelet coefficient levels 1, 2 and 3 are identified and presented in figures 6.5, 6.6 and 6.7 respectively.

Figures 6.3 to 6.7 show the wavelet coefficient response of the system at sensor

1 a to step change in the wavelet coefficient disturbance applied through a single magnetic bearing axis (figure caption (a)). The system can be seen to undergo a transient response before settling into a steady state. The inverse system response evaluated from equation (6.35), is shown in figure captions (b) and (c) truncated after 10 and 5 time steps. The inverse transfer function is truncated to allow for practical implementation. Applying the same process in all the control axis and measuring the response at all the sensor locations allows a full model of the system to be constructed, from which a full inverse dynamic model can be evaluated.

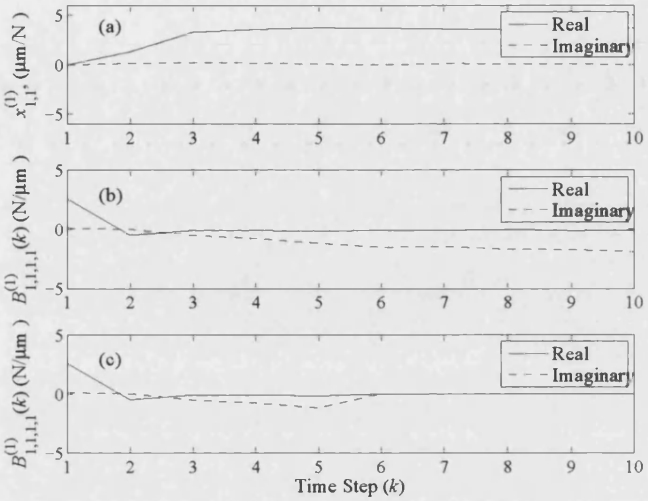

Figure 6.3: System identification at sensor 1 due to Haar wavelet harmonic forcing in control axis 1 at rotational speed of 11Hz, (a) measured synchronous harmonic wavelet coefficients , (b) 10^{th} order inverse transfer function, (c) 5^{th} order inverse transfer function.

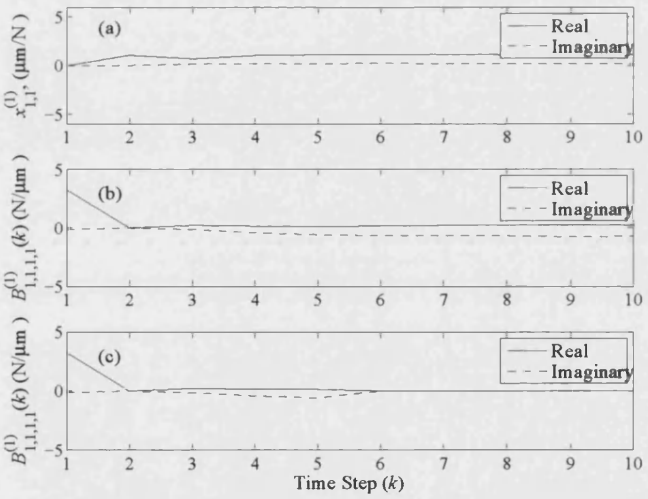

Figure 6.4: System identification at sensor 1 due to Haar wavelet harmonic forcing in control axis 1 at rotational speed of 18Hz, (a) measured synchronous harmonic wavelet coefficients , (b) 10^{th} order inverse transfer function, (c) 5^{th} order inverse transfer function.

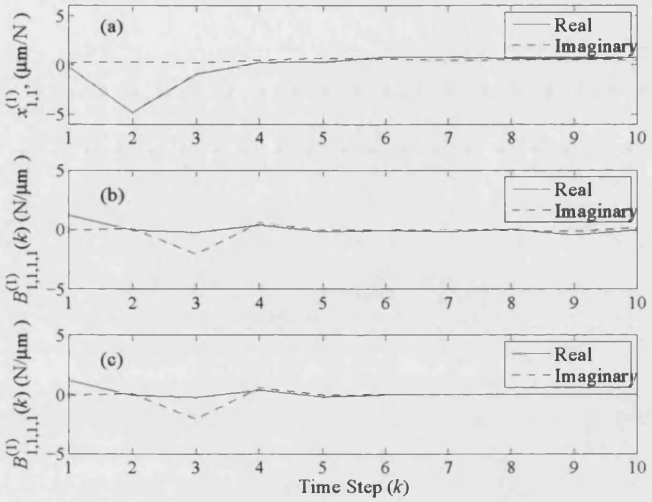

Figure 6.5: Level 1 system identification at sensor 1 due to Haar wavelet level 1 harmonic forcing in control axis 1 at rotational speed of 22Hz. (a) measured synchronous harmonic wavelet coefficients , (b) 10^{th} order inverse transfer function, (c) 5^{th} order inverse transfer function.

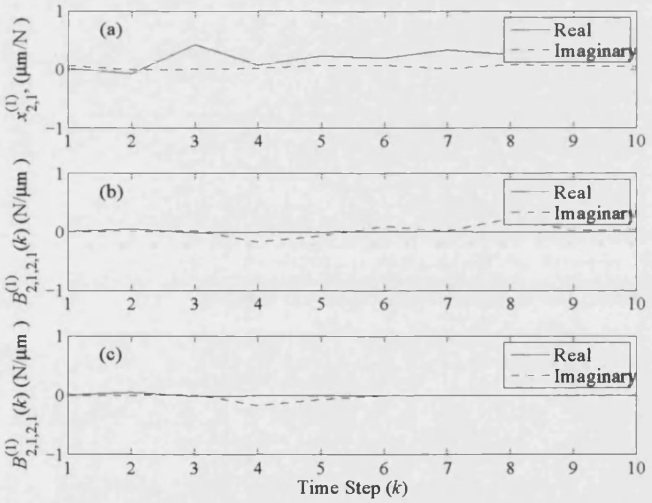

Figure 6.6: Level 2 system identification at sensor 1 due to Haar wavelet level 2 harmonic forcing in control axis 1 at rotational speed of 22Hz. (a) measured synchronous harmonic wavelet coefficients , (b) 10^{th} order inverse transfer function, (c) 5^{th} order inverse transfer function.

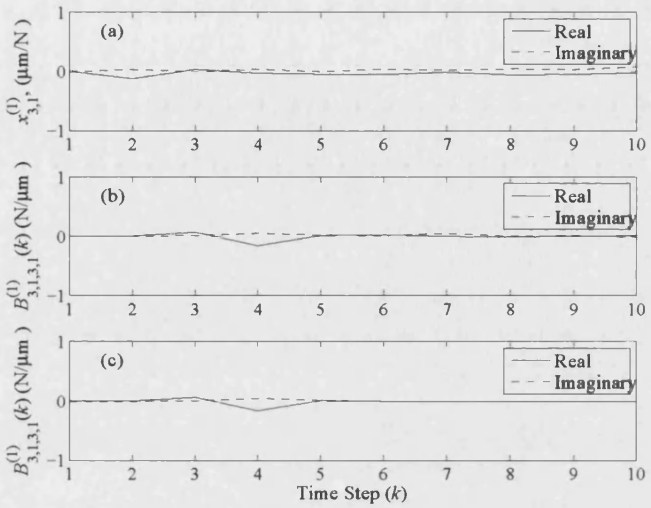

Figure 6.7: Level 3 system identification at sensor 1 due to Haar wavelet level 3 harmonic forcing in control axis 1 at rotational speed of 22Hz. (a) measured synchronous harmonic wavelet coefficients , (b) 10^{th} order inverse transfer function, (c) 5^{th} order inverse transfer function.

6.5 Closure

A framework for identifying the wavelet coefficient behaviour of a system has been presented. This leads to a generalized formulation of the wavelet coefficient transfer functions. This framework allows for different input and output mother wavelets and the comparison of different wavelet coefficient levels. An example case is presented evaluating the wavelet coefficient transfer function for a system using the Haar wavelet. This is a novel technique allowing the study of systems in the wavelet coefficient domain.

Experimental identification of the system inverse transfer functions has been presented at 11Hz and 18Hz corresponding to the first two natural frequencies of the PID controlled rotor. Furthermore, a multi-level system identification has been presented to identify the inverse transfer functions at wavelet coefficient levels 1, 2 and 3 at an operating frequency of 22Hz.

Chapter 7

WAVELET COEFFICIENT STEADY STATE IDENTIFICATION AND CONTROLLER MODERATION

7.1 Introduction

In principle, if a controller can provide a 'perfect' control signal at the same time as a change in the input disturbance, or onset of an external fault condition, then the rotor vibration will be zero. However, high system order in robust controller design limits the response speed of the controllers. Synchronous and multi-frequency controllers offer a faster response time however may provide inappropriate control forces during transient excitation. To overcome the problems associated with synchronous and multi-frequency controllers a digital signal processing method to identify the steady state vibration using wavelet analysis is proposed. The predicted steady state signal can then be used to reconfigure a control strategy or form the input signal to the controller itself.

7.2 Wavelet Steady State Prediction

The objective is to predict the steady state magnitudes of the wavelet coefficients in the rotor vibration due to a step change in wavelet coefficient input disturbance

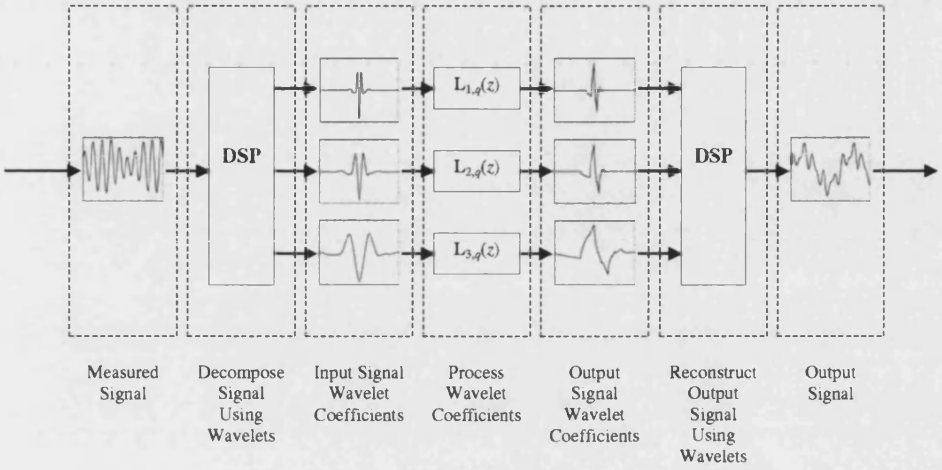

Figure 7.1: Signal processing structure through parallel wavelet coefficient manipulation.

at a given level. A step change in the input disturbance can be expressed as

$$\mathbf{F}_{a,b}(z) = \frac{1}{z-1}\mathbf{B}_u \tag{7.1}$$

Steady state prediction of the system is based around the determination of the steady state values at multiple wavelet coefficient levels. From full signal reconstruction the steady state response of the system can be evaluated. The measured states of the system can be extracted using the matrix $\mathbf{B}^{(m)}$ as $\mathbf{Q}^{(m)}_{p,q}(z) = \mathbf{B}^{(m)}\mathbf{Q}_{p,q}(z)$. The relation between the measured states and the measured steady state wavelet coefficients, $\mathbf{W}^{(m)}_{p,q}(z)$, can be expressed as:

$$\mathbf{W}^{(m)}_{p,q}(z) = \mathbf{S}_{p,q}(z)\mathbf{Q}^{(m)}_{p,q}(z) \tag{7.2}$$

where $\mathbf{S}_{p,q}(z)$ represents the steady state operator acting on wavelet coefficients at level p. Although in this case $\mathbf{S}_{p,q}(z)$ is designed to extract the steady state response from $\mathbf{Q}^{(m)}_{p,q}(z)$ it could also be designed to produce any dynamic. The dynamic equation of the system with steady state prediction can be expressed as

$$\mathbf{W}_{p,q}^{(m)}(z) = \mathbf{G}_{p,q}^{0}(z)\mathbf{F}^{0}(z) - \mathbf{S}_{p,q}(z)\mathbf{B}^{(m)} \sum_{a=0}^{\infty} \sum_{b=0}^{2^a-1} \mathbf{G}_{p,q,a,b}(z)\mathbf{F}_{a,b}(z) \tag{7.3}$$

Assuming the system disturbance is periodic and there are sufficient wavelet coefficient levels to represent all frequencies, then any change in the disturbance can be described using in $\mathbf{F}_{a,b}(z)$. This dictates the number of wavelet coefficient level used in the steady state prediction along with their dilations. The desired output, $\mathbf{W}_{p,q}^{(m)}(z)$, is a step change with magnitude matching the steady state wavelet coefficients at that level:

$$\mathbf{W}_{p,q}^{(m)}(z) = \mathbf{\Gamma}_{p,q}^{(m)} \frac{1}{z-1} \tag{7.4}$$

where from the final value theorem,

$$\mathbf{\Gamma}_{p,q}^{(m)} = \lim_{z \to 1}(1 - z^{-1})\mathbf{Q}_{p,q}^{(m)}(z) \tag{7.5}$$

$\mathbf{\Gamma}_{p,q}^{(m)}$ is a gain matrix containing the steady state wavelet coefficients of the system states. Then

$$\mathbf{S}_{p,q}(z) = \mathbf{\Gamma}_{p,q}^{(m)} \left(\mathbf{G}_{p,q,p,q}(z)\mathbf{B}_u\right)^* \tag{7.6}$$

Here $(.)^*$ indicates the pseudo-inverse. In this case the desired output is the steady state wavelet coefficients. However, this method can be applied to produce any desired output dynamic.

7.3 Wavelet Coefficient Prediction Steady State Control Strategy

Wavelet decomposition allows for the identification of wavelet coefficients corresponding to specific frequency bandwidths present in measured rotor vibration. Conversely, wavelet reconstruction can be used to create control signals from wavelet coefficients. Applying a control strategy in the wavelet coefficient domain allows for loop shaping of the wavelet coefficients. This provides a method of control, targeting specific components within the measured signal.

Initial rotor/active magnetic bearing stability is achieved using proportional-differential control with additional integral action to reduce the steady state error. A simple proportional controller is proposed to provide control action in the wavelet coefficient domain. This forms the basis of a simple control strategy acting on a specific wavelet coefficient. To overcome control instabilities during transient rotor excitation the steady state wavelet coefficient identification will be used to moderate the control signal.

The wavelet control coefficients can be evaluated as $\mathbf{U}_{p,q}(z) = -\mathbf{L}_{p,q}(z)\mathbf{Q}^{(m)}_{p,q}(z)$ where for proportional control $\mathbf{L}_{p,q}(z) = k_{p,q}$. In the case of the proportional predicted steady state controller the wavelet control coefficients will take the form $\mathbf{U}_{p,q}(z) = -\mathbf{L}_{p,q}(z)\mathbf{W}^{(m)}_{p,q}(z)$. The closed loop response can be identified as:

$$\left(\mathbf{I} - \mathbf{G}_{p,q,p,q}(z)\mathbf{B}_u\mathbf{L}_{p,q}(z)\right)\mathbf{Q}^{(m)}_{p,q}(z) = \mathbf{G}^0_{p,q}(z)\mathbf{F}^0(z) - \sum_{a=0}^{\infty}\sum_{b=0}^{2^a-1}\mathbf{G}_{p,q,a,b}(z)\mathbf{F}_{a,b}(z) \tag{7.7}$$

With steady state prediction this becomes:

$$\left(\mathbf{I} - \mathbf{G}_{p,q,p,q}(z)\mathbf{B}_u\mathbf{L}_{p,q}(z)\mathbf{S}_{p,q}(z)\right)\mathbf{Q}^{(m)}_{p,q}(z) = \mathbf{G}^0_{p,q}(z)\mathbf{F}^0(z) - \sum_{a=0}^{\infty}\sum_{b=0}^{2^a-1}\mathbf{G}_{p,q,a,b}(z)\mathbf{F}_{a,b}(z) \tag{7.8}$$

In reality, implementation of a wavelet coefficient domain controller will result in evaluation delays between the rotor displacement measurements and control forces. Incorporating delays into the controller gives $\mathbf{L}_{p,q}(z) = k_{p,q}/z^i$, where i indicates the number of cycles over which the control signal is delayed. This can also be used to incorporate any delays associated with the evaluation of the predicted steady state vibration. The closed loop system response with controller evaluation delays can be expressed as

$$\left(\mathbf{I} - \mathbf{G}_{p,q,p,q}(z)\mathbf{B}_u\frac{k_{p,q}}{z^i}\mathbf{S}_{p,q}(z)\right)\mathbf{Q}^{(m)}_{p,q}(z) = \mathbf{G}^0_{p,q}(z)\mathbf{F}^0(z) - \sum_{a=0}^{\infty}\sum_{b=0}^{2^a-1}\mathbf{G}_{p,q,a,b}(z)\mathbf{F}_{a,b}(z) \tag{7.9}$$

7.4 Experimental Validation

The parameters to be presented and their descriptions are shown in Table 7.1. The steady state predictor was configured with three wavelet coefficient levels having pseudo-frequencies corresponding to 1×, 2× and 4× the rotational speed of the rotor. These correspond to wavelet coefficients $x^{(i)}_{1,1}$, $x^{(i)}_{2,1}$ and $x^{(i)}_{3,1}$ respectively, where (i) indicates a specific measurement channel. The wavelet decomposition residue is set to zero. The predictive steady state transfer functions for each wavelet coefficient level were identified using equation (7.6). The inverse plant dynamics for each wavelet coefficient level, $(\mathbf{G}_{p,q,p,q}(z)\mathbf{B}_u)^*$, were identified from on-line identification. The inverse transfer function using the Haar at wavelet coefficient level 1 for an operating speed of 22Hz was identified and truncated after 10 and 5 time steps (figures 6.5(b) and 6.5(c)). The inverse transfer functions at wavelet coefficient levels 2 and 3 have also been identified and are presented in figures 6.6 and 6.7.

Table 7.1: Measurement parameter terminology.

Parameter	Description
$x^{(i)}$	Displacement measured by sensor i
$x_{1,1}^{(i)}$	Wavelet coefficient $(p = 1, q = 1)$ of displacement measured by sensor i
$u^{(j)}$	Magnetic bearing force in the j^{th} control axis
$u_{1,1}^{(j)}$	Wavelet coefficient $(p = 1, q = 1)$ of force in the j^{th} control axis

7.4.1 Step Synchronous Force Tests

Step Synchronous force tests were performed by applying a sudden change in the synchronous disturbance force of 200N acting on the rotor through a single active magnetic bearing. A rotational speed of 22Hz was selected to correspond to non-critical frequencies above the second rigid body mode of the rotor. Figure 7.2 shows the measured rotor vibration in the x-axis and the predicted steady state response of the system at a rotational speed of 22Hz. The measured response of the rotor undergoes a transient period before settling into a steady state. In particular, large transient overshoots are seen in the responses. The predictive steady state response of the system has a greatly reduced transient response with a marginal transient overshoot and matches the steady state amplitude of the measured response. There is a delay in the predictive steady state of approximately 0.3s associated with the wavelet coefficient evaluation, steady state prediction and signal reconstruction. Figures 7.3, 7.4, and 7.5 show the measured and predicted steady state Haar wavelet coefficient values corresponding $1\times$, $2\times$ and $4\times$ the rotational speed of the rotor. The transient response of the system is clearly evident in the wavelet coefficients of the measured response. The predictive steady state wavelet coefficients are seen to have a much shorter transient response reaching steady state before the system. The rotor measured and predicted responses in the x-axis using Daubechies wavelets 2 and 4 are shown in figures 7.6 and 7.10, respectively. Figures 7.7-7.9 and 7.11-7.13 show the measured and predicted steady state wavelet coefficient values corresponding $1\times$, $2\times$ and $4\times$ the rotational speed of the rotor. The steady state controller is seen to identify the steady state wavelet coefficients, using several different mother wavelets, effectively during the transient response allowing for an accurate prediction of the steady state of the system.

7.4.2 Mass-Loss Tests

Experimental validation of the control strategy was performed using mass loss tests to include a step change in rotor unbalance from an initially indeterminate state. Mass loss was induced by cutting free an attached mass at the non-driven end disk using a blade mechanism (figure ref 2.1). The effective mass loss eccentricity was 196gcm. Two wavelet coefficient controllers were identified, one with proportional wavelet coefficient feedback and the other with predictive steady state proportional wavelet coefficient feedback. To minimize the number of variables and allow for a direct comparison, both controllers were configured from a single wavelet coefficient level. The inverse transfer function used in steady state prediction was identified and truncated to 5 time steps to allow for real time controller implementation. Wavelet control force evaluation corresponds to a 3 cycle delay. Controller stability was assessed using a acceptability bound on performance. A controller was defined as unacceptable if the rotor displacement exceeded a specified limit, 0.5mm, in any control plane. The acceptability boundaries for the controllers were identified as $k_{1,1} = 0.68$ and $k_{1,1} = 0.41$ for the predictive steady state controller and the conventional controller, respectively. To assess controller performance a wavelet coefficient feedback gain corresponding to 50% of the maximum acceptable limit was used. This provides a comparison of the controllers at similar performance demands relative to their maximum. These correspond to $k_{1,1} = 0.34$ for the predictive steady state controller and $k_{1,1} = 0.21$ for the and the conventional controller.

The rotor displacements in the x-axis for the rotor configured with local PID control case are shown in figure 7.14 along with their corresponding wavelet coefficients. The demand control forces are shown in figure 7.15. Since there is no additional controller the wavelet control coefficients are zero. The measured response to the mass-loss disturbance is an increase in the rotor orbit with an initial transient component. Figures 7.16 and 7.18 show the rotor displacement in the x-axis using the proportional wavelet coefficient controller and the proportional wavelet controller with predictive steady state moderation in addition to the local PID controller. The corresponding control forces are presented in figures 7.17 and 7.19 respectively. Mass-loss experiments show that both controllers suppress rotor vibration. There is a marginal improvement in the system response with just proportional wavelet coefficient feedback. This is due to the delay between measuring the wavelet coefficients in the system response and evaluation the appropriate control force. In the case of direct wavelet coefficient feedback, the upper limit on feedback gain, ensuring system stability, is small. This results in a conservative control strategy. Moderating the controller input using predictive steady state measurements increased stability margins allowing for improved system performance. This is seen in figure 7.18 showing a greater reduction in the rotor orbit. These problems are largely associated with the delays incurred in the evaluation of the control signals. Predictive steady state moderation is therefore an improvement allowing for increased control action during transient vibrations.

7.5 Closure

A method of identifying the steady state rotor vibration using wavelet coefficients has been presented. Experimental validation of the technique was performed using step changes of synchronous forcing applied by the magnetic bearings. Results indicate that this method provides an accurate estimation of the steady state response and is able to reduce the transient response time.

A simple proportional wavelet coefficient controller was introduced as a method of targeting specific rotor vibration. The controller took the form of proportional feedback applied in the wavelet coefficient domain. A second controller was identified using predictive steady state techniques as a method of moderating the control forces. Experimental validation of the controllers was performed using mass-loss tests. Both controllers reduced rotor vibration. However, the controller incorporating steady state vibration prediction had increased stability allowing for improved performance during transient vibration periods.

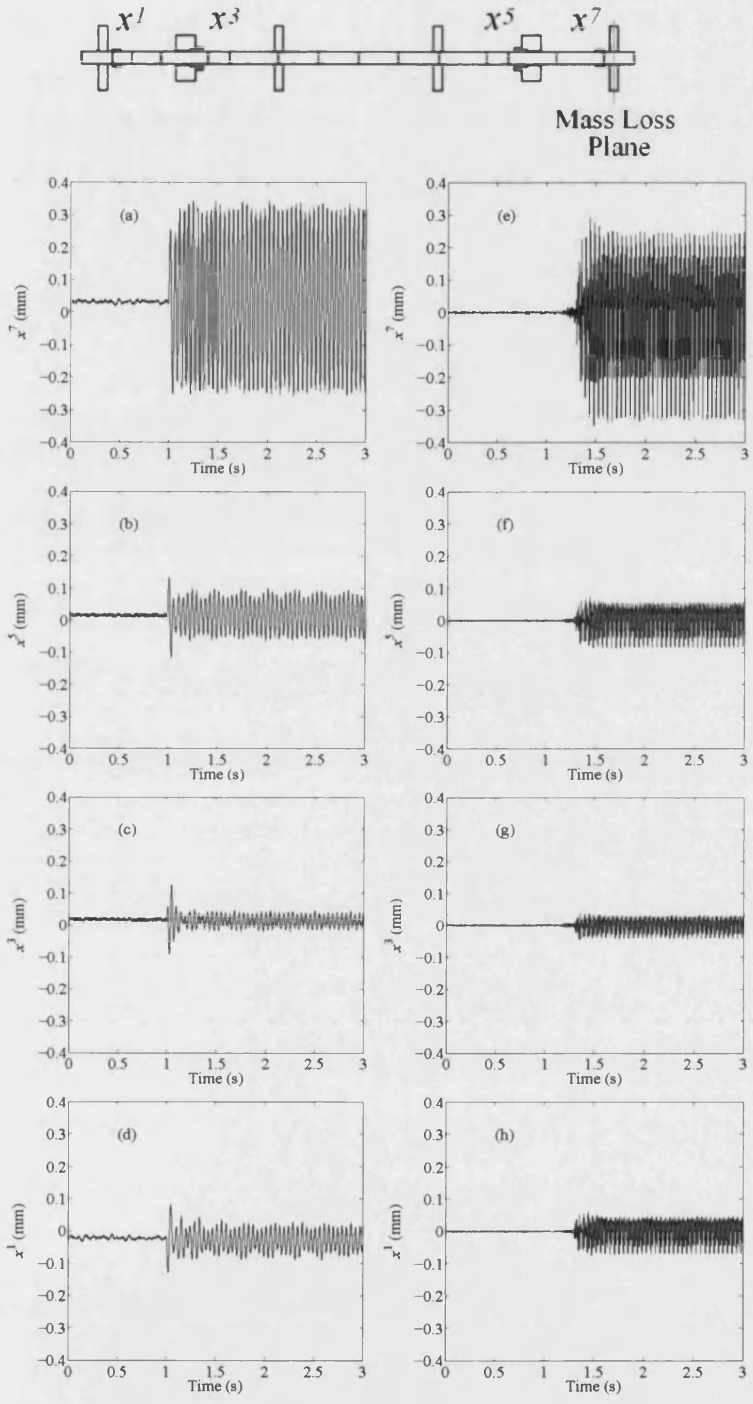

Figure 7.2: Measured step synchronous force response in the x-axis at a rotational speed of 22Hz. (a-d) show measured response and (e-h) show predicted steady state response using the Haar wavelet.

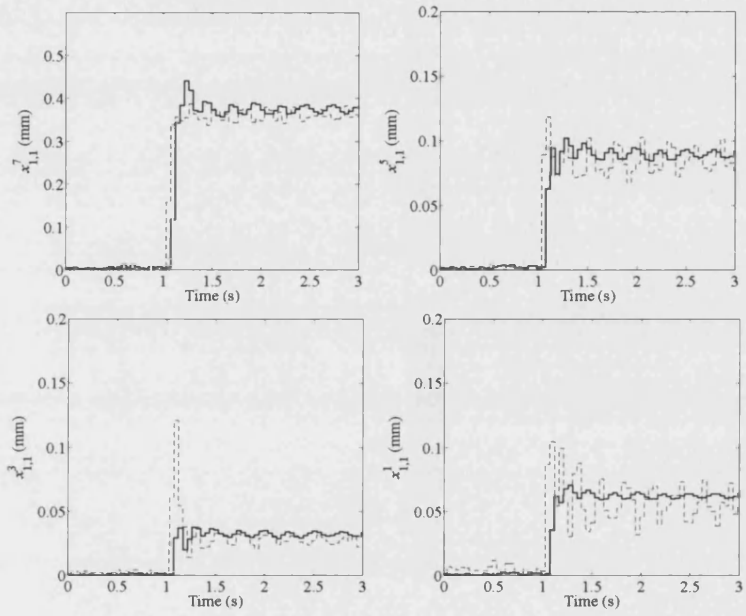

Figure 7.3: Haar wavelet coefficients corresponding to 1× the rotational frequency (dashed line) and predicted steady state wavelet coefficients (solid line) in the x-axis at a rotational speed of 22Hz.

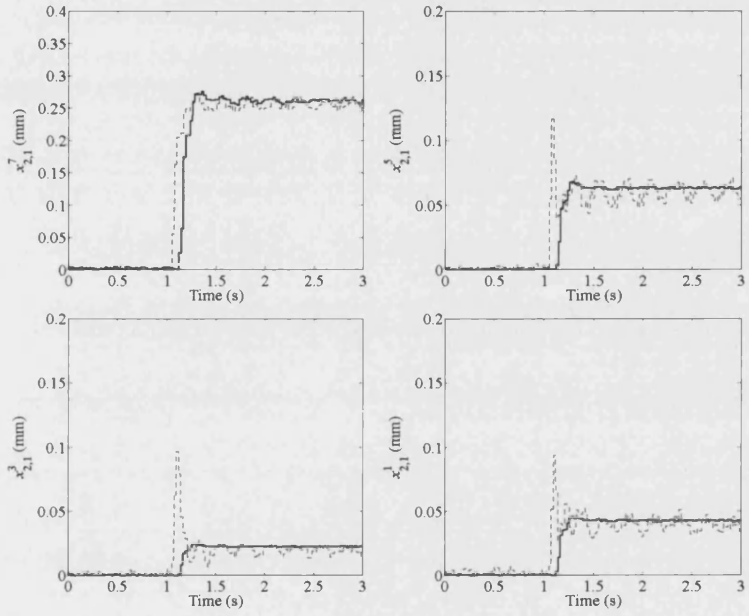

Figure 7.4: Haar wavelet coefficients corresponding to 2× the rotational frequency (dashed line) and predicted steady state wavelet coefficients (solid line) in the x-axis at a rotational speed of 22Hz.

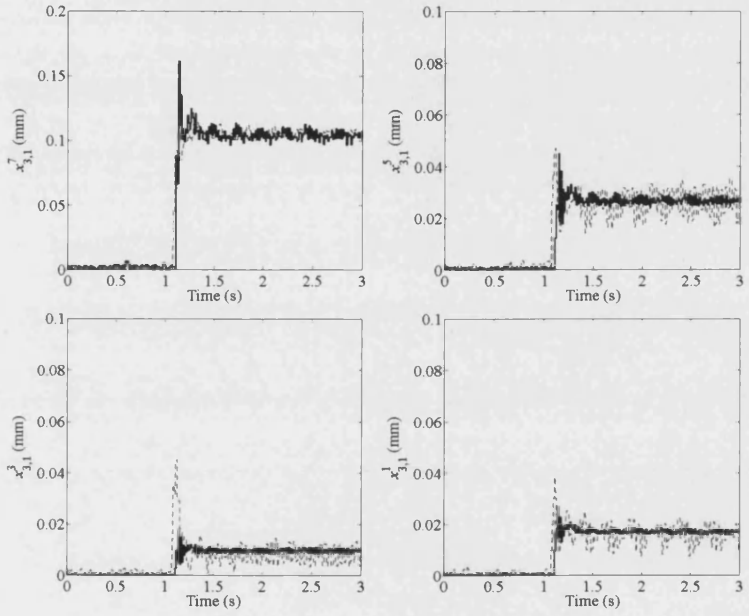

Figure 7.5: Haar wavelet coefficients corresponding to 4× the rotational frequency (dashed line) and predicted steady state wavelet coefficients (solid line) in the x-axis at a rotational speed of 22Hz.

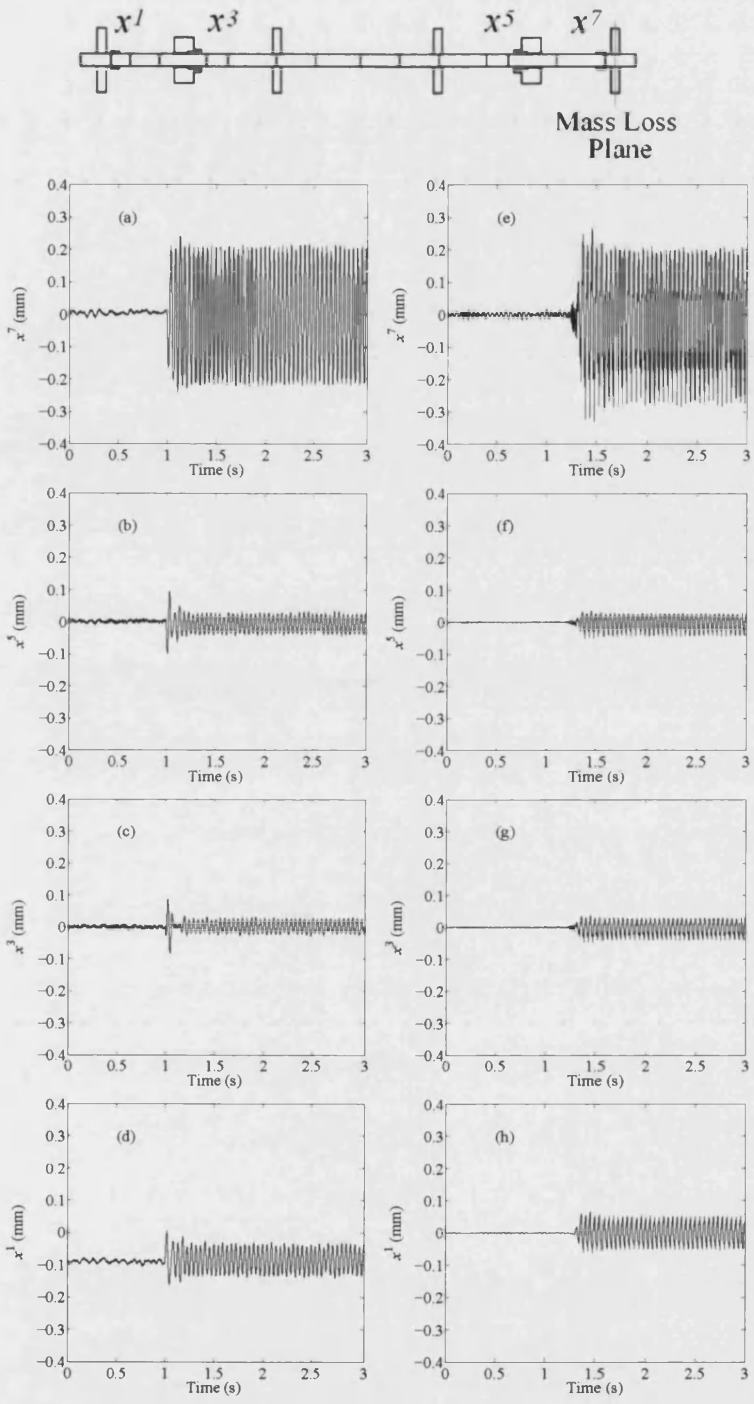

Figure 7.6: Measured step synchronous force response in the x-axis at a rotational speed of 22Hz. (a-d) show measured response and (e-h) show predicted steady state response using Daubechies wavelet 2.

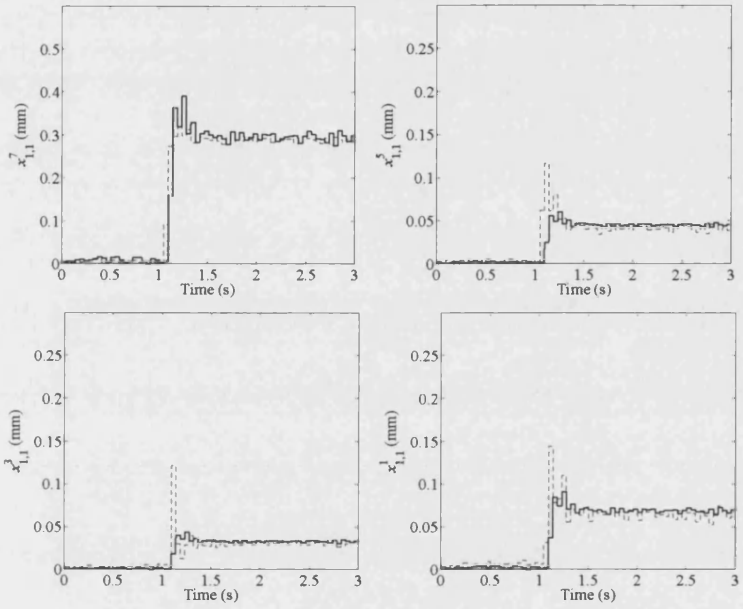

Figure 7.7: Daubechies wavelet 2 coefficients corresponding to 1× the rotational frequency (dashed line) and predicted steady state wavelet coefficients (solid line) in the x-axis at a rotational speed of 22Hz.

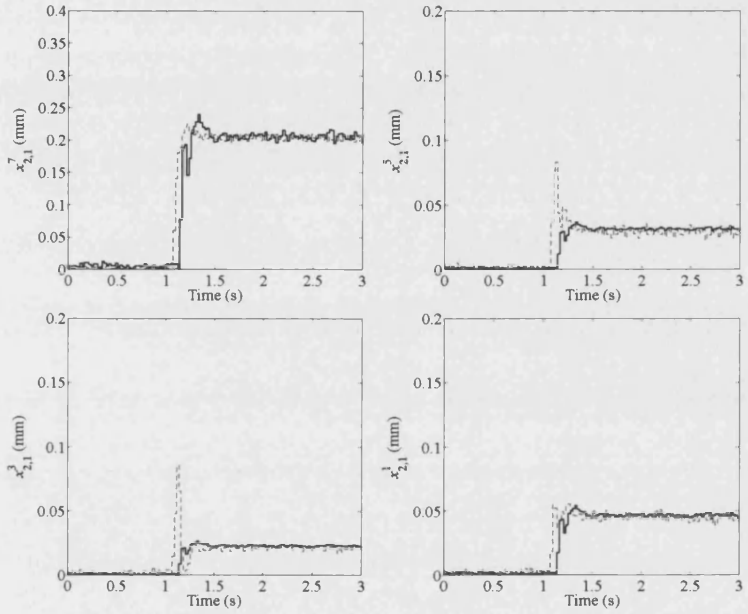

Figure 7.8: Daubechies wavelet 2 coefficients corresponding to 2× the rotational frequency (dashed line) and predicted steady state wavelet coefficients (solid line) in the x-axis at a rotational speed of 22Hz.

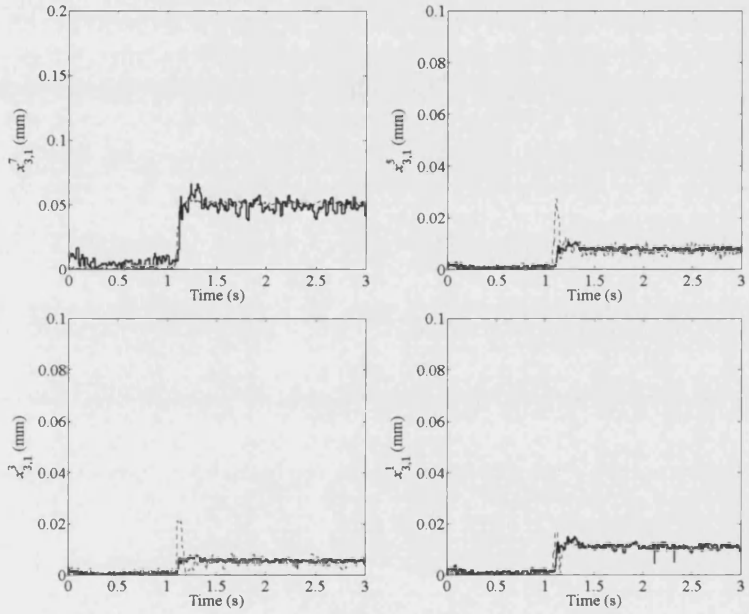

Figure 7.9: Daubechies wavelet 2 coefficients corresponding to 4× the rotational frequency (dashed line) and predicted steady state wavelet coefficients (solid line) in the x-axis at a rotational speed of 22Hz.

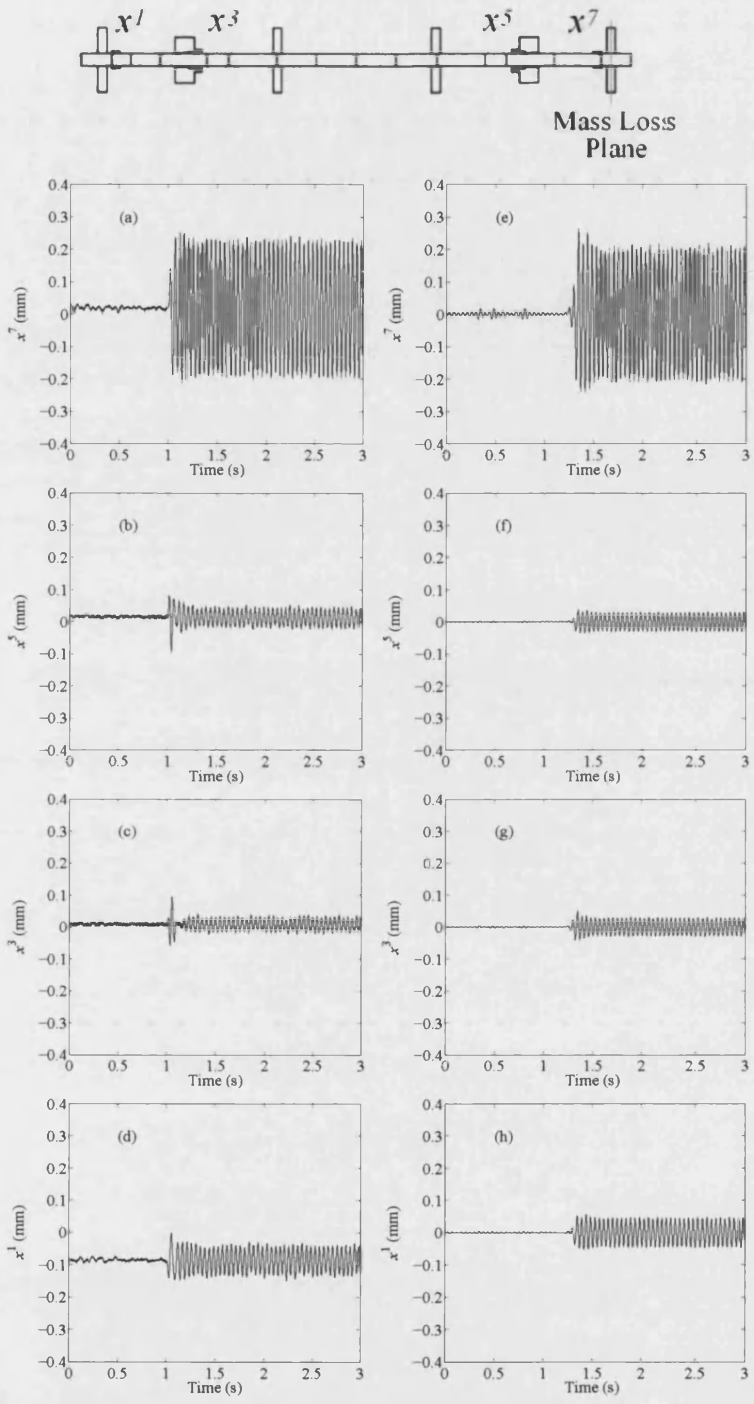

Figure 7.10: Measured step synchronous force response in the x-axis at a rotational speed of 22Hz. (a-d) show measured response and (e-h) show predicted steady state response using Daubechies wavelet 4.

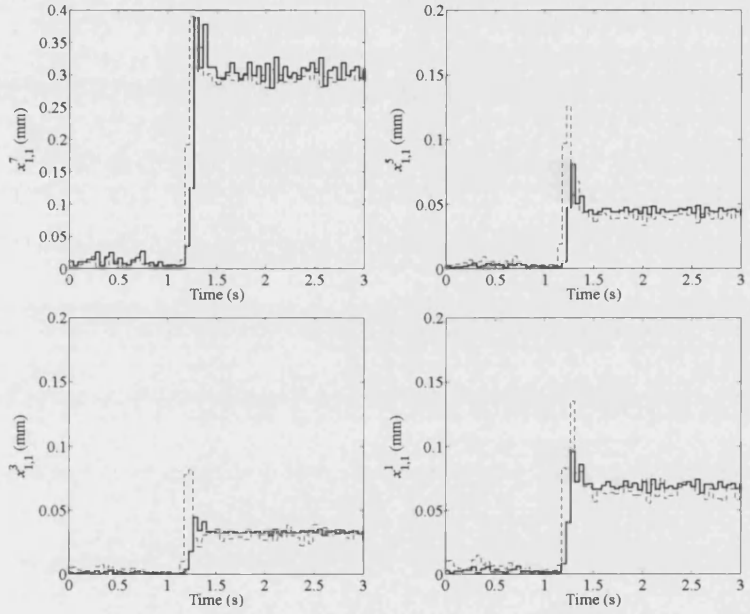

Figure 7.11: Daubechies wavelet 4 coefficients corresponding to 1× the rotational frequency (dashed line) and predicted steady state wavelet coefficients (solid line) in the x-axis at a rotational speed of 22Hz.

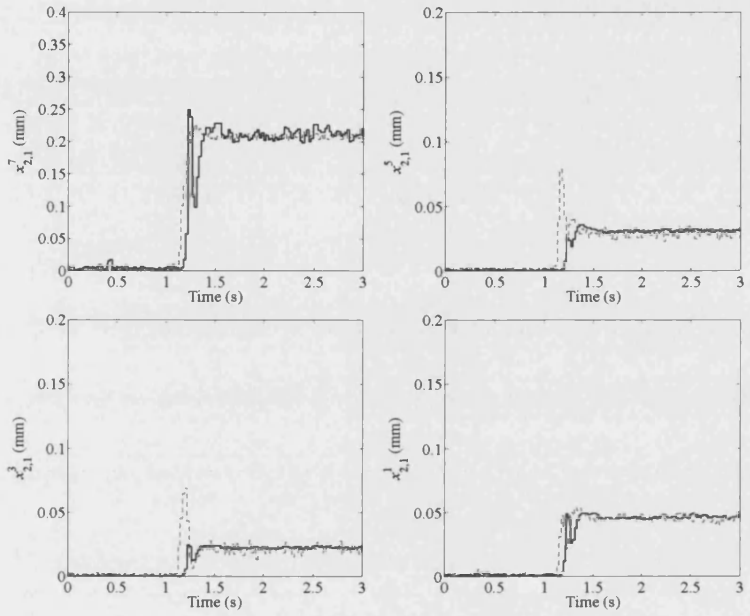

Figure 7.12: Daubechies wavelet 4 coefficients corresponding to 2× the rotational frequency (dashed line) and predicted steady state wavelet coefficients (solid line) in the x-axis at a rotational speed of 22Hz.

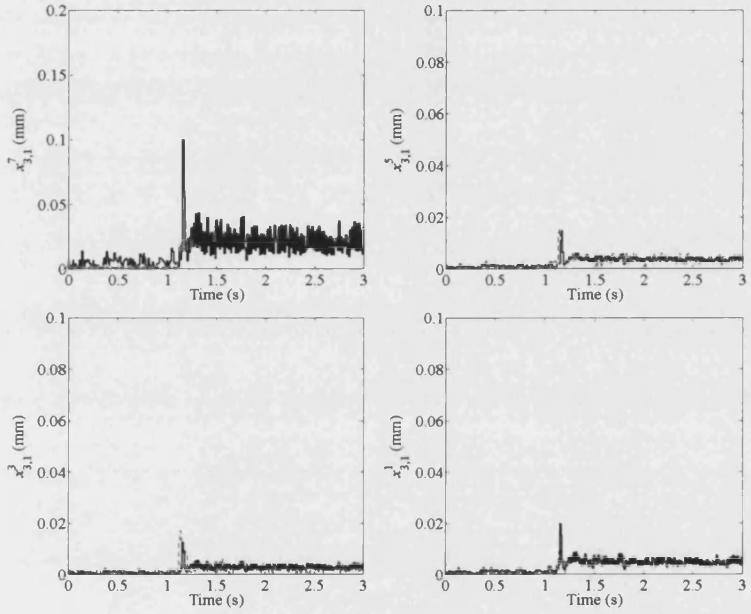

Figure 7.13: Daubechies wavelet 4 coefficients corresponding to 4× the rotational frequency (dashed line) and predicted steady state wavelet coefficients (solid line) in the x-axis at a rotational speed of 22Hz.

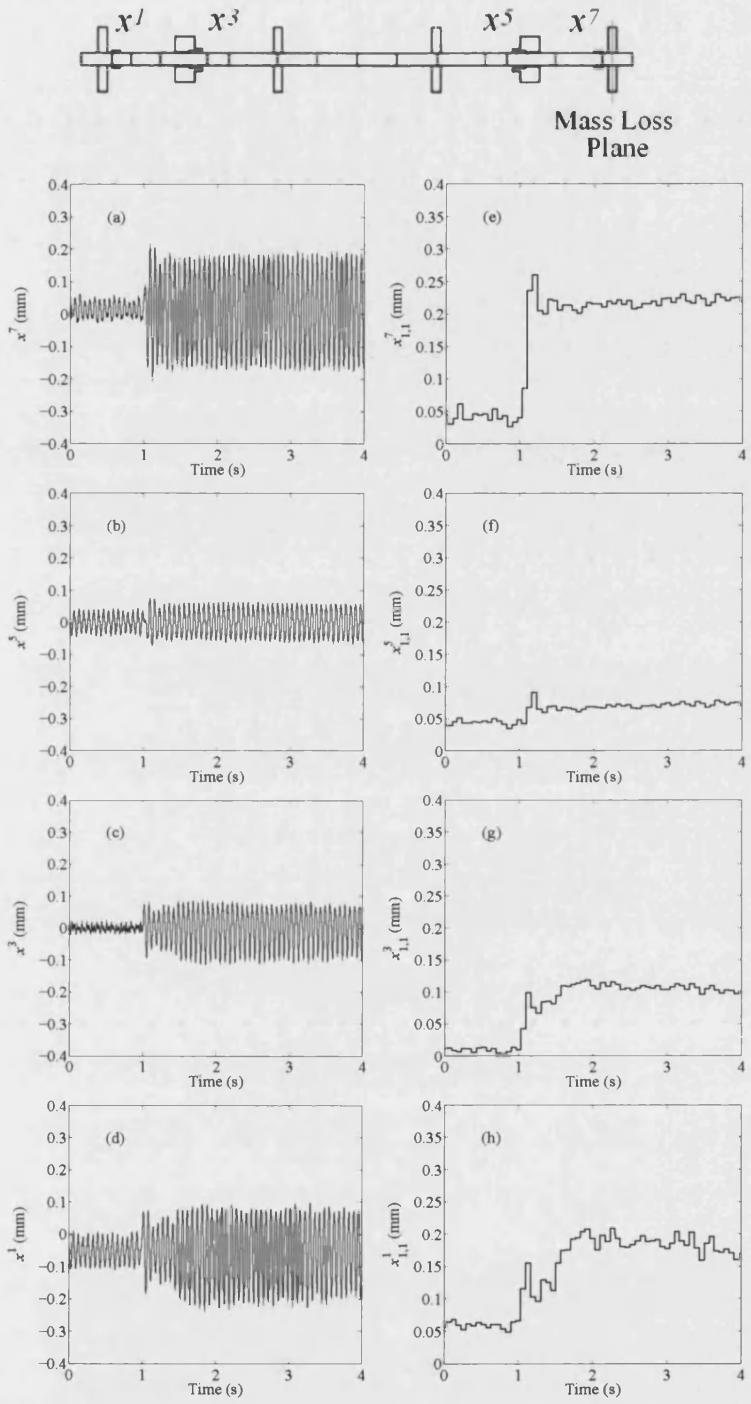

Figure 7.14: Measured mass-loss response in the x-axis at a rotational speed of 15Hz (a-d) for the rotor configured with local PID control only. Wavelet coefficients corresponding to $1\times$ the rotational frequency shown in (e-h).

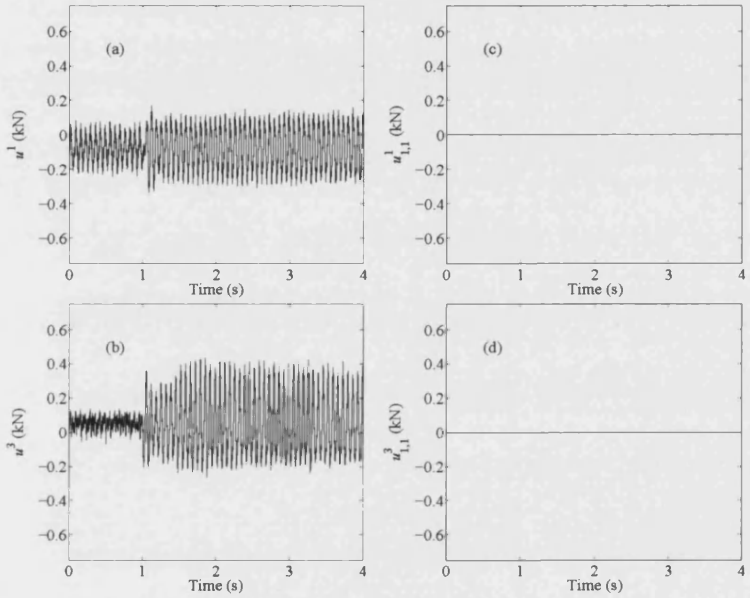

Figure 7.15: (a) and (b) show the total control forces at non driven end and driven end active magnetic bearing at a rotational speed of 15Hz. (c) and (d) show the wavelet coefficient control force.

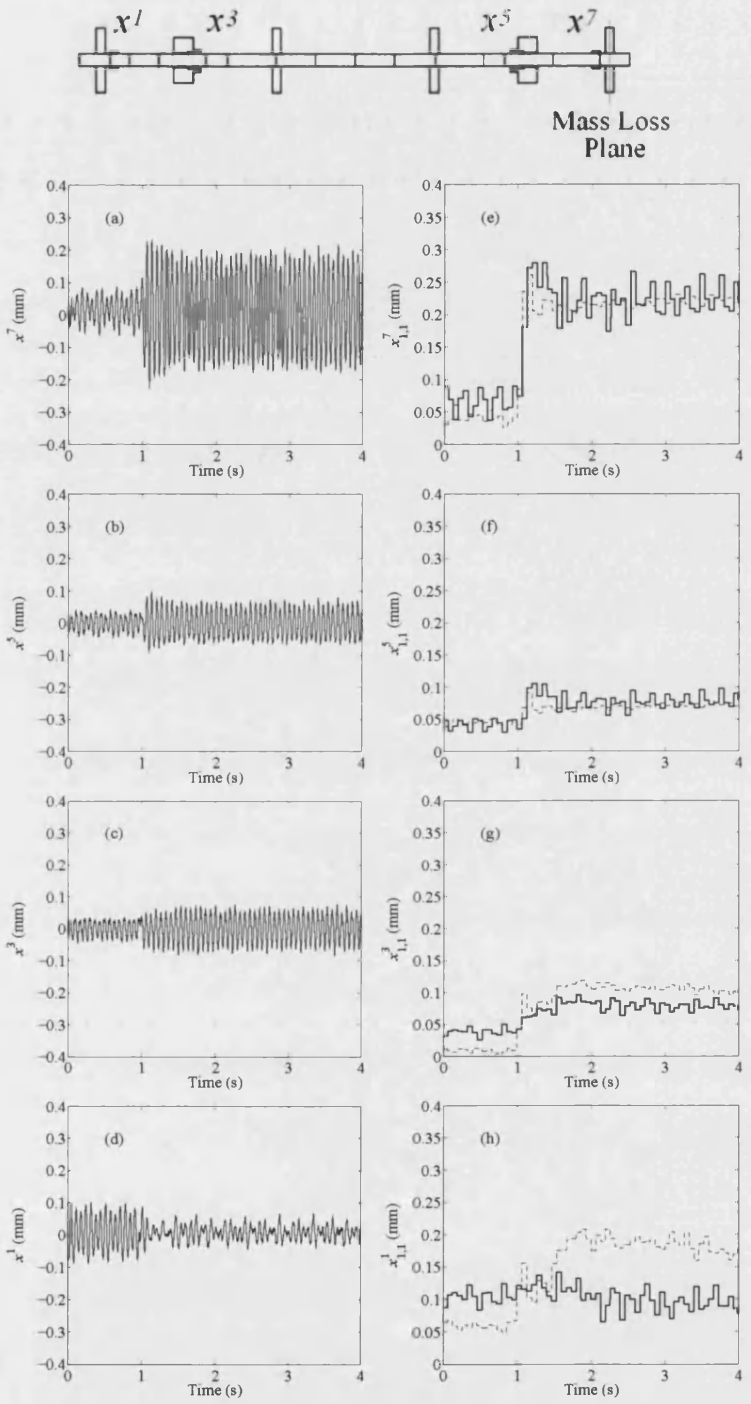

Figure 7.16: Measured mass-loss response in the x-axis at a rotational speed of 15Hz (a-d) for the rotor configured with local PID control and proportional wavelet coefficient feedback. Wavelet coefficients corresponding to $1\times$ the rotational frequency shown in (e-h).

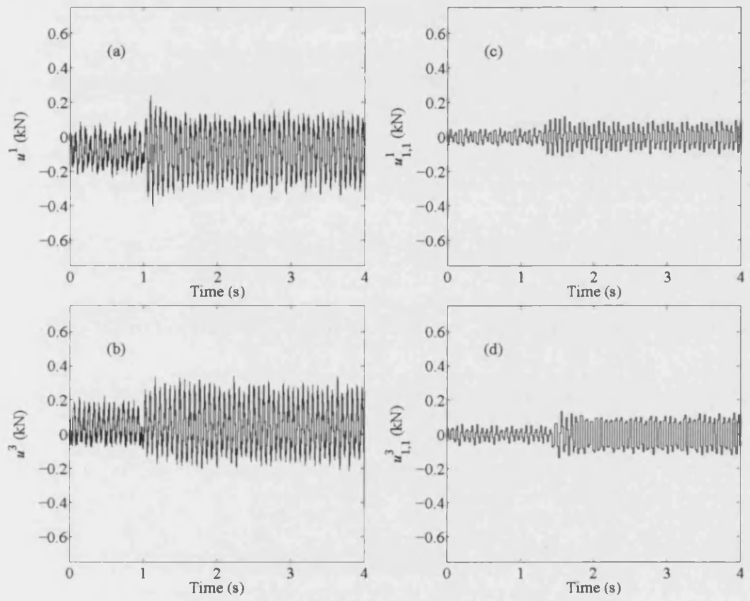

Figure 7.17: (a) and (b) show the total control forces at non driven end and driven end active magnetic bearing at a rotational speed of 15Hz using proportional wavelet coefficient feedback. (c) and (d) show the wavelet coefficient control force.

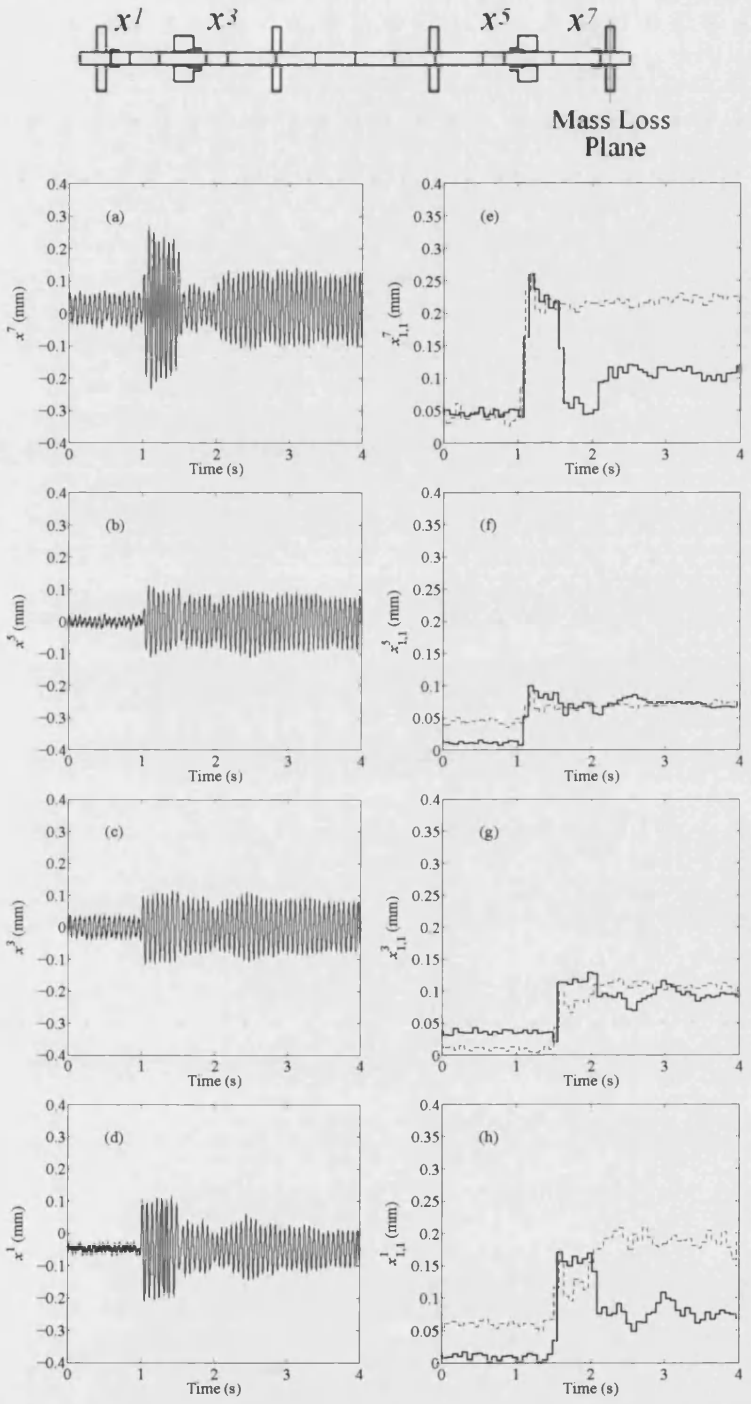

Figure 7.18: Measured mass-loss response in the x-axis at a rotational speed of 15Hz (a-d) for the rotor configured with local PID control and proportional wavelet coefficient feedback with predictive steady state moderation. Wavelet coefficients corresponding to $1\times$ the rotational frequency shown in (e-h).

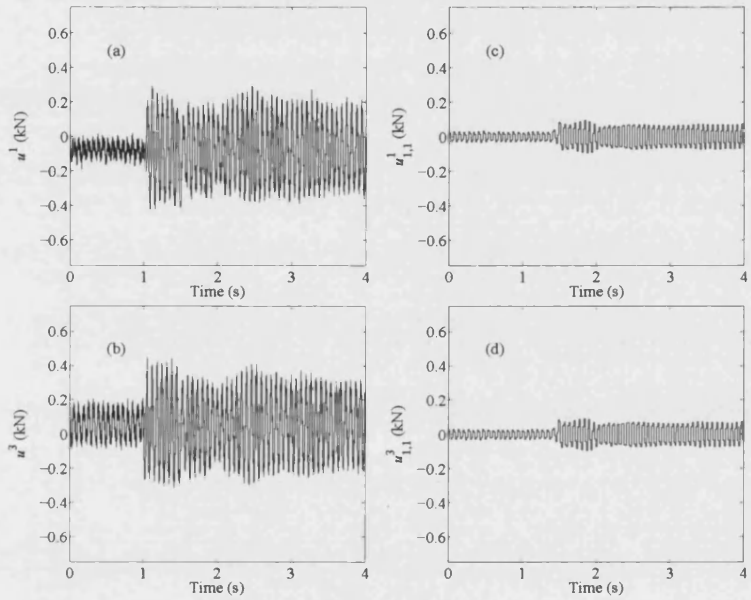

Figure 7.19: (a) and (b) show the total control forces at non driven end and driven end active magnetic bearing at a rotational speed of 15Hz using proportional wavelet coefficient feedback with predictive steady state moderation. (c) and (d) show the wavelet coefficient control force.

Chapter 8

WAVELET TRANSIENT CONTROL

8.1 Introduction

The control of rotor vibration during transient disturbances needs careful consideration. Traditional steady state control algorithms are quick to evaluate the control force, however, they may fail to provide sufficient control forces during transient vibration. Optimally designed control strategies have limited response times due to high system order in the plant model, however, they will ensure system stability. Keogh *et al.* [10] consider a multi-state transient controller evaluated from sampled harmonics. This is essentially a steady state controller embedded with transient system dynamics. The controller is further enhanced through a prescribed transient response dictating the desired system behaviour to step changes in disturbance. However, as already discussed, the transient response may be better represented using wavelet coefficients. This chapter considers a multi-state transient controller acting in the wavelet coefficient domain.

8.2 Discrete Control

Controller design is to be based on a control force evaluated from single or multiple wavelet coefficients (figure 8.1). Assuming that an orthogonal wavelet (e.g. Haar) is used to decompose the measured signals and reconstruct the control signal, each control wavelet coefficient can be evaluated using a different set of control parameters. The closed loop response of a given wavelet coefficient can be evaluated by replacing $\mathbf{F}_{a,b}(z)$ by $\mathbf{F}_{a,b}(z) + \mathbf{B}_u\mathbf{U}_{a,b}(z)$ in equation (6.18). The control force

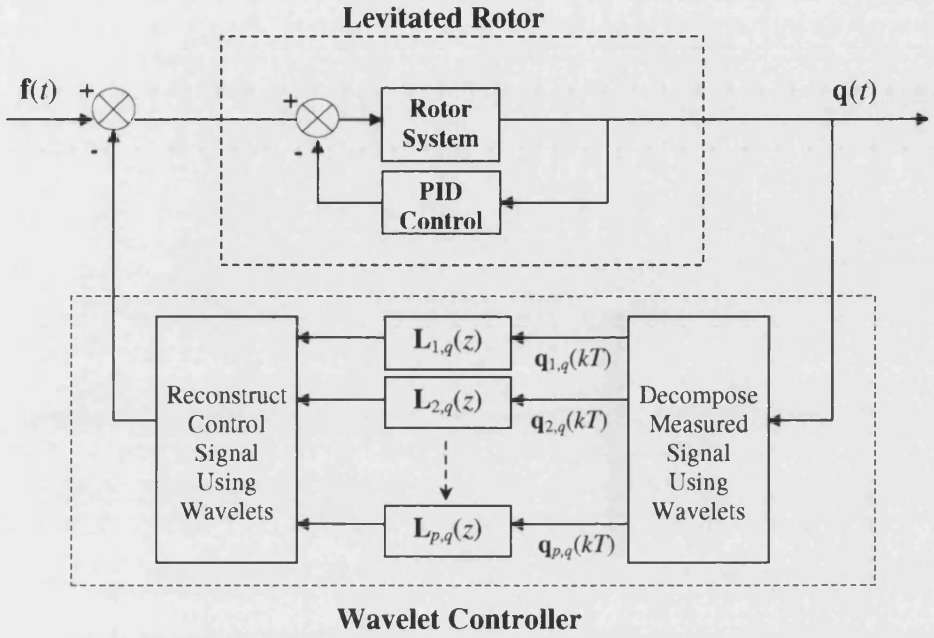

Figure 8.1: Block diagram showing feedback control structure in the wavelet coefficient domain.

wavelet coefficients, $\mathbf{U}_{p,q}(z)$, are now specified by

$$\mathbf{U}_{p,q}(z) = -\mathbf{L}_{p,q}(z)\mathbf{Q}^{(m)}_{p,q}(z) \tag{8.1}$$

where $\mathbf{L}_{p,q}(z)$ represents the controller operating on wavelet coefficients at level p. The matrix $\mathbf{B}^{(m)}$ is used to extract the measurement states from the system state vector as $\mathbf{Q}^{(m)}_{p,q}(z) = \mathbf{B}^{(m)}\mathbf{Q}_{p,q}(z)$. The closed loop response of the system satisfies

$$\left(\mathbf{I} - \mathbf{G}_{p,q,p,q}(z)\mathbf{B}_u\mathbf{L}_{p,q}(z)\right)\mathbf{Q}^{(m)}_{p,q}(z) = \mathbf{G}^0_{p,q}(z)\mathbf{F}^0(z) - \sum_{a=0}^{\infty}\sum_{b=0}^{2^a-1}\mathbf{G}_{p,q,a,b}(z)\mathbf{F}_{a,b}(z) \tag{8.2}$$

The controller objective is to minimize the transient response of the measured states at a given level of wavelet decomposition, p. The controller is also required to provide optimal steady state performance. In order to achieve this the controller is designed around a desired closed loop transient response due to a step change in the wavelet

coefficients of an input disturbance:

$$\begin{aligned} \textit{Step input}: \quad & \mathbf{F}_{p,q}(z) = \frac{1}{z-1}\mathbf{B}_u \\ \textit{Desired output}: \quad & \mathbf{Q}_{p,q}^{(m)}(z) = \alpha_{p,q}(z)\mathbf{G}_{p,q,p,q}(z)\mathbf{B}_u \end{aligned} \tag{8.3}$$

where $\alpha_{p,q}(z)$ defines the prescribed transient response of a measurement axis. In a multi output system $\alpha_{p,q}(z)$ can be expressed as an $n \times n$ matrix. Prescribed transient responses for each measurement axis can be specified using the diagonal elements. Combining equations (8.1), (8.2) and (8.3) the least squares solution of equation (8.2) is:

$$\begin{aligned} \mathbf{L}_{p,q}(z) =& \mathbf{G}_{p,q,p,q}(z)\mathbf{B}_u)^* \left[\alpha_{p,q}(z)\mathbf{I}\right]^{-1} \frac{1}{z-1} \\ & - (\mathbf{G}_{p,q,p,q}(z)\mathbf{B}_u)^* \left[\alpha_{p,q}(z)\mathbf{I}\right] (\mathbf{G}_{p,q,p,q}(z)\mathbf{B}_u)(\mathbf{G}_{p,q,p,q}(z)\mathbf{B}_u)^* \left[\alpha_{p,q}(z)\mathbf{I}\right]^{-1} \end{aligned} \tag{8.4}$$

For a controller with a specified transient response given by equation (8.3) then

$$\mathbf{L}_{p,q}(z) = (\mathbf{G}_{p,q,p,q}(z)\mathbf{B}_u)^* \left(\frac{1}{\alpha_{p,q}(z)(z-1)} - 1\right) \tag{8.5}$$

where $(.)^*$ denotes the pseudo-matrix inverse.

It is noted that closed loop instability could result from the application of the controller specified in equation (8.5), for example, due to residuals arising from the least squares solution. An assessment of closed loop stability could be made at this stage if a system modeling approach is adopted. A controller could also be derived from a model based on system identification and assessed using on-line testing to determine acceptable operating boundaries. The latter approach overcomes certain issues relating to modelling uncertainty and for this reason is selected.

8.3 Variations of Transient Response Characteristic

The control action is dictated by the specified transient response characteristic. Exponential decay of the wavelet coefficients can be achieved by setting $\alpha_{p,q}(z)$ to

$$\alpha_{p,q}(z) = \frac{w_{p,q}}{z - v_{p,q}} \tag{8.6}$$

where $0 \leq w_{p,q} < 1$ and $0 \leq v_{p,q} < 1$. However, any other decay characteristic can also be specified. Expressing the desired transient response characteristic as a series

$$\alpha_{p,q}(z) = \sum_{k=1}^{\infty} \frac{c_k}{z^k} \tag{8.7}$$

then c_k is the desired transient response after the k^{th} time step.

8.4 Controller Stability

From equation (8.2), the system will demonstrate closed loop stability provided provided that all the zeros present are within the unit circle, [74]. Combining equation (8.5) with the left hand side of equation (8.2) so that

$$\mathbf{I} - \mathbf{G}_{p,q,p,q}(z)\mathbf{B}_u\mathbf{L}_{p,q}(z) = \mathbf{I} - \mathbf{G}_{p,q,p,q}(z)\mathbf{B}_u(\mathbf{G}_{p,q,p,q}(z)\mathbf{B}_u)^* \left(\frac{1}{\alpha_{p,q}(z)(z-1)} - 1\right) \tag{8.8}$$

giving

$$\mathbf{I} - \mathbf{G}_{p,q,p,q}(z)\mathbf{B}_u\mathbf{L}_{p,q}(z) = \mathbf{I} - \mathbf{I}\left(\frac{1}{\alpha_{p,q}(z)(z-1)} - 1\right) \tag{8.9}$$

The right hand side of equation (8.9) has two terms equal to either $1/\alpha_{p,q}(z)(z-1)$ or 1. For the closed loop system to be stable any zeros in equation (8.2) must lie within the unit circle. Therefore, any singularities in the prescribed transient response, $\alpha_{p,q}(z)\mathbf{I}$, must also lie within the unit circle. Other considerations will also affect the choice of $\alpha_{p,q}(z)$. These include the performance capabilities of the magnetic bearings, rotor clearances, modelling errors and control evaluation time. The latter is of significant importance when considering transient vibrations. It has already been noted that instabilities could arise from the controller due to residuals and discretization errors in the system modelling. Implementation of the control algorithm will require the wavelet coefficients to be evaluated from measured signals, this is then followed by the evaluation of the control wavelet coefficient. There will therefore be a time delay associated with the evaluation of the control force. In the case of steady state vibration this is a less significant problem since the wavelet coefficients will remain constant. However, for a rapidly varying transient response the control coefficient evaluated to cancel a wavelet coefficient may be ineffective after a delay of several periods. Incorporating the delays into the controller gives

$$\mathbf{L}_{p,q}(z) = \frac{1}{z^i}(\mathbf{G}_{p,q,p,q}(z)\mathbf{B}_u)^* \left(\frac{1}{\alpha_{p,q}(z)(z-1)} - 1\right) \tag{8.10}$$

where i represents the number of delay periods. Equation (8.9) can be modified and rearranged to incorporate evaluation delays as

$$\mathbf{I} - \mathbf{G}_{p,q,p,q}(z)\mathbf{B}_u\mathbf{L}_{p,q}(z) = \mathbf{I} - \mathbf{I}\left(\frac{1 - \alpha_{p,q}(z)(z-1)}{\alpha_{p,q}(z)z^i(z-1)}\right) \tag{8.11}$$

The stability of the system due to errors in the controller plant model is an important consideration. Figure 8.2 shows a schematic block diagram of the system with

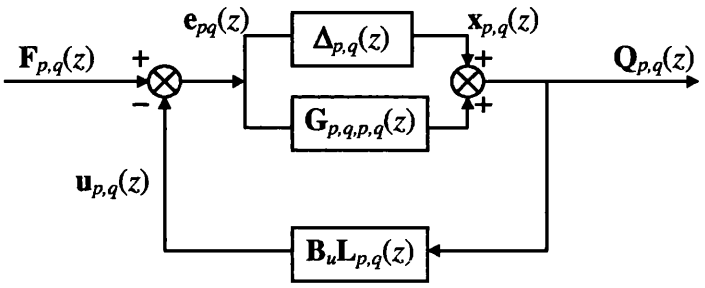

Figure 8.2: Schematic block diagram of system with additive error dynamics.

additional additive errors in the plant model given by $\boldsymbol{\Delta}_{p,q}(z)$. The transfer function, $\mathbf{H}_{p,q}(z)$, from $\mathbf{x}_{p,q}(z)$ to $\mathbf{e}_{p,q}(z)$ can be identified as

$$\mathbf{H}_{p,q}(z) = -\mathbf{B}_u\mathbf{L}_{p,q}(z)\left(\mathbf{I} + \mathbf{G}_{p,q,p,q}(z)\mathbf{B}_u\mathbf{L}_{p,q}(z)\right)^{-1} \tag{8.12}$$

giving

$$\mathbf{H}_{p,q}(z) = -\mathbf{B}_u\frac{1}{z^i}(\mathbf{G}_{p,q,p,q}(z)\mathbf{B}_u)^*\left(\frac{1}{\alpha_{p,q}(z)(z-1)} - 1\right)\left[\mathbf{I} - \mathbf{I}\left(\frac{1-\alpha_{p,q}(z)(z-1)}{\alpha_{p,q}(z)z^i(z-1)}\right)\right]^{-1} \tag{8.13}$$

Combining the target transient response terms, $\mathbf{H}_{p,q}(z)$ can be expressed as

$$\mathbf{H}_{p,q}(z) = -\mathbf{B}_u(\mathbf{G}_{p,q,p,q}(z)\mathbf{B}_u)^*\gamma(\alpha_{p,q}(z)) \tag{8.14}$$

where

$$\gamma(\alpha_{p,q}(z)) = \frac{1-\alpha_{p,q}(z)(z-1)}{1+\alpha_{p,q}(z)(z-1)(z^i-1)} \tag{8.15}$$

Closed loop stability of the system can be ensured provided that

$$(\mathbf{G}_{p,q,p,q}(z)\mathbf{B}_u)^*\gamma(\alpha_{p,q}(z)) \leq 1 \tag{8.16}$$

Stability limits for the controller are shown in figure 8.3. The effect of system delays is evident showing controller performance to be limited by longer evaluation times.

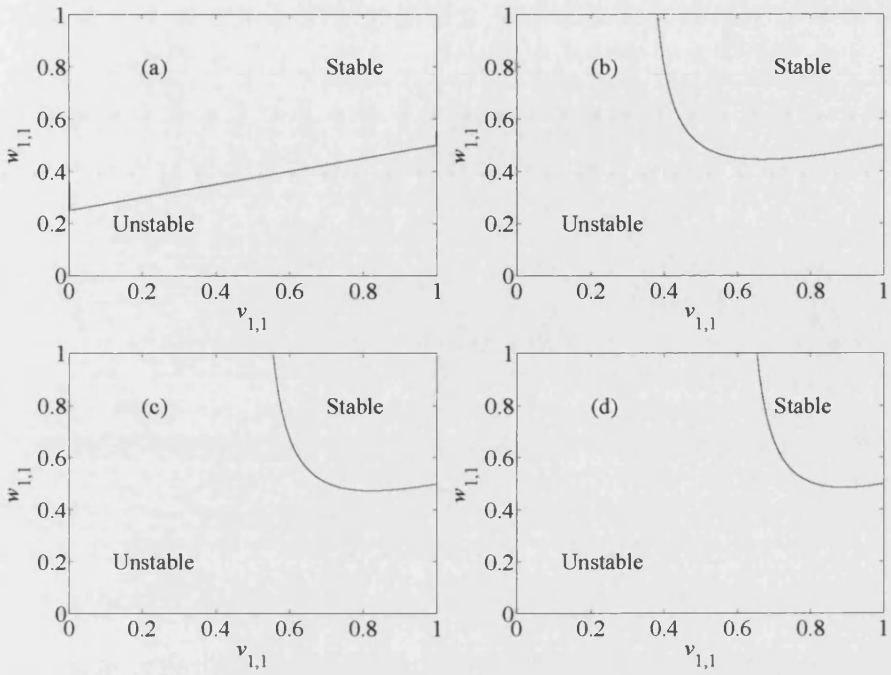

Figure 8.3: System stability regions for an exponential target transient response. (a) one cycle delay. (b) two cycle delay. (c) three cycle delay. (d) four cycle delay.

8.5 Experimental Validation

8.5.1 Experimental Procedure and Results

The experimentally derived parameters to be presented are specified in Table 7.1. The system was identified from measurement of the wavelet coefficients with a pseudo-frequency matching the rotational frequency. Control wavelet coefficients were set at the same level such that $a = p = 1$. Figure 6.3(a) shows the measured response, corresponding to a pseudo-frequency of 11Hz, at sensor 1 due to a step wavelet disturbance applied through control axis 1. The inverse transfer function has been identified and truncated after 10 and 5 time steps (figures 6.3(b) and 6.3(c). The measured response corresponding to a pseudo-frequency of 18Hz is shown in figure 6.4. The 5^{th} order version was selected to allow for real time controller implementation. The controller evaluation time required there to be a 2 cycle delay in control action. Variation of the parameters $w_{1,1}$ and $v_{1,1}$ was used to create controllers with different target transient responses. From observations of the rotor displacements controllers were classified unacceptable if the vibration exceeded a

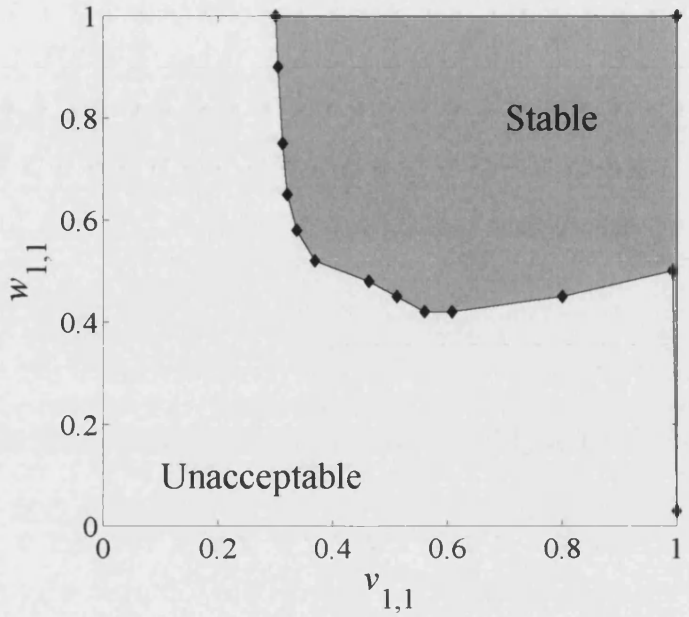

Figure 8.4: Acceptable performance diagram for a prescribed transient exponential decay at a rotational speed of 11Hz.

specified limit of 0.5mm in any control plane. This was repeated for various combinations of $w_{1,1}$ and $v_{1,1}$ to identify a region of controller acceptability. It is noted that this is not a measure of controller stability since stable operating states may exceed the specified limit. However, physical limitations, such as the magnetic bearings performance and auxiliary bearing clearance, must also be accounted for. A systematic experimental search of the stability limit yielded the boundary shown in figure 8.4 for a controller designed to operate at 11Hz. The same procedure was used to identify a limit on the maximum linear decay rate per time step for controllers operating at 11Hz. This was found to be 0.31 per time step.

8.5.2 Step Synchronous Force Tests

Step synchronous force tests were performed by applying a sudden change in synchronous disturbance force, 150N, through the non-driven end active magnetic bearing. Operating speeds of 11Hz, 18Hz and 29Hz were chosen to coincide with critical operating speeds of the rotor. The wavelet coefficient controller was derived from a target transient response with $w_{1,1} = 0.75$ and $v_{1,1} = 0.75$. Figure 8.5 shows the rotor response in the x-axis at an operating speed of 11Hz. Corresponding wavelet coefficients at each time step are also shown. The controller is seen to suppress the

transient response of the wavelet coefficients in a finite settling time. The corresponding demand control forces through the x-axis are shown in figure 8.6. The rotor responses at 18Hz and 29 Hz are shown in figures 8.7 and 8.9. The corresponding demand control forces through the x-axis are shown in figures 8.8 and 8.10

8.5.3 Mass-Loss Tests

Mass-loss experiments were performed at the non-driven end disk (figure 2.1) at the first 2 critical speeds, 11Hz and 18Hz. Mass-loss was initiated by a blade mechanism using a tied on mass from an initial indeterminate state of unbalance. The effective mass loss eccentricity was 430gcm. The wavelet coefficient controller was configured to give an exponential decay as prescribed by equation (8.6) where $w_{1,1} = 0.75$ and $v_{1,1} = 0.75$. Figure 8.11 shows the mass loss response of the rotor at a rotational frequency of 11Hz in the x-axis for the PID controlled system with and without the additional transient wavelet controller. The corresponding wavelet coefficient is presented at each sampled step for the transient wavelet controlled case. The controller is shown to suppress the transient responses within a finite settling time. This is further seen in the reduction in the wavelet coefficients in the rotor response. Figure 8.12 shows both the wavelet control force and the total control force at both magnetic bearings. The wavelet control force due to the Haar wavelet is seen to compensate for the disturbance and settles into a steady state. The mass loss response at a rotational frequency of 18Hz is presented in figure 8.13 for $w_{1,1} = v_{1,1} = 0.75$. The corresponding PID and wavelet demand control forces are shown in figure 8.14. Variation of the prescribed transient response is shown in figures 8.15, 8.16 and 8.17 for $w_{1,1} = v_{1,1} = 0.65$ (faster exponential decay), $w_{1,1} = v_{1,1} = 0.9$ (slower exponential decay), and a linear decay rate of 0.2 per time step, respectively. The rotor response due to a prescribed fast exponentially decay is seen to flutter due to over compensation of the disturbance by the controller. The prescribed slow exponential response is seen to gradually reduce the rotor vibration, however, performance is limited by the small controller gain ($w_{1,1}$) and slow prescribed decay rate ($v_{1,1}$). The prescribed linear controller is effective and demonstrates a linear reduction in the rotor vibration. These results demonstrate how the transient rotor response can be directly influenced by the selected target setting of equation (8.3). Moreover, the wavelet coefficient variations provide strong correlations to the boundary envelopes of the directly measured rotor vibratory signals. The potential for transient control in the wavelet coefficient domain has thus been shown to be highly positive.

Limitations in the level of possible transient control relate to stability issues in the closed loop, which are caused primarily by the control evaluation delays. For ultra high speed rotors, processor limitations could result in increased delays and hence degrade closed loop stability. Measurement noise could also contribute to reduced controller performance and stability margins. However, the on-line testing procedure presented could, in principle, be used to determine a more conservative acceptable

performance diagram for the controller.

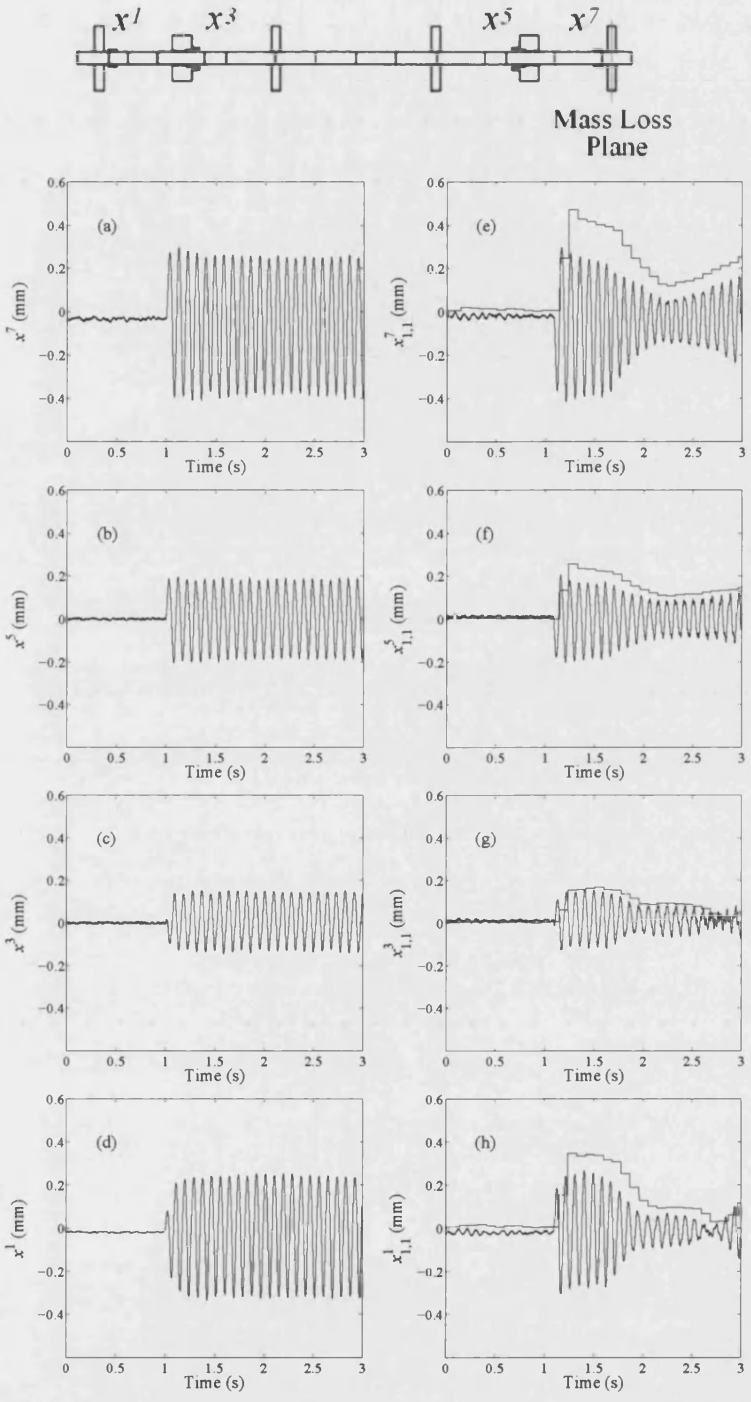

Figure 8.5: Measured step synchronous force response in the x-axis at a rotational speed of 11Hz. (a-d) show uncontrolled response and (e-h) show controlled response and wavelet coefficients.

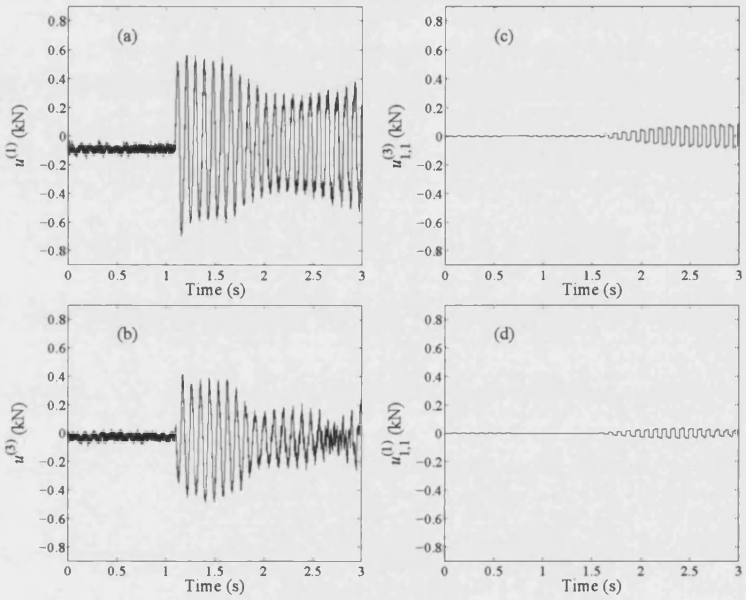

Figure 8.6: (a) and (b) show the total control forces at non driven end and driven end active magnetic bearings at a rotational speed of 11Hz. (c) and (d) show the wavelet coefficient control force.

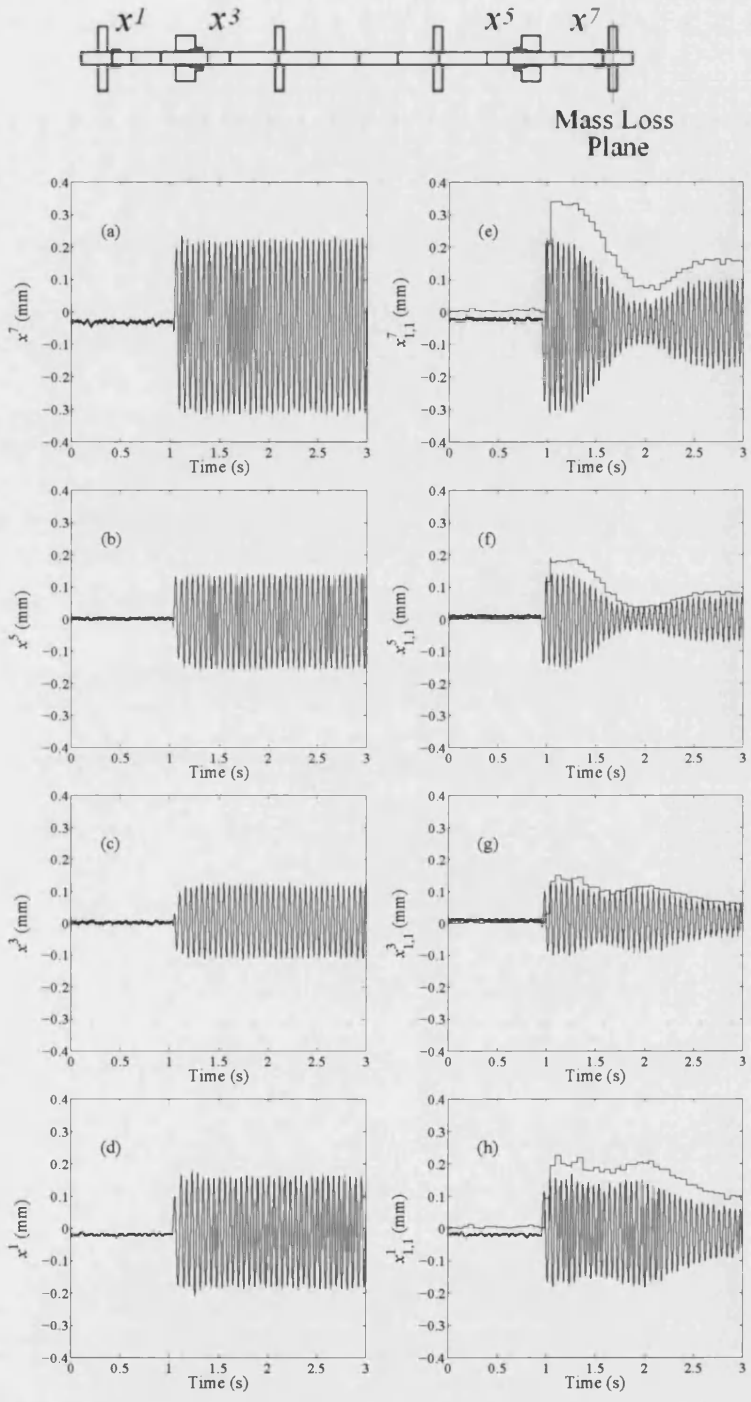

Figure 8.7: Measured step synchronous force response in the x-axis at a rotational speed of 18Hz. (a-d) show uncontrolled response and (e-h) show controlled response and wavelet coefficients.

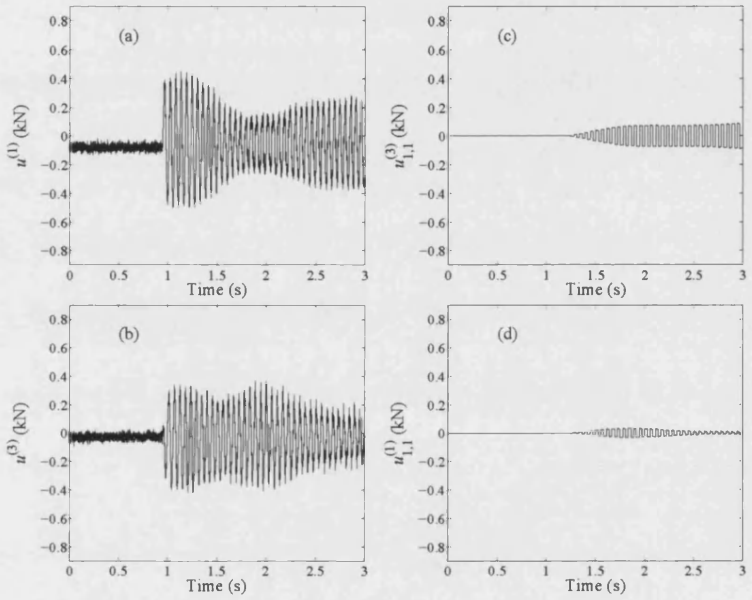

Figure 8.8: (a) and (b) show the total control forces at non driven end and driven end active magnetic bearings at a rotational speed of 18Hz. (c) and (d) show the wavelet coefficient control force.

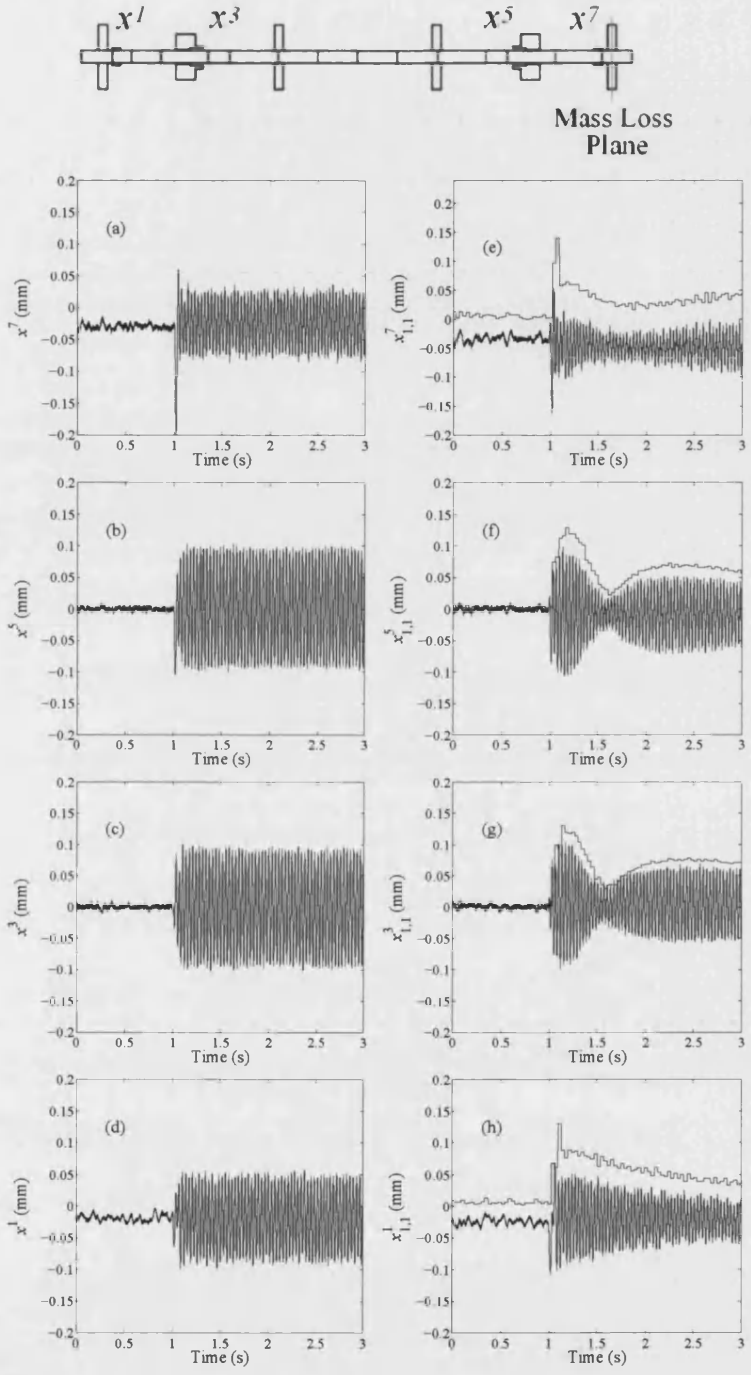

Figure 8.9: Measured step synchronous force response in the x-axis at a rotational speed of 29Hz. (a-d) show uncontrolled response and (e-h) show controlled response and wavelet coefficients.

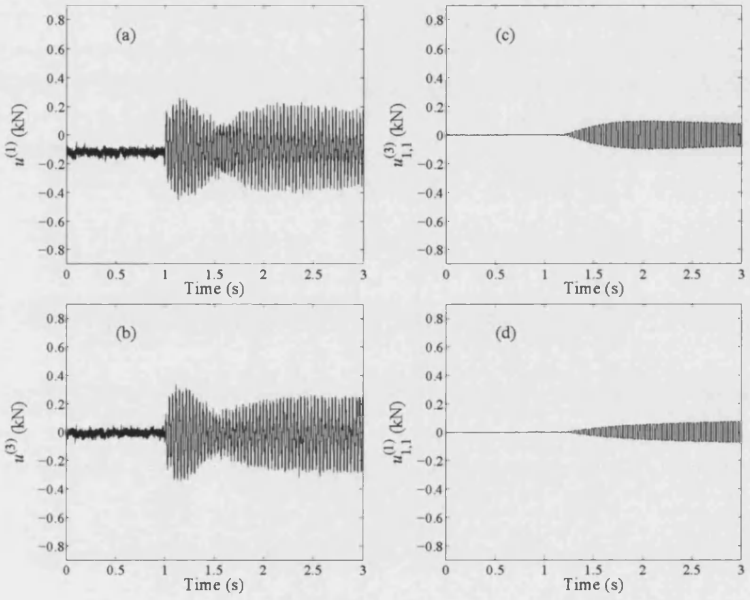

Figure 8.10: (a) and (b) show the total control forces at non driven end and driven end active magnetic bearings at a rotational speed of 29Hz. (c) and (d) show the wavelet coefficient control force.

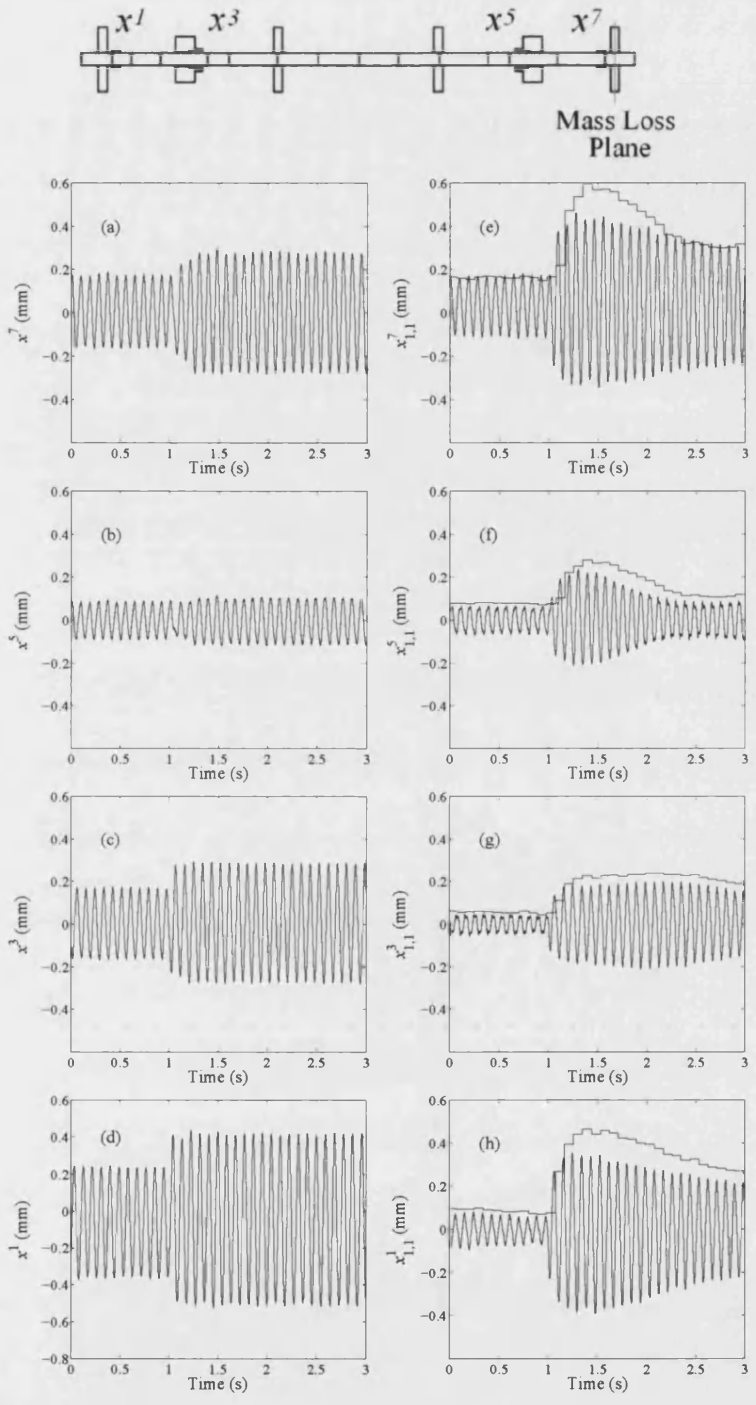

Figure 8.11: Measured mass-loss response in the x-axis at a rotational speed of 11Hz. (a-d) show uncontrolled response and (e-h) show controlled response and wavelet coefficients.

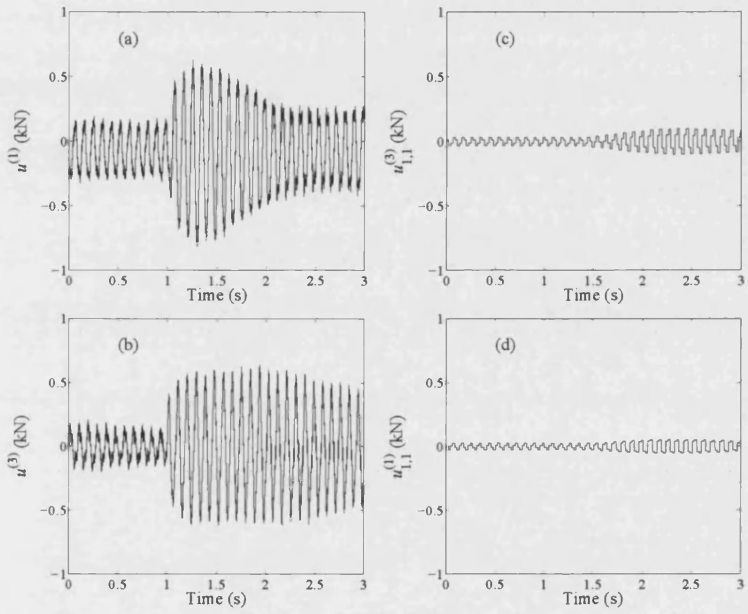

Figure 8.12: (a) and (b) show the total control forces at non driven end and driven end active magnetic bearings at a rotational speed of 11Hz. (c) and (d) show the wavelet coefficient control force.

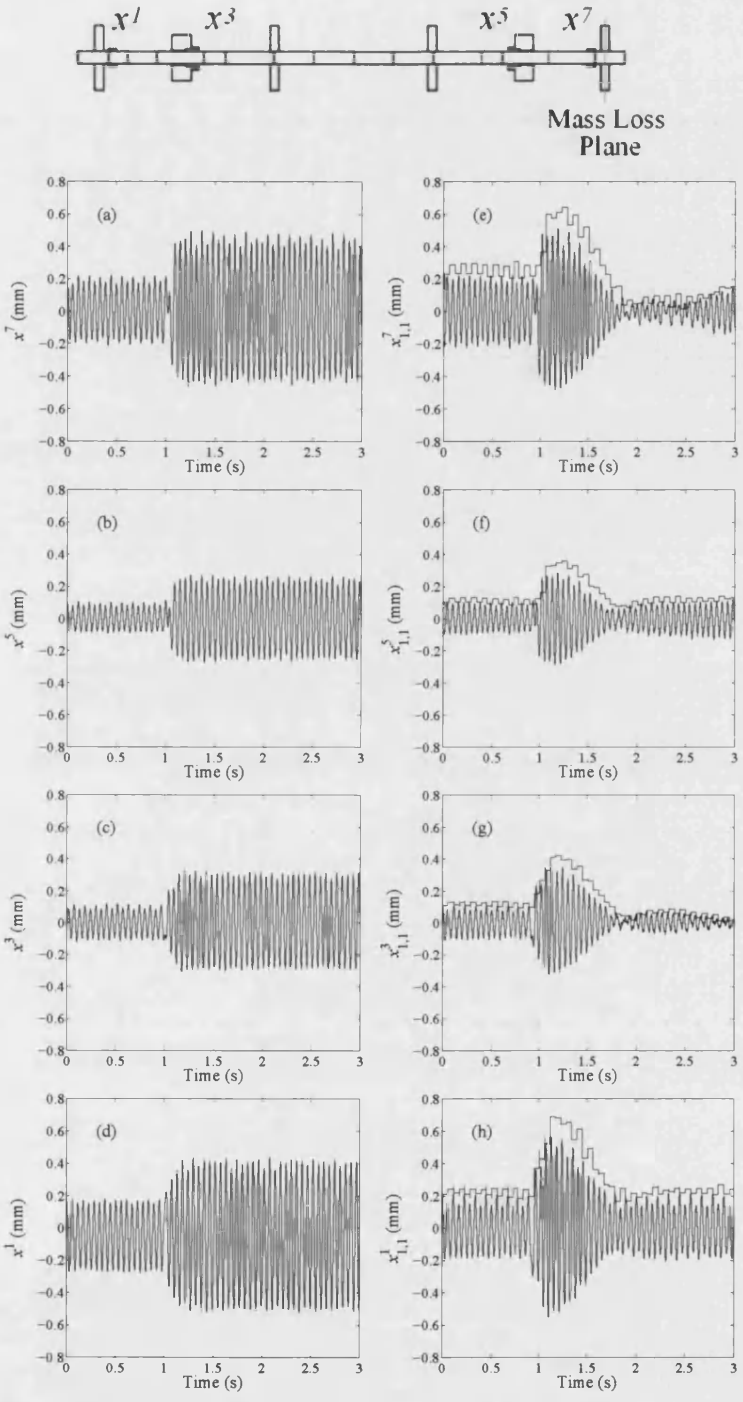

Figure 8.13: Measured mass-loss response in the x-axis at a rotational speed of 18Hz. (a-d) show uncontrolled response and (e-h) show controlled response and wavelet coefficients.

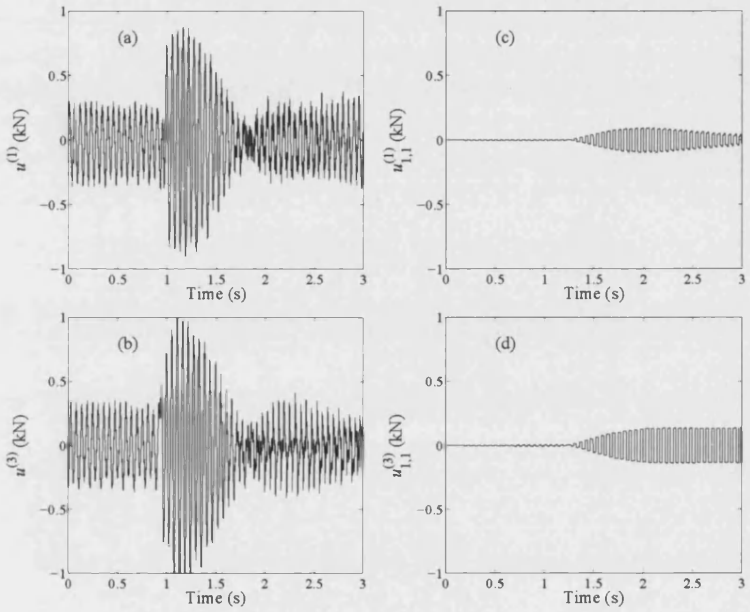

Figure 8.14: (a) and (b) show the total control forces at non driven end and driven end active magnetic bearings at a rotational speed of 18Hz. (c) and (d) show the wavelet coefficient control force.

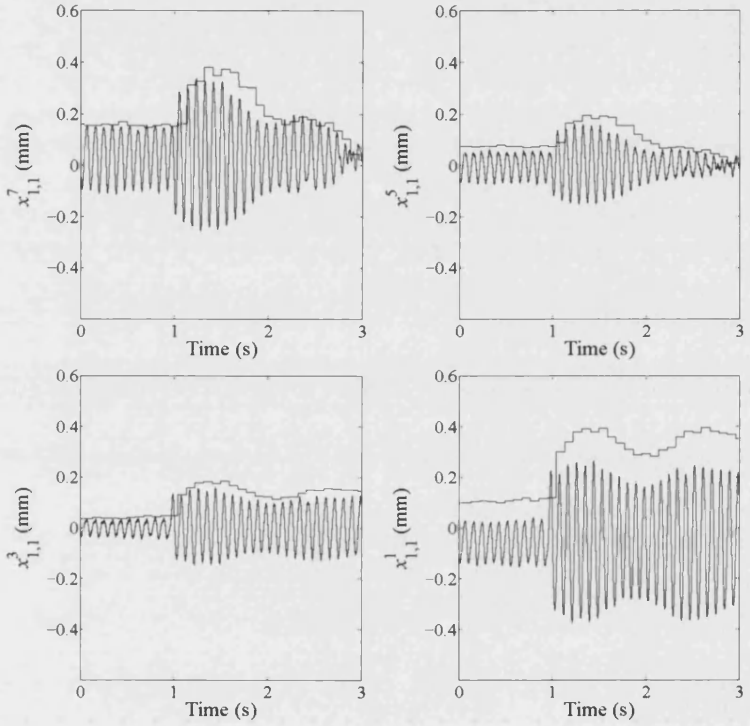

Figure 8.15: Measured mass-loss response and wavelet coefficients in the x-axis at a rotational speed of 11Hz for a controller configured with a prescribed fast exponential decay.

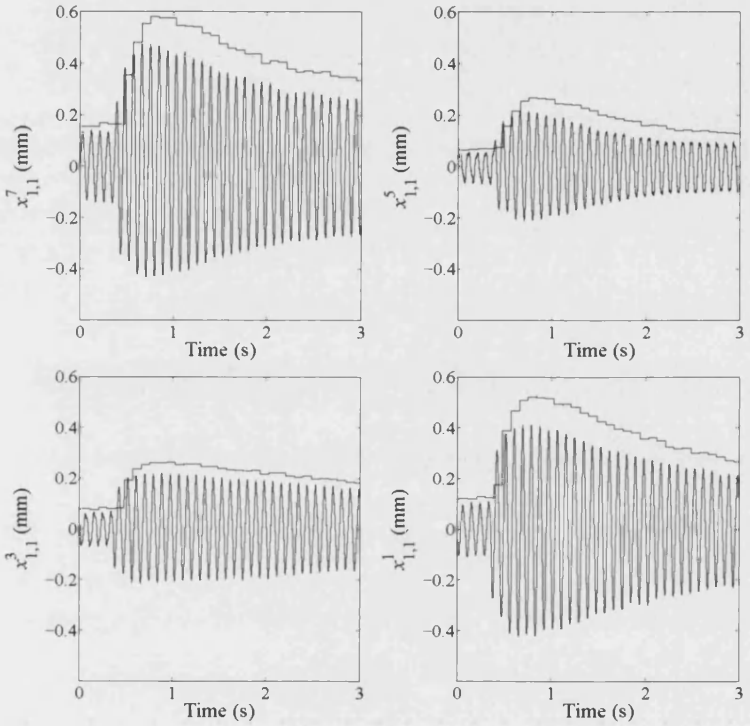

Figure 8.16: Measured mass-loss response and wavelet coefficients in the x-axis at a rotational speed of 11Hz for a controller configured with a prescribed slow exponential decay.

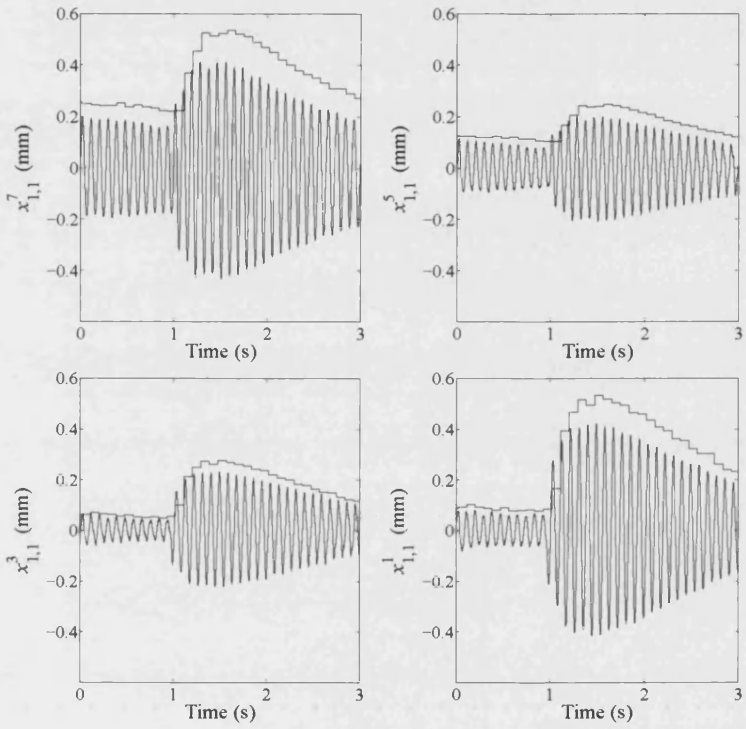

Figure 8.17: Measured mass-loss response and wavelet coefficients in the x-axis at a rotational speed of 11Hz for a controller configured with a prescribed linear decay.

8.6 Closure

A novel method of transient rotor/active magnetic bearing control using sampled wavelet harmonics has been proposed. Control currents were formulated in the wavelet coefficient domain in order to attenuate the measured transient rotor vibration. The wavelet based controller was designed from a target transient response due to step changes in wavelet coefficients of input disturbances. Transient system dynamics were embedded in the controller and derived from on-line system identification.

Experimental validation was performed on a flexible rotor/active magnetic bearing facility. Mass loss experiments were undertaken at the first two critical rotor speeds. The controller suppressed the transient responses within a finite settling time. Variation of the prescribed transient responses are shown to allow shaping of the rotor vibratory signals. Stability criteria for linear and exponentially decaying wavelet controllers are identified. This method offers potential for an improved control strategy utilizing multiple wavelet levels. Optimizing the computational efficiency to minimize control evaluation delays would improve stability margins and performance.

Chapter 9

CONCLUSIONS AND RECOMMENDATIONS

The problem of transient control during fault condition has been identified as an area of important consideration when designing rotor/magnetic bearing systems. It is critical to identify the onset time and fault type in order to evaluate sufficient control currents to maintain operation within specified boundary conditions. This can either be achieved with fault tolerant control or by using a reconfigurable controller with fault detection software. Recent studies into wavelet analysis have shown it to be an excellent tool for analyzing transient behaviour. This thesis is concerned with using the transient properties of wavelet analysis to improve methods of fault identification and rotor/magnetic bearing control.

A method of fault detection has been proposed identifying the onset time of both sudden changes in rotor unbalance, including mass-loss, and rotor/auxiliary bearing contact.

A comparative approach has been undertaken by considering fault specific vibrations in fixed and rotating reference frames. Artifacts associated with the onset of fault conditions are identified using wavelet coefficient analysis. This method is independent of the choice of mother wavelet. However, better bandwidth and dispersion are achieved using short duration wavelets. Signal evaluation time is also an important factor emphasizing the importance of wavelet duration. This method is validated using both simulation and by undertaking experimental tests. Experimental results show that artifacts present in the wavelet coefficients associated with both sudden mass loss and rotor/bearing contact can be distinguished. Validation was performed using Haar wavelet coefficients. However, the method was also shown to be accurate during simulations with higher order Daubechies mother wavelets.

It is important from a design and analysis view point to have a clear and accurate understanding of system dynamics. Therefore, when considering a system in

the wavelet coefficient domain it is advantageous to be able to identify the system dynamics associated with the wavelet coefficients. A generalized framework has been presented for identifying the wavelet coefficient transfer function of a system. Furthermore, the mother wavelets of the system disturbance and output may be varied. Therefore the choices of input and output wavelet can be tailored according to both the disturbance and vibratory response characteristics. The framework also allows for the analysis of different wavelet levels, or pseudo frequencies. An example transfer function is identified using Haar wavelet coefficients for both the input disturbance and output.

Although steady state control methods, such as synchronous rotor vibration controllers, allow reasonably fast evaluation of control signals they may be ineffective or unstable during transient disturbances. Robust control strategies can ensure system stability, however, this is often at the expense of evaluation time which is increased by their higher order. A method of predicting the steady state vibration using wavelet coefficients was presented as a means of fault analysis and control signal moderation. This method utilizes inverse system dynamics at a number of different wavelet coefficient levels identifying their long term behaviour. Full signal reconstruction yields the predicted steady state vibration of the system. The steady state prediction showed excellent agreement with measured steady state vibration, with a reduced transient response period. Controller performance using predictive steady state vibration was assessed. Controllers were developed using proportional wavelet coefficient feedback. Predictive steady state measurements were then used to moderate the control signal. Mass-loss experiments showed that both controllers suppressed rotor vibration. In the case of direct wavelet coefficient feedback, limited stability results in a conservative control strategy. Moderating the controller input using predictive steady state measurements increased stability margins allowing for improved system performance. These problems are largely associated with the delays incurred in the evaluation of the control signals. Predictive steady state moderation is therefore seen as an improvement to the control of the system allowing for increased control action during transient vibration periods.

An alternative method of novel transient control has also been presented using sampled wavelet coefficients. Control currents were formulated from reconstruction of control wavelet coefficients evaluated in the wavelet coefficient domain. The controller was identified from a pre-specified target transient response due to step changes in the disturbance wavelet coefficients. Transient system dynamics were incorporated into the controller to ensure system performance during the transient response and were identified on-line. Experimental validation performed using mass-loss tests was shown to be successful at suppressing transient rotor vibration within a finite time. Transient response shaping was demonstrated with fast and slow exponential decays and a linear target response. Theoretical and experimentally determined stability and acceptable performance bounds were found.

This thesis has covered a range of important topics in rotor/active magnetic bearing systems, from fault detection to transient controller design, all based on wavelet

coefficients. Wavelet coefficient analysis has been shown to be an important tool for identifying and characterizing transient rotor behaviour. This was demonstrated in both fault detection/identification and as a method of predicting steady state vibration. Furthermore, novel techniques of control in the wavelet coefficient domain have been developed. These techniques, however, are not specific to rotor/magnetic bearings and can be applied to any system with short term periodic disturbances resulting in transient behaviour. These are important concepts and should be considered for other dynamic systems.

The major limiting factor in controller performance is the delay time between a transient event occurring and the application of an appropriate control action. Improved methods for evaluating the wavelet coefficients and control forces would be a significant advantage and would benefit from further consideration. Other areas that would benefit from further research include the use of different wavelets at the controller input and output as a means of identifying transient responses quicker and applying more accurate control forces. This also includes considering the use of different frequency wavelets in the controller input and output with the objective to match high frequency transients with low frequency steady states.

Bibliography

[1] M. Dussaux. "The Industrial Applications for Active Magnetic Bearings Technology". *Proceedings of the Second International Symposium on Magnetic Bearings*, 1:33–38, 1990.

[2] G. Scweitzer, H. Bleuler, and A. Traxler. *Active Magnetic Bearings.* Vdf Hochschulverlag AGder ETH, Zürich, 1994.

[3] C.R. Burrows and M.N. Sahinkaya. "Vibration Control of Mutli–Mode Rotor–Bearing Systems". *Proceedings of the Royal Society of London Series A-Mathematical Physical and Engineering Sciences*, 386(1790):74–94, 1983.

[4] C.R. Burrows, M.N. Sahinkaya, and S. Clements. "Active Vibration Control of Flexible Rotors – An Experimental and Theoretical Study". *Proceedings of the Royal Society of London Series A-Mathematical Physical and Engineering Sciences*, 422 (1862):123–146, 1989.

[5] C.R. Knospe, R.W Hope, S.J. Fedigan, and R.D. Williams. "Experiments in the Control of Unbalance Response Using Magnetic Bearings". *Mechatronics*, 5(4):385–400, 1995.

[6] C.R. Knospe, S.J. Fedigan, R.W Hope, and R.D. Williams. "A Multitasking DSP Implementation of Adaptive Magnetic Bearing Control". *IEEE Transactions on Control Systems Technology*, 5(2):230–238, 1997.

[7] C.R. Knospe, S.M. Tamer, and J. Lindlau. "New Results in Adaptive Vibration Control". *Proceedings 1997 industrial conference and exhibition on magnetic bearings*, pages 209–219, 1997.

[8] B. Sahfai, B. Beale, P. LaRocca, and E. Cussons. "Magnetic Bearing Control Systems and Adaptave Forced Balancing". *Control Systems, IEEE*, 14:4–113, 1994.

[9] M.O.T. Cole, P.S. Keogh, and C.R. Burrows. "Control of Multifrequency Rotor Vibration Components". *Proceedings of the Institution of Mechanical Engineers Part C: Journal of Mechanical Engineering Science*, 216(2):165–177, 2002.

[10] P.S. Keogh, M.O.T. Cole, and C.R. Burrows. "Multi-State Transient Rotor Vibration Control Using Sampled Harmonics". *Journal of Vibration and Acoustics-Transactions of the ASME*, 124(2):186–197, 2002.

[11] M. Fujita, F. Matsumura, and M. Shimizu. "Robust Control Design for a Magnetic Suspension System". *Proceedings of the Second International Symposium on Magnetic Bearings*, pages 349–356, 1990.

[12] R. Herzog and H. Bleuler. "Stiff AMB Control Using an H_∞ Approach". *Proceedings of the Second International Symposium on Magnetic Bearings*, pages 343–348, 1990.

[13] R. Herzog and H. Bleuler. "On Achievable H_∞ Disturbance Attenuation in AMB Control". *Proceedings of the Third International Symposium on Magnetic Bearings*, pages 485–494, 1992.

[14] C. Mu, P.S. Keogh, and C.R. Burrows. "H_∞ Controller Design for Active Vibration Control of a Flexible Rotor". *Vibrations in Rotating Machinery, IMechE*, pages 131–135, 1992.

[15] P.S. Keogh, C. Mu, and C.R. Burrows. "Optimized Design of Vibration Controllers for Steady and Transient Excitation of Flexible Rotors". *Proceedings Institute of Mechanical Engineers Part C: Journal of Mechanical Engineering Science*, 209(3):155–168, 1995.

[16] M.O.T. Cole, P.S. Keogh, and C.R. Burrows. "Vibration Control of a Flexible Rotor Magnetic Bearing System Subject to Direct Forcing and Base Motion Disturbances". *Proceedings of the Institution of Mechanical Engineers Part C: Journal of Mechanical Engineering Science*, 212(7):535–546, 1998.

[17] K. Nonami and T. Ito. "μ Synthesis of Flexible Rotor Magnetic Bearing Systems". *Proceedings of the 4th International Symposium on magnetic bearings*, pages 73–78, 1994.

[18] S. Sivrioglu and K. Nonamin. "Sliding Mode Control With Time-Varying Hyperplane for AMB Systems". *IEEE-ASME Transactions on Mechatronics*, 3(1):51–59, 1998.

[19] M.O.T. Cole, P.S. Keogh, and C.R. Burrows. "Fault-Tolerent Control of Rotor/Magnetic Bearing Systems Using Reconfigurable Control with Built-In Fault Detection". *Proceedings of the Institution of Mechanical Engineers Part C: Journal of Mechanical Engineering Science*, 214(3):1445–1465, 2000.

[20] C. Seo and B.K. Kim. "Robust and Reliable H_∞ Control for Linear Systems with Parameter Uncertainity and Acuator Failure". *Automatica*, 32(3):465–467, 1996.

[21] A.N. Gündes. "Stabilizing Controller Design for Linear Systems with Sensor or Actuator Failures". *Transactions on Automatic Control, IEEE*, 39:1224–1230, 1994.

[22] D. Sauter and F. Hamelin. "Frequency-Domain Optimization for Robust Fault Detection and Isolation in Dynamic Systems". *Transactions on Automatic Control, IEEE*, 44(4):878–882, 1999.

[23] Y. Maki and K.A. Loparo. "A Neural-Network Approach to Fault Detection and Diagnosis in Industrial Processes". *Transactions on Control System Technology, IEEE*, 5(6):529–541, 1997.

[24] M.N. Sahinkaya, M.O.T. Cole, and C.R. Burrows. "Fault Detection and Tolerance in Synchronous Vibration Control of Rotor-Magnetic Bearing Systems ". *Proceedings Institute of Mechanical Engineers Part C: Journal of Mechanical Engineering Science.*, 215(12):1401–1416, 2001.

[25] N. Bachschmid and A. Pennacchi, P. Vania. "Identification of Multiple Faults in Rotor Systems". *Journal of Sound and Vibration*, 254(2):327–366, 2002.

[26] M. Antonini, M. Barlaud, P. Mathieu, and I. Daubechies. "Image Coding Using Wavelet Transform". *Proceedings of the International Conference on Image Processing, IEEE*, 1:205–220, 1992.

[27] M.S. Lee. "Image Compression and Watermarking by Wavelet Localisation". *International Journal of Computer Mathematics*, 80(4):401–412, 2003.

[28] J. Zhang, G.G. Gilbert, Y. Miao, and W.N.W. Lee. "Wavelet Neural Networks for Function Learning". *Transactions on Signal Processing*, 43, 1995.

[29] B.R. Keeton. "Applications of Wavelets in Doppler Ultrasound". *Sensors Review*, 17:38–145, 1997.

[30] D.L. Donoho. "De-Noising by Soft-Thresholding". *IEEE Transactions On Information Theory*, 41(3):613–627, 1995.

[31] I.K. Fodor and C. Kamath. "Denoising Through Wavelet Shrinkage: An Empirical Study". *Journal of Electronic Images*, 12(1):151–160, 2003.

[32] S.G. Mallat. "A Theory for Multiresolution Signal Decomposition - The Wavelet Representation". *Transactions on Pattern Analysis and Machine Intelligence, IEEE*, 11(7):269–276, 1989.

[33] D.E. Newland. "Wavelet Analysis of Vibration, Part 1: Theory". *Journal of Vibration and Acoustics–Transactions of the ASME*, 116(4):409–416, 1994.

[34] V.C. Chancey and G.T. Flowers. "Identification of Transient Vibtarion Characteristics Using Aboslute Harmonic Wavelet Coefficients". *Journal of Vibration and Control*, 7(8):1175–1193, 2001.

[35] W.J. Staszewski. "Identification of Damping in MDOF Systems Using Time–Scale Decomposition". *Journal of Sound and Vibration*, 203(2):283–305, 1997.

[36] D.E. Newland. "Wavelet Analysis of Vibration, Part 2: Wavelet Maps". *Journal of Vibration and Acoustics–Transactions of the ASME*, 116(4):417–425, 1994.

[37] V.C. Chancey, G.T. Flowers, and C.L. Howard. "A Harmonic Wavelet Approach for Extracting Transient Patterns from Measured Rotor Vibration Data". *Journal of Engineering for Gas Turbines and Power-Transactions of the ASME*, 125(1):18–89, 2003.

[38] W.J. Staszewski. "Identification of Non–Linear Systems Using Multi–Scale Ridges and Skeletons of the Wavelet Transform". *Journal of Sound and Vibration*, 214(4):639–658, 1998.

[39] Z. Geng and L. Qu. "Vibrational Diagnosis of Machine Parts Using the Wavelet Packet Technique". *British Journal Of Non-Destructive Testing*, 36(1):11–15, 1994.

[40] W.J. Staszewski. "Wavelet Based Compression and Feature Analysis Selection for Vibration Analysis". *Journal of Sound and Vibration*, 211(5):735–760, 1998.

[41] S. Prabhakar, A.S. Sekhar, and A.R. Mohanty. "Detection and Monitoring of Cracks in a Rotor–Bearing System Using Wavelet Transforms". *Mechanical Systems and Signal Processing*, 15(2):447–450, 2001.

[42] S. Prabhakar, A.S. Sekhar, and A.R. Mohanty. "Vibration Analysis of a Misaligned Rotor-Coupling-Bearing System Passing Through the Critical Speed". *Proceedings of the Institution of Mechanical Engineers Part C: Journal of Mechanical Engineering Science*, 215(12):1417–1428, 2001.

[43] J. Lin and L.S. Qu. "Feature Extraction Based on Morlet Wavelet and its Application for Mechanical Fault Diagnosis". *Journal of Sound and Vibration*, 234(1):135–148, 2000.

[44] D. Boulahbal, M.F. Farid, and F. Ismal. "Amplitude and Phase Wavelet Maps for the Detection of Cracks in Geared Systems". *Mechanical Systems and Signal Processing*, 13(3):423–436, 1999.

[45] Q.G. Zhang and A. Benveniste. "Wavelet Networks". *IEEE Transactions On Neural Networks*, 3(6):889–898, 1992.

[46] C.L. Lin and H.T. Huang. "Linear Servo Motor Control Using Adaptive Neural Networks". *Proceedings of the Institution of Mechanical Engineers Part I-Journal of Systems And Control Engineering*, 216(15):407–427, 2002.

[47] S. Parvez and Z.Q. Goa. "A Wavelet-Based Multiresolution PID Controller". *IEEE Transactions On Industry Applications*, 41(2):537–7543, 2005.

[48] Y.H. Zhou, J. Wang, X.J. Zheng, and Q. Jiang. "Vibration Control of Variable Thickness Plates with Piezoelectric Sensors and Actuators Based on Wavelet Theory". *Journal of Sound and Vibration*, 237(3):1395–410, 2000.

[49] I.S. Cade, P.S. Keogh, and M.N. Sahinkaya. "Fault Identification in Rotor/Magnetic Bearing Systems Using Discrete Time Wavelet Coefficients". *IEEE-ASME Transactions on Mechatronics*, 10(6):648–657, 2005.

[50] N.K. Rutland and P.S. Keogh. "Design of an Experimental Rotor/Active Magnetic Bearing Rig". *Report number 030/1994, University of Bath, UK*, 1994.

[51] N.K. Rutland and P.S. Keogh. "Design Procedure for an Active Magnetic Bearing". *Report number 0329/1994, University of Bath, UK*, 1994.

[52] N.K. Rutland and P.S. Keogh. "Experimental Validation of an Active Magnetic Bearing Force Characteristic". *Report number 032/1994, University of Bath, UK*, 1995.

[53] H.D. Nelson and J.M. McVaugh. "The Dynamics of Rotor–Bearing Systems Using Finite Elements". *Journal of Engineering for Industry–Transactions of the ASME*, pages 593–600, 1976.

[54] E.S. Zorzi and H.D. Nelson. "Finite Element Simulation of Rotor–Bearing Systems With Internal Damping". *Journal of Engineering for Power–Transactions of the ASME*, pages 71–76, 1977.

[55] R.L. Ruhl and J.F. Booker. "A Finite Element Model for Distributed Parameter Turborotor Systems". *Journal of Engineering for Industry–Transactions of the ASME*, pages 126–132, 1972.

[56] P. Hammond. *Electromagnetism for Engineers: An Introductory Course, Third Edition.* Pergamon Press, Oxford, 1986.

[57] J.D. Knight, Z. Xia, E. McCaul, and H. Hacker. "Determination of Forces in a Magnetic Bearing Actuator". *Journal of Tribology–Transactions of the ASME*, 114:796–801, 1992.

[58] G. Schweitzer. "Safety and Reliability Aspects for Active Magnetic Bearing Applications - a Survey ". *Proceedings of the Institution of Mechanical Engineers Part I-Journal of Systems and Control Engineering*, 219 (16):383–392, 2005.

[59] P.S. Keogh and M.O.T. Cole. "Rotor Vibration with Auxiliary Bearing Contact in Magnetic Bearing Systems - Part 1: Synchronous Dynamics ". *Proceedings of the Institution of Mechanical Engineers Part C-Journal of Mechanical Engineering Science*, 217(4):377–392, 2003.

[60] M.O.T. Cole and P.S. Keogh. "Rotor Vibration with Auxiliary Bearing Contact in Magnetic Bearing Systems - Part 2: Robust Synchronous Control for Rotor Position Recovery". *Proceedings of the Institutionof Mechanical Engineers Part C-Journal of Mechanical Engineering Science*, 217(4):393–409, 2003.

[61] P.S. Keogh, M.O.T. Cole, M.N. Sahinkaya, and Burrows C.R. "On the Control of Synchronous Vibration in Rotor/Magnetic Bearing Systems Involving Auxiliary Bearing Contact". *Journal of Engineering for Gas Turbines and Power-Transactions Of The Asme*, 126(2):366–372, 2004.

[62] J.M. Maciejowski. *Multivariable Feedback Design.* Addison–Wesley Publishers Ltd, 1989.

[63] K. Zhou, J.C. Doyle, and K. Glover. *Robust and Optimal Control.* Prentice Hall, 1996.

[64] D.B. Ridgely. *Introduction to Robust Multivariable Control.* Microinfo, 1989.

[65] M. Aenis, E. Knopf, and R. Nordmann. "Active Magnetic Bearings for the Identification and Fault Diagnosis In Turbomachinery". *Mechatronics*, pages 1011–1021, 2002.

[66] R. Isermann. "Model-Based Fault-Detection and Diagnosis - Status and Applications". *Annual Reviews in Control*, pages 71–85, 2005.

[67] M. Vetterli and Kovačević. *Wavelets and Subband Coding.* Prentice Hall, Inc, New Jersey, 1995.

[68] G. Strang and T. Nguyen. *Wavelets and Filter Banks.* Wellsey–Cambridge Press, Cambridge, MA, 1996.

[69] I. Daubechies. *Ten Lectures on Wavlets.* Society for industrial and applied mathematics, Philadelphia, Pennsylvania, 1992.

[70] D. Gabor. "Theory of Communication". *Journal of the IEE*, pages 429–457, 1946.

[71] I. Daubechies. "Time-Frquency Localization Operators: A Geometric Phase–Spae Approach". *IEEE Transactions on Information Theory*, 34(4):605–612, 1988.

[72] F. Keinert. *Wavelets and Multiwavelets.* Chapman and Hall/CRC, New York, 2000.

[73] D.M. Monro, B.E. Bassil, and G.J. Dickson. "Orthonormal Wavelets with Balanced Uncertainity". *Proceedings of the International Conference on Image Processing, IEEE*, 2:539–532, 1996.

[74] J.J. DiStefano, A.R. Stubberud, and I.J. Willams. *Schaum's Outline of Theory and Problems of Feedback and Control Systems, Second Edition.* McGraw–Hill, United States of America, 1990.